Analysis and modeling of the distribution of tracers of glacial melt in the Southern Ocean with focus on the Southeast Pacific sector

Dissertation zur Erlangung des
Doktorgrades der Naturwissenschaften
Dr. rer. nat.

dem Fachbereich Physik/Elektrotechnik der
Universität Bremen
vorgelegt von

Yoshihiro Nakayama

14. Nov 2014

Universität Bremen

ALFRED-WEGENER-INSTITUT
HELMHOLTZ-ZENTRUM FÜR POLAR-
UND MEERESFORSCHUNG

Date of Colloquium 17. Feb. 2015

1. Referees: Prof. Dr. P. Lemke

2. Referees: Prof. Dr. T. Kanzow

Acknowledgement

I would like to sincerely appreciate my supervisor, Dr. Hartmut Hellmer for giving me the opportunity to conduct my doctoral study at the Alfred Wegener Institute and his supervision throughout my doctoral thesis. I acknowledge Dr. Michael Schröder and Dr. Ralph Timmermann for their supervision on the analysis of the hydrographic data obtained during ANTXXVI/3 in 2010 on the eastern Amundsen Sea continental shelf and the modeling of the Pacific sector using the Finite-Element Sea-ice/ice-shelf/Ocean Model (FESOM), respectively.

I thank Dr. Christian Rodehacke for supporting my study at the Max Planck Institute for Meteorology regarding the implementation of an ocean-atmosphere gas exchange module in FESOM. I thank Dr. Sergey Danilov, Dr. Dmitry Sidorenko, and Dr. Qiang Wang for their technical help and support on FESOM matters. I thank Dr. Jürgen Sültenfuß and Dr. Oliver Huhn for the noble gas measurements. I also thank Prof. Dr. Shigeru Aoki, Dr. Karen M. Assmann, Dr. Pierre Dutrieux, Dr. Paul Holland, Stanley S. Jacobs, Prof. Dr. Adrian Jenkins, Dr. Kazuya Kusahara, and Prof. Dr. Kay I. Ohshima for their useful comments and suggestions during my doctoral study. I also would like to thank Prof. Dr. Takenobu Toyota for his kind support and advice when applying for the doctoral-position at the Alfred Wegener Institute.

This study is also a contribution to the Earth System Science Research School (ESSReS). I would like to thank Dr. Klaus Grosfeld, Dr. Helge Meggers, and Dr. Ludvig Löwemark for organizing helpful lectures, soft-skill trainings, and monthly seminars during the last three years, which expanded my knowledge in Earth system science and enabled me to improve my scientific performance. I also would like to express my gratitude to Stefanie Klebe for their excellent administrative support that provided a very comfortable research environment.

I would also like to thank all my colleagues, doctoral students in ESSReS, and friends.

Abstract

In the Pacific sector of the Southern Ocean, the ice shelves and glaciers of the West Antarctic Ice Sheet (WAIS) are rapidly thinning, especially in the Amundsen Sea (AS) and Bellingshausen Sea (BS). The high basal melting of these relative small ice shelves is caused by warm Circumpolar Deep Water (CDW) that, based on observations, mainly intrudes via submarine glacial troughs located at the continental shelf break. When CDW reaches the grounding line of the fringing glaciers, strong basal melting supports a buoyant melt water plume. As the glacial melt becomes part of the shelf circulation, it may cause a freshening of the shelf water locally as well as remotely in the Ross Sea (RS). In the RS, on the other hand, shelf water salinity has declined by 0.03 per decade over the past 50 years. Thus, the objective of this doctoral thesis is to simulate the spreading of glacial melt water using the Finite-Element Sea-ice/ice-shelf/Ocean Model (FESOM) and investigate whether the ice shelf melting in the AS is one of the main reasons for the observed shelf water freshening in the RS.

However, there are two main difficulties for the simulation of the spreading of glacial melt water: (1) the number of observations on the Amundsen Sea continental shelf and thus our understanding of CDW intrusions, ice shelf basal melting, and spreading of glacial melt water is limited and (2) none of the high-resolution global models resolving all small ice shelves around Antarctica is able to simulate CDW intrusions realistically. Thus, in this doctoral study the hydrographic data of the cruise ANTXXVI/3 from the eastern AS continental shelf was analyzed, focusing on intrusions of CDW, basal melting of Pine Island Ice Shelf (PIIS), and spreading of glacial melt water. The data analysis was followed by several model sensitivity experiments using FESOM. They revealed that the model configuration such as horizontal resolution and atmospheric forcing is important for the reproduction of CDW intrusions.

With these modifications, FESOM reproduces the bottom temperatures in the AS and BS and basal melt rates of AS and BS ice shelves much closer to reality. Therefore, I tested whether the observed freshening of the RS is a consequence of enhanced basal melting of AS ice shelves. Using several independent virtual passive tracers to identify pathways of the glacial melt, I found that the melt water from the ice shelves in the AS mainly flows towards the Ross Ice Shelf front. After 10 years of simulation, about half of the melt water in the RS originates from the Getz Ice Shelf. Further, I investigated the sensitivity of the melt water transport into the RS associated with the strength of the basal melt water flux. When this flux is increased by 30%, the transport of glacial melt into the RS nearly doubles, supporting the idea that the basal melting of AS and BS ice shelves is one of the main reasons for the observed freshening on the RS continental shelf. This may imply that the observed freshening of the RS in the late 1970's/early 1980's, prior to the remotely sensed increase in ice shelf mass losses, might have been caused by enhanced basal melting already in the 1960's.

Contents

1 Introduction

1.1 The importance of the Southern Ocean for the global climate

Around Antarctica, cold and dense water is formed due to intense sea-ice formation in coastal polynyas, which are thin-ice or ice-free regions formed by persistent divergent ice motions in response to prevailing winds and/or oceanic currents. This dense water spreads near the bottom of most of the continental shelves around Antarctica, in some cases interacts with ice shelves, descends the continental slope, and contributes to the formation of Antarctic Bottom Water (AABW). AABW is mainly formed in the Weddell Sea, Ross Sea (RS), and off Adélie Land (*Orsi et al.*, 1999) (Fig. 1.1a). Since AABW formation is one of the drivers of the global thermohaline circulation, transporting cold and dense water from higher latitudes towards tropics (*Schmitz*, 1995), understanding AABW formation is important for assessing the response of the ocean to climate variability and change.

Ocean circulation around Antarctica is also important because it supplies heat to the Antarctic ice sheet. In the Amundsen Sea (AS) and Bellingshausen Sea (BS), the southern branch of the Antarctic Circumpolar Current (ACC) brings warm Circumpolar Deep Water (CDW, $\sim$1.5 °C) closer to the continental shelf (yellow contour in Fig. 1.1a). This warm water intrudes onto the AS continental shelf through the eastern and central submarine glacial troughs (marked E and C in Fig. 1.1c) and flows into the fringing ice shelf cavities, e.g., under Pine Island Ice Shelf (PIIS) and Thwaites Glacier (TG) (vertical section in Fig. 1.1b and red arrows in Fig. 1.1c), causing a rapid thinning of the West Antarctic Ice Sheet (WAIS) (*Pritchard et al.*, 2012). Repeated oceanographic observations show that CDW ($\sim$1.0 °C) reaches the PIIS cavity (*Jacobs et al.*, 1996; *Jenkins et al.*, 2010; *Jacobs et al.*, 2011), fueling the highest basal melt rates determined for an Antarctic ice shelf. Based on satellite observations, basal mass loss of the AS and BS ice shelves is estimated to be $\sim$ 500 and $\sim$ 150 Gt $^{-1}$yr, respectively (*Rignot et al.*, 2013).

The mass loss of the WAIS could have two large impacts. First, the rapid thinning of WAIS contributes to global sea-level rise through dynamic changes of the ice sheet, which are thought to be initiated by an increase of ice shelf basal melting (*Rignot*, 1998). PIIS and TG together drain $\sim$13% of the entire Antarctic ice sheet (e.g., *Rignot et al.*, 2013) and WAIS contributes $\sim$10% of recent observed global sea level rise ($\sim$0.3 mm yr^{-1}; *Church and White*, 2011). The collapse of WAIS has the potential to raise global sea level by $\sim$3.3 m (*Bamber et al.*, 2009). Second, basal melting of AS ice shelves can cause freshening of shelf water locally in the AS as well as remotely in the RS (*Jacobs et al.*, 2002). *Jacobs and Giulivi* (2010) show that shelf water salinity in the southwest RS has declined by 0.03 per decade over last 50 years and suggest that the observed freshening may be related to increased ice shelf melting upstream in the AS. Furthermore, *Nakayama et al.* (accepted) show that glacial meltwater in the AS flows along the coast into the RS (blue arrows in Fig. 1.1c). This may lead to a change in the characteristics of AABW formed in the RS and further downstream, thus influencing the strength of the global thermohaline circulation (*Jacobs et al.*, 2002; *Rintoul*, 2007). Therefore, understanding the controlling mechanism for the rapid ice shelf melting as well as the spreading of glacial melt water is crucial for investigating the role of the WAIS in the global climate system.

1.2 Research outline

This doctoral thesis is focussed on the analysis and modeling of the distribution of tracers of glacial melt in the Southeast Pacific sector of the Southern Ocean. However, there are two main difficulties for the simulation of the spreading of glacial melt water: (1) there have not been enough observations on the AS continental shelf with respect to CDW intrusions, ice shelf basal melting, and spreading of glacial meltwater and (2) none of the high-resolution global models, resolving small ice shelves around Antarctica, is able to simulate realistic CDW intrusions onto the AS continental shelf.

Thus, I first conducted the study entitled "From circumpolar deep water to the glacial melt water plume on the eastern Amundsen Shelf" (published in Deep Sea Research Part l, referred to *Nakayama et al.* (2013), see chapter 2). In this study, I analyzed the hydrographic data of cruise ANTXXVI/3 with the German research ice breaker Polarstern. Due to extremely low sea-ice coverage in austral summer 2010, we were able to conduct CTD measurements over the whole eastern AS continental shelf, including two submarine glacial troughs that channel CDW all the way into the PIIS cavity. This study shows, for the first time, the relative importance of the eastern and central CDW intrusions towards the glaciated coast. In this study, I also analyzed the melt rate of PIIS in 2010, the spreading of glacial melt water, and the temporal variability of CDW properties in the bottom layer on the continental shelf.

Second, I conducted the study entitled "On the difficulty of modeling Circumpolar Deep Water intrusions onto the Amundsen Sea continental shelf" (published in Ocean Modeling, referred to *Nakayama et al.* (2014), see chapter 3). Although high resolution global models, resolving small ice shelves around Antarctica, are an ideal tool to study the possible interaction between ice shelf melting in the AS and the RS freshening, there have not been any study successfully reproducing CDW intrusions in the global set-up. However, I am now able to simulate CDW intrusions onto the AS continental shelf with realistic basal melt rates of West Antarctic ice shelves using the global Finite-Element Sea-ice/ice-shelf/Ocean Model (FESOM). I use a tetrahedral mesh with a horizontal spacing of $\sim$2-10 km over the central Amundsen and Bellingshausen Seas and a hybrid vertical coordinate system with 46 layers with a z-level discretization in the mid- and low-latitude ocean basins. For the vertical coordinate system, the top 21 layers along the Antarctic coast are terrain-following (sigma coordinate) for depths shallower than 650 m. I conducted sensitivity studies showing the importance of the model configuration such as horizontal resolution and atmospheric forcing for reproducing CDW intrusions. This study is important because global models, considering ocean-ice shelf interaction, are required to simulate the spreading of glacial melt water and investigate the impact of WAIS melting on the local and global ocean circulation.

Finally, I conducted the study entitled "Modeling the spreading of glacial melt water from the Amundsen and Bellingshausen Seas" (accepted in Geophysical Research Letters, see chapter 4). It has been suggested that an increased melting of continental ice in the AS (AS) and BS is a likely source of the observed freshening of RS waters. To test this hypothesis, I simulated the spreading of glacial melt water using the global FESOM. Based on the spatial distribution of simulated passive tracers, most of the basal melt water from AS ice shelves flows towards the RS. Further, the model results show that a slight increase of the basal mass loss can substantially intensify the transport of melt water into the RS due to a strengthening of the melt-driven shelf circulation and the westward flowing coastal current. This is the first numerical modeling study directly showing the connection between two important findings of polar science: an increasing mass loss of WAIS and the freshening of the RS.

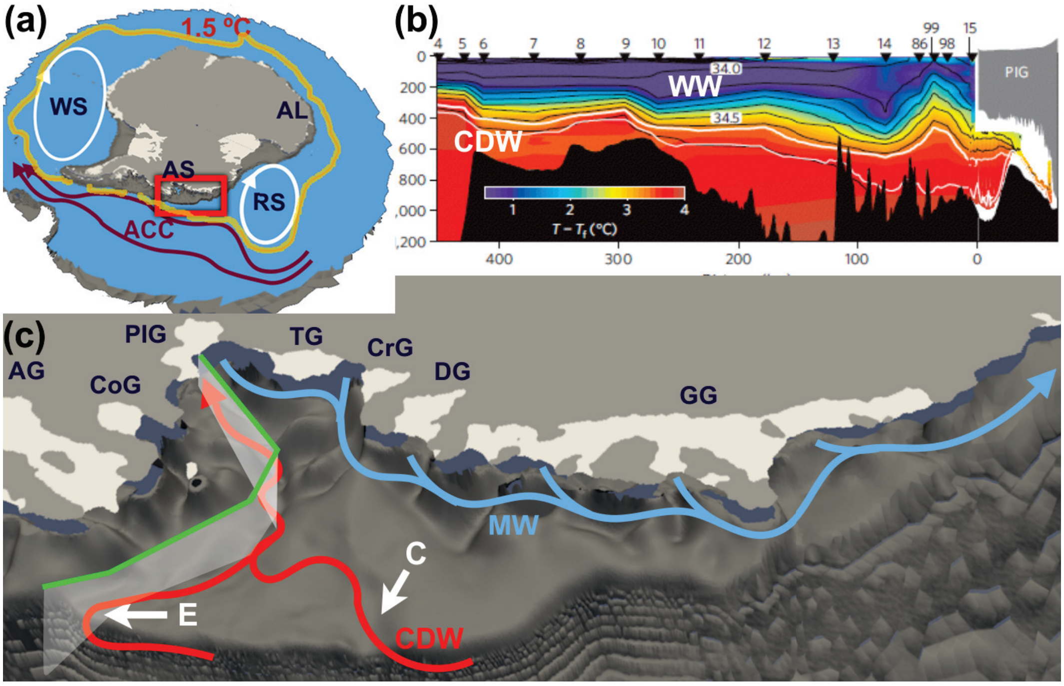

Figure 1.1: **(a)** Schematic of Antarctica. ACC, AL, AS, RS, and WS denote Antarctic Circumpolar Current, Adélie Land, Amundsen Sea (AS), Ross Sea, and Weddel Sea, respectively. White arrows indicate Weddell and Ross Gyres. The dark red arrows indicate pathways of the ACC. The blue surface is the 700-m depth and the yellow line is the 1.5°C contour based on World Ocean Atlas 2005.**(b)** Vertical section showing temperature relative to the in-situ freezing point along the green line in (a) (from *Jacobs et al.* (2011)). CDW and WW denotes Circumpolar Deep Water and Winter Water, respectively. The white arrow indicates the location of ridge in front of PIIS grounding line. **(c)** Ocean bathymetry and location of ice shelves (white) in the AS, the region surrounded by the red box in (c). AG, CoG, PIG, TG, CrG, DG, and GG denote, respectively, the Abbot, Cosgrove, Pine Island, Thwaites, Crosson, Doston, and Getz Ice Shelves. E and C denote submarine glacial troughs located, respectively, on the eastern and central AS continental shelf. The green line represents the section shown in (b). The red and blue arrows show pathways of CDW and glacial meltwater (MW), respectively.

2 Method

This doctoral study uses observational data and a numerical model. Thus, section 2.1 provides an introduction to observational data and data analysis methods used in the first part of the study. In section 2.2, the Finite-Element Sea-ice/ice-shelf/Ocean Model (FESOM) is briefly explained, which is used in the latter part of my study.

2.1 Observation

2.1.1 Observational data

For the data analysis of the eastern Amundsen Sea, I mainly use conductivity-temperature-depth (CTD) data from cruise ANTXXVI/3 of the research ice breaker Polarstern in 2010 (*Gohl*, 2010). Due to an extremely low sea-ice coverage on the whole Amundsen Sea continental shelf, it was possible, for the first time, to conduct comprehensive CTD measurements in its eastern region, including the two submarine glacial troughs that may channel CDW beneath the PIIS (Fig. 2.1). Thus, such data is essential to determine the routes of CDW into the PIIS cavity and to detect the freshwater spreading due to ice shelf basal melting.

For the measurements, a Seabird 911+ CTD (SN 561) connected to a caroussel (SBE 32, SN 202) with 24-(12-l) water bottles was used. This instrument system contains two sensor pairs of conductivity (SBE 4, SN 3607, SN 3590) and temperature (SBE 3, SN 1373, SN 2629), a high precision pressure sensor Digiquartz 410K-105 (SN 68997), one oxygen sensor (SBE 43, SN 743 until station no. 143 and SN 880 from station no. 147 on), one oxygen sensor (Rinko SN 10, optode), a fluorometer (Wetlab ECO-AFL/FL, SN 1365), and a Benthos altimeter Model PSA 916 (SN 1228).

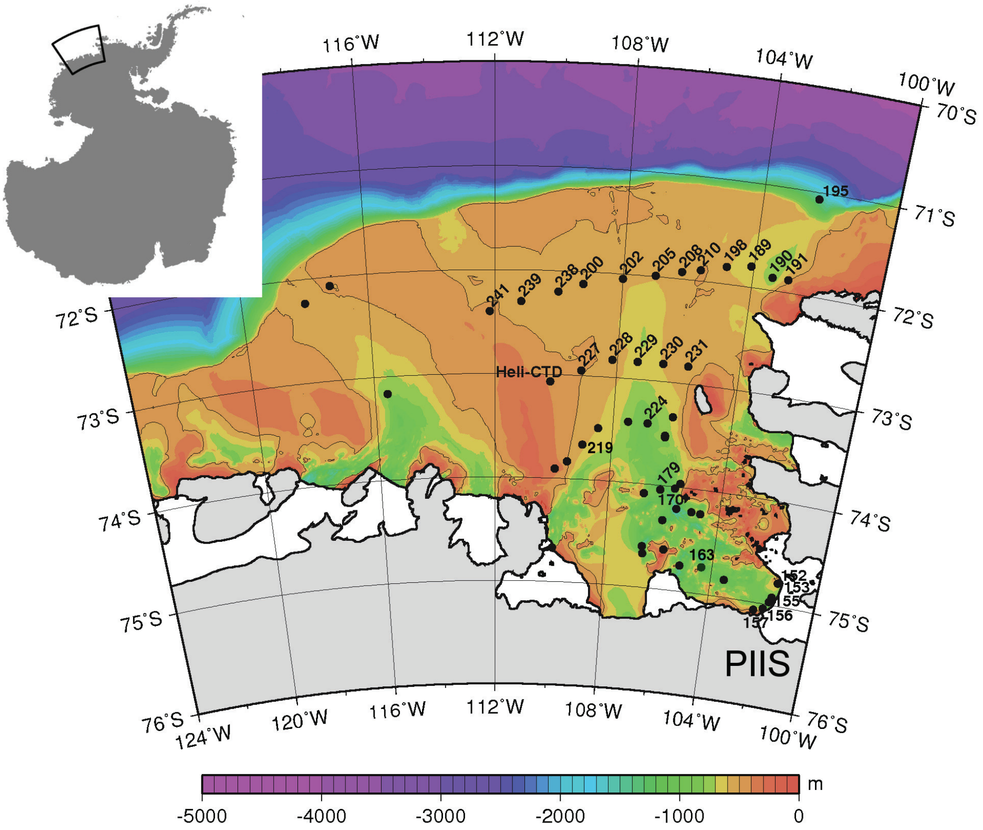

Figure 2.1: Distribution of CTD stations in the eastern Amundsen Sea of the cruise in 2010 (ANTXXVI/3) with bathymetry and coastline (gray shade). The 500-m contour is also shown. The upper-left panel shows Antarctica with the enclosed region denoting the location of enlarged portion. The location of Pine Island Ice Shelf (PIIS) is shown.

The conductivity and temperature sensor calibrations were performed before and after the cruise at Seabird Electronics. The accuracy of the temperature sensors is 2 mK. The readings for the pressure sensors are better than 2 dbar. The conductivity was corrected using salinity measurements from water samples related to IAPSO Standard Seawater from the P-series P149 (K15= 0.99984). A total of 77 water samples were measured using a Guildline Autosal 8400B. On the basis of the water sample correction, salinity is measured to an accuracy of 0.002. The oxygen was corrected from water samples using the Winkler method with a Dissolved Oxygen Analyser (DOA, built by Sensoren Instrumente Systeme, Germany).

For the identification of glacial melt, a few helium and neon samples were taken from the water samples of the CTD casts at the PIIS front section (Fig. 2.1). Helium and neon are supersaturated in seawater when air bubbles are released from the ice by basal melting. Due to their low solubility, these supersaturated noble gas signals show the clearest signature of melt water from meteoric ice (*Schlosser*, 1986; *Hohmann et al.*, 2002). They were all sealed in copper tubes and analyzed by mass spectrometery at the IUP Bremen (*Sültenfuß et al.*, 2009). The accuracy of the measurements is 0.01 nmol kg^{-1} or 1 % for He and 0.04 nmol kg^{-1} or 1 % for Ne, determined from the large number of observations in the western Weddell Sea (*Huhn et al.*, 2008).

In addition, Nathaniel B. Palmer CTD data from 2000, 2007, and 2009 is used to discuss the temporal variability. All data sets are taken in austral summer between January and March.

2.1.2 Meltwater fraction calculation

To investigate the spreading of glacial melt, the melt water fraction is calculated simply as the mixture of three water masses, Circumpolar Deep Water (CDW), glacial Melt water (MW), and Winter Water (WW), (*Jenkins*, 1999; *Jenkins and Jacobs*, 2008; *Jacobs et al.*, 2011) as shown in eqs. (2.1)-(2.3),

$$\chi^1_{mix} = A\chi^1_{CDW} + B\chi^1_{MW} + C\chi^1_{WW}, \tag{2.1}$$

$$\chi^2_{mix} = A\chi^2_{CDW} + B\chi^2_{MW} + C\chi^2_{WW}, \tag{2.2}$$

$$A + B + C = 1, \tag{2.3}$$

where A, B, and C are fractions of CDW, MW, and WW, respectively, and χ is a tracer that is conserved during mixing. For the case of the analysis in chapter 3, two tracers χ^1 and χ^2 are chosen from the available set of parameters of potential temperature, salinity, dissolved oxygen, and concentrations of helium and neon.

The subscripts of χ indicate the defined water mass characteristics for CDW, WW, and MW (Table 2.1) following *Jenkins* (1999), *Jenkins and Jacobs* (2008), and *Jacobs et al.* (2011). By solving for B, the melt water fraction can be obtained as

$$B = \frac{(\chi^1_{mix} - \chi^1_{CDW}) - (\chi^2_{mix} - \chi^2_{CDW})(\dfrac{\chi^1_{WW} - \chi^1_{CDW}}{\chi^2_{WW} - \chi^2_{CDW}})}{(\chi^1_{melt} - \chi^1_{CDW}) - (\chi^2_{melt} - \chi^2_{CDW})(\dfrac{\chi^1_{WW} - \chi^1_{CDW}}{\chi^2_{WW} - \chi^2_{CDW}})}. \tag{2.4}$$

Table 2.1: The water mass characteristics of CDW, WW, and MW. The water mass characteristics of CDW and WW in potential temperature, salinity and dissolved oxygen are chosen such that the CDW/WW mixing line is the same as in *Jacobs et al.* (2011).

	CDW	WW	MW
Potential Temperature (°C)	1.18	-1.8	-90.8
Salinity (psu)	34.7	34.0	0.0
Dissolved Oxygen (ml kg $^{-1}$)	4.18	6.83	28.5
Helium concentration (nmol kg $^{-1}$)	1.85	1.86	25.7
Neon concentration (nmol kg $^{-1}$)	8.03	8.22	89.2

2.1.3 Basal melt rate calculations

To estimate the basal melt rate, the same technique used for George VI Ice Shelf is employed (*Jenkins and Jacobs*, 2008). This method is based on the classical inverse method (*Wunsch*, 1978), and is also used to estimate the basal melt rates of Pine Island and Getz Ice Shelves (*Jenkins and Jacobs*, 2008; *Jacobs et al.*, 2011; *Nakayama et al.*, 2013; *Jacobs et al.*, 2013; *Dutrieux et al.*, 2014).

It is assumed that the ice front CTD sections effectively close off the cavity, and the total mass transport must satisfy

$$\sum_{j=1}^{n}(M_{out} - M_{in})_j = M_{melt}, \tag{2.5}$$

where M_{in}, M_{out} and M_{melt} are the mass transport of inflow, outflow and melt water, respectively, and n is the number of vertical velocity profiles between n+1 CTD stations. Assuming that cavity properties are in steady state, a similar equation must be satisfied for the transport of each tracer χ across the section:

$$\sum_{j=1}^{n}\{(M\chi)_{out} - (M\chi)_{in}\}_j = M_{melt}\chi_{MW}. \tag{2.6}$$

Combining the conservations of total mass transport and tracer transport, eqs (2.5) and (2.6) can be reduced to,

$$\sum_{j=1}^{n}\frac{1}{g}\int_{P_{bot}}^{P_{top}}(v_j^{adj} + \bar{v}(p))[\bar{\chi}(p) - \chi_{MW}]\Delta x(p)dp = 0, \tag{2.7}$$

where overbars indicate averages over the width Δx between stations, g is the acceleration due to gravity, p is pressure, v_j^{adj} is the barotropic reference velocity, and $\bar{v}(p)$ is the velocity obtained from the geostrophic balance. For the case shown in chapter 3, n equals to four with four unknown barotropic reference velocities, while there are only three equations for potential temperature, salinity, and dissolved oxygen. Since, this problem has many possible solutions, the solution that minimizes the sum of the squares of the barotropic reference velocities is chosen.

2.2 Model description

This section provides an introduction to the Finite-Element Sea-ice/ice-shelf/Ocean Model (FESOM). As FESOM is the main tool of the second and third part of this dissertation (chapters 4 and 5), the functioning of the model is briefly described here.

FESOM consists of a finite-element physical ocean circulation component, a dynamic-thermodynamic sea-ice component, and a thermodynamic ice-shelf component. The governing equations of the ocean, sea ice, and ice shelf are described separately in subsections 2.2.1, 2.2.2, and 2.2.4. Couplings between ocean and sea ice, and between ocean and ice shelf are described in subsections 2.2.3 and 2.2.5. Lastly, the discretization procedure for these equations is briefly explained in subsection 2.2.6. A more detailed description of FESOM can be found in *Timmermann et al.* (2009, 2012), *Timmermann and Hellmer* (2013), and *Wang et al.* (2014).

2.2.1 Ocean component

In the simulation of the ocean state, the evolution of the four main variables is modeled by the discretization of the governing equations. Those variables are

- $\mathbf{v} = (\mathbf{u}, w)$, the three-dimensional ocean velocity vector
- $\eta = \eta(x, y, t)$, the sea surface height of the ocean
- $S = S(x, y, z, t)$, the salinity of the sea water
- $T = T(x, y, z, t)$, the potential temperature of sea water.

The ocean component solves the standard set of hydrostatic primitive equations with the Boussinesq approximation. The system of governing equations can be divided into two subproblems, a dynamical part and a thermodynamical part, which are solved separately. The dynamical part solves the momentum equations, the vertically integrated continuity equation, and hydrostatic balance for pressure p as represented by

$$\partial_t \mathbf{u} + (\mathbf{v} \cdot \nabla_3)\mathbf{u} + f(\mathbf{k} \times \mathbf{u}) + g\nabla\eta + \frac{1}{\rho_0}\nabla p = \nabla \cdot A_h \nabla \mathbf{u} + \partial_z A_v \partial_z \mathbf{u}, \tag{2.8}$$

$$\partial_t \eta + \nabla \cdot \int_{z=-H}^{z=\eta} \mathbf{u} \, dz = P - E, \tag{2.9}$$

and

$$\partial_z p = -\rho g, \tag{2.10}$$

where $f = f(\theta)$ is the Coriolis parameter dependent on the latitude θ, $\mathbf{k}$ is the vertical unit vector, ρ_0 and ρ are the mean sea water density and the deviation from mean sea water density, respectively, A_h and A_v are the lateral and vertical momentum diffusion coefficients, respectively, and P and E are the precipitation and evaporation, correspondingly. The precipitation and evaporation fields are obtained from the National Centers for Environmental Prediction Climate Forecast System Reanalysis (NCEP-CFSR) data set (*Saha et al.*, 2010). ∇ and ∇_3 stand for the 2-dimensional and 3-dimensional gradient and divergence operators, respectively. Bottom drag is implemented by a quadratic function of bottom velocity with the drag coefficient of 2.5×10^{-3}. For the computation of density, the equation of state

$$\rho = \rho(T, S, z) \tag{2.11}$$

is applied, which relates in-situ density to potential temperature and salinity of sea water at given depth z.

For the thermodynamical part of the ocean component, potential temperature T, salinity S, and any passive tracer C are calculated from the tracer evolution equations

$$\partial_t T + \mathbf{v} \cdot \nabla_3 T = \nabla \cdot K_h \nabla T + \partial_z K_v \partial_z T, \tag{2.12}$$

$$\partial_t S + \mathbf{v} \cdot \nabla_3 S = \nabla \cdot K_h \nabla S + \partial_z K_v \partial_z S, \tag{2.13}$$

and

$$\partial_t C + \mathbf{v} \cdot \nabla_3 C = \nabla \cdot K_h \nabla C + \partial_z K_v \partial_z C, \tag{2.14}$$

where K_h and K_v are the horizontal and vertical diffusion coefficients, respectively. The horizontal diffusivity K_h is calculated as a linear function of the element area Δ_i as $K_h = 4.0 \times 10^{-7} k_h \Delta_i$, where i and k_h is the number of the element and the scaling factor for diffusion, respectively. In this study, k_h is set to 0.9 for the CTRL case in chapters 4 and 5, and 0.45 and 0.05 for the sensitivity studies in chapter 4. For the case with a horizontal resolution of 5 km, for example, horizontal diffusivity is calculated to be about 5 m^2 s^{-1}. The vertical diffusivity K_v is calculated using a Pacanowski-Philander type vertical mixing scheme (*Pacanowski and Philander*, 1981).

In the initial state, ocean velocity is set to zero. The initial conditions for salinity and potential temperature are taken from a climatological data set, which will be discussed later in chapter 4.

2.2.2 Sea-ice component

In the simulation of the sea-ice state, sea ice is assumed to be a two dimensional, quasi continuous fluid. The evolution of the four main variables is modeled by the discretization of the governing equations. These variables are

- $h = h(x, y, t)$ mean ice thickness, defined as the ice volume per unit area averaged over the ice covered and ice-free part of the element
- $h_s = h_s(x, y, t)$ mean snow thickness, defined in the same way as h
- $A = A(x, y, t)$ sea-ice concentration, a dimensionless quantity ranging from zero to one specifying the fraction of the ice-covered area of an element
- $\mathbf{u}_{ice} = \mathbf{u}_{ice}(x.y, t)$ ice (and snow on sea ice) drift velocity.

The model includes a snow layer (*Owens and Lemke*, 1997). The transformation of snow to ice by flooding of sea water is considered (*Leppäranta*, 1983; *Fischer*, 1995), but snow redistribution by winds is not considered. Linear temperature profiles are assumed in both layers applying the zero-layer approach of *Semtner Jr.* (1976), and thus, heat storage within ice or snow is not considered. The evolution of the quantities h, h_s, and A is described by the continuity equations,

$$\partial_t h + \nabla \cdot (\mathbf{u}_{ice}\, h) = S_h, \tag{2.15}$$

$$\partial_t h_s + \nabla \cdot (\mathbf{u}_{ice}\, h_s) = S_{sn}, \tag{2.16}$$

and

$$\partial_t A + \nabla \cdot (\mathbf{u}_{ice}\, A) = S_A, \tag{2.17}$$

where S_h, S_{sn}, and S_A are the source and sink terms representing thermodynamic processes (freezing and melting), snow fall and snow to ice transformation.

The horizontal ice drift velocity $\mathbf{u}_{ice}$ is computed from the 2-dimensional momentum equation,

$$m\left(\partial_t + f\mathbf{k}\times\right)\mathbf{u}_{ice} = A\left(\boldsymbol{\tau}_{ai} + \boldsymbol{\tau}_{oi}\right) + \mathbf{F} - mg\nabla\eta., \tag{2.18}$$

where m is the ice mass per unit area, $\boldsymbol{\tau}_{ai}$ and $\boldsymbol{\tau}_{oi}$ are the air-ice and ice-ocean stresses, respectively. The term $\mathbf{F} = \nabla \cdot \boldsymbol{\sigma}$ accounts for the effect of internal stresses, where $\boldsymbol{\sigma}$ is a stress tensor that depends on the deformation field. For the computation of $\mathbf{F}$, sea ice is treated as a nonlinear elastic-viscous-plastic compressible fluid following *Hunke and Dukowicz* (1997) and *Hunke and Lipscomb* (2010). The ice mass m can be represented by $m = \rho_i h + \rho_{sn} h_s$, where $\rho_i = 910$ kg/m^3 stands for the density of ice and $\rho_{sn} = 290$ kg/m^3 stands for the density of snow.

The wind stress term in eq. 2.18 depends on the wind velocity at 10 m height, $\mathbf{u}_{10}$, using

$$\boldsymbol{\tau}_{ai} = C_{d,ai}\,\rho_a\,\mathbf{u}_{10}|\mathbf{u}_{10}|, \tag{2.19}$$

where $C_{d,ai}$ stands for the ice-atmosphere drag coefficient and $\rho_a = 1.3$ kg/m^3 stands for the air density. The ice velocity is small compared to the wind velocity and is thus ignored in the above equation. The atmosphere-ice drag coefficient is set to $c_{d,ai} = 1.0 \times 10^{-3}$ in this study, following *Holland et al.* (2010) in which they simulated the ice and ocean processes in the Bellingshausen Sea.

The exchange of momentum between the ocean surface and the sea ice is expressed by

$$\boldsymbol{\tau}_{io} = C_{d,io}\,\rho_0\left(\mathbf{u}_{ice} - \mathbf{u}_s\right)|\mathbf{u}_{ice} - \mathbf{u}_s|, \tag{2.20}$$

where $C_{d,io}$ stands for the ice-ocean drag coefficient. The ocean surface velocity $\mathbf{u}_s$ is taken from the ocean component as part of the coupling scheme. The ice-ocean drag coefficient is set to $c_{d,io} = 5.0 \times 10^{-3}$ in this study.

These governing equations (eqs. 2.15-2.18) are solved as follows. First, the momentum equations are solved for ice velocity. Second, the continuity equations are solved assuming that source and sink terms (S_h, $S_s n$, and S_A) are zero to obtain preliminary values for sea ice thickness and snow thickness and ice concentration. Finally, these variables are updated by accounting for the thermodynamic source and sink terms following the surface heat budget.

For the surface heat budget, the heat flux to the atmosphere Q_a is represented by,

$$Q_a = Q_{sw} + Q_{lw} + Q_s + Q_l, \tag{2.21}$$

where Q_{sw}, Q_{lw}, Q_s, and Q_l refer to the shortwave radiative heat flux, the longwave radiative heat flux, the sensible heat flux and the latent heat flux, respectively. All heat flux components are calculated as net upward heat fluxes and the heat loss to the atmosphere is positive in this notation.

Upward shortwave and longwave radiations are calculated as

$$Q_{sw} = (\alpha - 1)Q_{sw}^{\downarrow} \tag{2.22}$$

and

$$Q_{lw} = -Q_{lw}^{\downarrow}, \tag{2.23}$$

where $Q_{sw}^{\downarrow}$ and $Q_{lw}^{\downarrow}$ are the downward shortwave and longwave radiations from the NCEP-CFSR dataset, respectively, and α is the surface albedo. For one of the sensitivity studies in chapter 4, NCEP/NCAR reanalysis forcing is used instead of the NCEP-CFSR data. For this case, shortwave and longwave radiations are calculated using empirical equation from *Zillman* (1972) and the Stefan-Boltzmann-Law, respectively.

The sensible heat flux is determined by the ocean-atmosphere temperature difference and the 10-m wind speed u_{10} as represented by

$$Q_s = c_p \, \rho_a \, C_s \, u_{10} \cdot (T_s - T_a), \tag{2.24}$$

where c_p, C_s, and T_s are the specific heat of air, the heat transfer coefficient for sensible heat, and the surface potential temperature, correspondingly. For this study, C_s is set to 1.75×10^{-3} over ice, snow and water following (*Maykut*, 1977; *Parkinson and Washington*, 1979). For open water, T_s is the temperature of the ocean model surface layer. For sea ice, T_s is obtained as part of the diagnostic computation of the sea ice surface energy budget.

The latent heat flux is calculated using wind speed and the difference between the specific humidities at the surface q_s (where saturation is assumed) and at 2 m height q_a as shown by

$$Q_l = L_e\ \rho_a\ C_l\ u_{10} \cdot (q_s - q_a), \tag{2.25}$$

where L_e and C_l are the latent heat of evaporation and the heat transfer coefficient for latent heat, respectively. For this study, C_l is set to 1.75×10^{-3} over ice, snow and water following (*Maykut*, 1977; *Parkinson and Washington*, 1979).

All heat flux components are calculated separately for the ice-covered and the ice-free part of each element and weighted with sea-ice concentration, A and $(1 - A)$. The growth rates of sea ice can be calculated to be

$$(\partial_t h)_{ow} = -\frac{Q_{ao}}{\rho_i L_i}. \tag{2.26}$$

for the ice-free area and

$$\partial_t h_s = -\frac{Q_{ai}}{\rho_{sn} L_i}, \tag{2.27}$$

and

$$(\partial_t h)_a = -\frac{Q_{ai}}{\rho_i L_i} - \partial_t h_s, \tag{2.28}$$

for the ice and snow covered area, where Q_{ao} and Q_{ai} are the heat flux over open ocean and ice covered area, respectively, and $(\partial_t h)_{ow}$, $\partial_t h_s$, and $(\partial_t h)_a$ are the growth rate of sea ice in open water, the change of snow thickness, and the change of ice thickness, respectively. L_i is the latent heat of fusion. Here we assume that the snow melt first under surface melting conditions. In addition, melting and freezing occur at the base of ice. The rate of melting or freezing is calculated to be

$$(\partial_t h)_o = -\frac{Q_{oi}}{\rho_i L_i}, \tag{2.29}$$

where Q_{oi} is heat flux between ocean and ice (see eq. 2.30).

2.2.3 The coupling of ocean and sea-ice components

The ocean and sea ice models are coupled via heat exchange, salt flux due to the effects of net precipitation and of melting and freezing of ice and snow, and momentum exchange.

The heat flux between ocean and sea ice is given by

$$Q_{oi} = \rho_w \, c_{p,w} \, C_{h,io} u^*_{io} (T_s - T_f), \tag{2.30}$$

where $c_{p,w}$ stands for the specific heat capacity of seawater at constant pressure, $C_{h,io}$ stands for the transfer coefficient of the exchange of sensible heat between the ocean and the bottom side of the ice, and T_f stands for the freezing temperature of sea water. The transfer coefficient $C_{h,io}$ is set to 1.2×10^{-2} in this study.

The friction velocity u^*_{io} between ice and ocean is computed as

$$u^*_{io} = C^{1/2}_{d,io} |\mathbf{u}_s - \mathbf{u}_{ice}|, \tag{2.31}$$

where $C_{d,io}$ denotes the oceanic drag coefficient and $\mathbf{u}_s$ denotes the ocean velocity of the surface layer.

In the model, melting and freezing result in a virtual salt flux $\mathcal{F}^{salt}_{ice}$, which is described by

$$\mathcal{F}^{salt}_{ice} = (S_s - S_{ice}) \frac{\rho_i}{\rho_w} (\partial_t h)_{th} + S_s \frac{\rho_{sn}}{\rho_w} (\partial_t h_s)_{th}. \tag{2.32}$$

The first term describes the salt flux due to thermodynamic changes in the ice thickness, while the second term considers the snow thickness. The ice salinity, S_{ice}, is set to a constant value of 5 psu in the model, with the salinity of snow assumed to be zero.

The difference of precipitation and evaporation ($P - E$) also provides a source of freshwater. If the air temperature is above the freezing point ($T_a \geq 0°C$), the precipitation runs completely into the ocean. For $T_a < 0°C$, the precipitation on the ice-covered area of the grid cell is accumulated as snow. Therefore, the salinity flux due to $P - E$, $\mathcal{F}^{salt}_{P-E}$ is given by

$$\mathcal{F}^{salt}_{P-E} = S_s \cdot \begin{cases} P - E & \text{if } T_a \geq 0°C \\ (1 - A) \cdot (P - E) & \text{if } T_a < 0°C \end{cases} \tag{2.33}$$

The salt flux from snow-to-ice conversion by flooding $\mathcal{F}^{salt}_{fl}$ is represented by,

$$\mathcal{F}^{S}_{fl} = S_{ice} \, \frac{\rho_i}{\rho_w} (\partial_t h_i)_{fl}, \tag{2.34}$$

where $(\partial_t h_i)_{fl}$ is sea ice thickness change due to flooding.

The total virtual salt flux into the surface layer of the ocean model can be represented by

$$\mathcal{F}^{salt} = \mathcal{F}^{salt}_{ice} + \mathcal{F}^{salt}_{P-E} + \mathcal{F}^{salt}_{fl}. \tag{2.35}$$

The exchange of momentum between ice and ocean is computed by

$$\boldsymbol{\tau}_{io} = C_{d,io} \, \rho_o \, (\boldsymbol{u}_{ice} - \mathbf{u}_s) |\boldsymbol{u}_{ice} - \mathbf{u}_s|, \tag{2.36}$$

where $C_{d,io}$ stands for the ice-ocean drag coefficient. The stress between the open ocean surface and the atmosphere is

$$\boldsymbol{\tau}_{ao} = \rho_a \, C_{d,ao} \, \boldsymbol{u}_{10} |\boldsymbol{u}_{10}|, \tag{2.37}$$

where $C_{d,ao}$ is the atmosphere-ocean drag coefficient. The total ocean surface stress is the weighted average of the two terms:

$$\boldsymbol{\tau}_o = A \cdot \boldsymbol{\tau}_{io} + (1 - A) \cdot \boldsymbol{\tau}_{ao}. \tag{2.38}$$

2.2.4 Ice-shelf component

For the ice-shelf component, basal melt water and heat fluxes are calculated. Following *Timmermann et al.* (2012), a steady state for ice shelf thickness and cavity geometry is assumed. Basal mass loss rates at ice-shelf bases is computed as proposed by *Hellmer and Olbers* (1989) and refined by *Holland and Jenkins* (1999), which is based on a three-equation scheme, based on conservation equations of heat and salinity in a thin boundary layer between ice and ocean and the pressure-depending linearized equation for the in-situ freezing point (*Foldvik and Kvinge*, 1974),

$$\rho_{fw}\dot{m}L_i - K_i\frac{T_{is}-T_b}{D} = \rho_w c_{p,w}\gamma_T(T_s - T_b), \tag{2.39}$$

$$\rho_{fw}\dot{m}S_b = \rho_w\gamma_S(S_s - S_b), \tag{2.40}$$

and

$$T_b = -0.0575S_b + 0.0901 - 7.61\times10^{-4}d, \tag{2.41}$$

where ρ_{fw} and ρ_w are the densities of fresh water and sea water, respectively, γ_S and γ_T are the salt and heat transfer coefficients, respectively, T_s, S_s, T_b, and S_b are the potential temperatures and salinities in the uppermost layer of the model and in the boundary layer at the ice shelf base, respectively, and $\dot{m}$, K_i, T_{is}, D, and d are the melt rate, the thermal conductivity of ice, the temperature at the surface of the ice shelf, the ice shelf thickness, and the depth of ice shelf base, respectively. The potential temperature at ice shelf surface T_{is} is set to be -20 °C. Turbulent fluxes of heat and salt are computed with coefficients depending on the friction velocity following *Jenkins* (1991),

$$\gamma_S = \frac{u^*_{is}}{2.12\ln(u^*_{is}h/\nu) + 12.5Sc^{2/3} - 9} \tag{2.42}$$

$$\gamma_T = \frac{u^*_{is}}{2.12\ln(u^*_{is}h/\nu) + 12.5Pr^{2/3} - 9} \tag{2.43}$$

, where u^*_{is}, h, ν, Sc, and Pr are friction velocity at the the ocean-ice shelf interface (uppermost layer of the model), the thickness of the boundary layer, the kinematic viscosity of sea water, and the Schmidt and Prandtl numbers, respectively. Following *Jenkins* (1991), Sc and Pr are set to 2432 and 13.8. The drag coefficient between ice shelf base and ocean is set to $C_{d,ib} = 2.5\times10^{-3}$. The friction velocity at the ocean-ice shelf interface u^*_{is} is represented by

$$u^*_{is} = C^{1/2}_{d,io}|\mathbf{u}_s|, \tag{2.44}$$

where $\mathbf{u}_s$ is the ocean velocity of the element close to the ocean-ice shelf interface.

2.2.5 The coupling of ocean and ice-shelf components

To couple the ice-shelf component to the ocean model, salinity flux and heat flux are transferred between ocean and ice sheet components after each time step. The salinity flux at the base of the ice shelf cavity is given as,

$$\mathcal{F}^S = -S_s \dot{m}, \tag{2.45}$$

where S_s is the salinity of the element at the ocean-ice shelf interface. The heat flux at the base of the ice shelf cavity is given as,

$$Q_o = \rho_w c_{p,w} \gamma_T (T_s - T_b), \tag{2.46}$$

where T_s is the salinity of the element at the ocean-ice shelf boundary.

In addition, a passive tracer flux is also included to visualize the spreading of glacial melt water. The flux of the passive tracer at the ice shelf base is set to the melt water production rate ($\dot{m}$). Concentrations of passive tracers are set to zero everywhere in the beginning of the experiments. Several independent virtual passive tracers are used to identify detailed pathways of basal melt water from ice shelves in the AS and BS.

2.2.6 Discretization

The finite element method is a method of numerical discretization that is not commonly applied in global ocean modeling. While the size of the time step in FESOM is fixed, the finite element mesh for the spatial domain is an unstructured triangular grid on the ocean surface. The use of unstructured grids makes the model resolution highly adjustable. This is a great advantage for ocean modeling with complex coastlines and bathymetry, because some of the small scale bathymetric features, which can only be resolved in a fine resolution, are crucial for reproducing realistic ocean circulation. This approach can also be used for studies with specific regional focus, which allows for the investigation of the impact of the basal melting flux of small ice shelves on the large scale ocean circulation in this study.

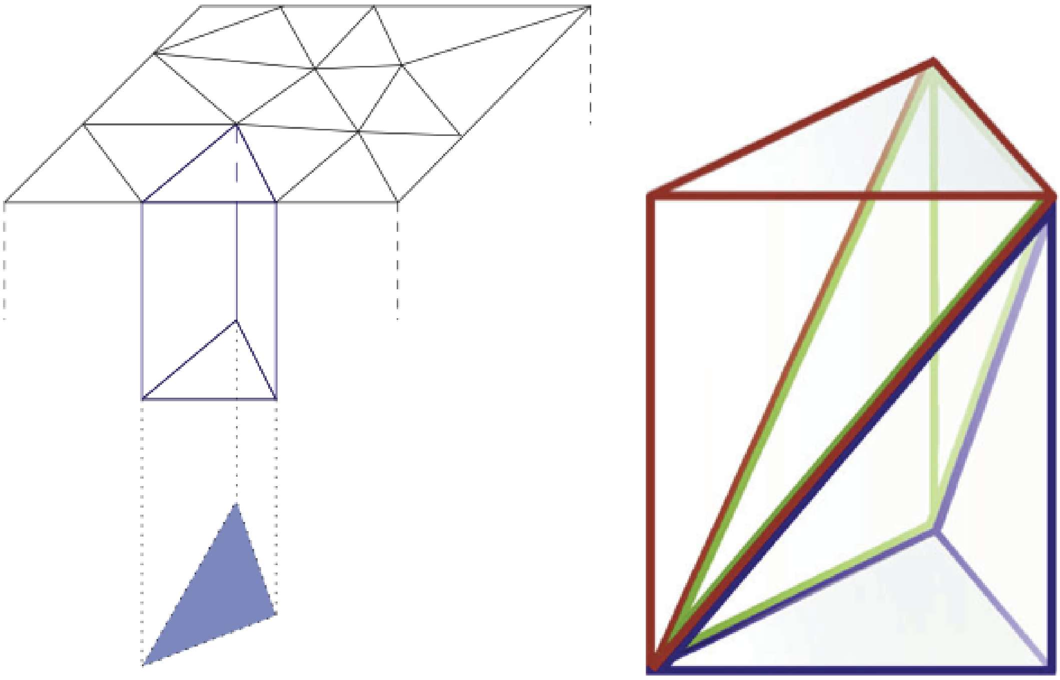

Figure 2.2: Illustration of the three dimensional structure of the FESOM mesh. Grid nodes in the interior ocean are aligned under the surface triangles (left). Each of the resulting prisms is split into three tetrahedra (right). Figure from *Timmermann et al.* (2009)

The computational mesh for the ocean component is composed of tetrahedra, as already mentioned, based on an unstructured surface triangular grid. To allow for an adequate representation of ice shelf cavities, a hybrid vertical coordinate system with 46 layers and a z-level discretization in the mid- and low-latitude ocean basins is applied. The top 21 layers are terrain-following (sigma coordinate) for depths shallower than 650 m along the Antarctic coast. Each surface triangle defines a prism that is cut into smaller prisms by vertical discritization (Fig. 2.2). Each small prism is then split into three tetrahedra. In order to avoid a stepwise bottom and to approximate bathymetry in a smooth way with realistic depths, nodes of bottom elements are allowed to deviate from z-levels.

Time derivatives are approximated by finite differences, while spatial derivatives are computed using the finite element method. For the representation of model variables, linear basis functions for horizontal velocity, tracer variables, and surface elevation are used, leading to a continuous linear representation of model variables. Basis functions Ψ_j are equal to 1 at node j and linearly go to 0 at the neighboring nodes. They are zero outside the cluster of neighboring elements. Using these basis functions, any field a is expressed as $a = \Sigma a_j \psi_j$, where a_j are the nodal values, located on the corners of the tetrahedra. The solution can be obtained by inserting the approximated solution a into the governing equations formulated into the weak form. Details of the spatial and temporal discretization can be found in *Timmermann et al.* (2009) and *Wang et al.* (2014).

3

From circumpolar deep water to the glacial meltwater plume on the eastern Amundsen Shelf

Yoshihiro Nakayama, Michael Schröder, and Hartmut H. Hellmer

Alfred Wegener Institute, Helmholtz Centre for Polar and Marine Research
in Bremerhaven, Germany

Journal of Deep Sea Research Part I, 77 (2013), 50-62

Y. Nakayama conducted the significant part of the analysis and interpretation of the hydrographic data. The hydrographic observations were conducted by M. Schröder. Y. Nakayama wrote all the text of the paper and prepared all the figures. All authors participated in the discussion of the data interpretation and revision of the paper.

Deep-Sea Research I 77 (2013) 50–62

Contents lists available at SciVerse ScienceDirect

Deep-Sea Research I

journal homepage: www.elsevier.com/locate/dsri

From circumpolar deep water to the glacial meltwater plume on the eastern Amundsen Shelf

Y. Nakayama*, M. Schröder, H.H. Hellmer

Alfred Wegener Institute for Polar and Marine Research, Bussestrasse 24, D-27570 Bremerhaven, Germany

ARTICLE INFO

Article history:
Received 27 August 2012
Received in revised form
26 March 2013
Accepted 1 April 2013
Available online 17 April 2013

Keywords:
Circumpolar deep water
Ocean-ice shelf interaction
Ice shelf basal melting
Amundsen Sea

ABSTRACT

The melting of Pine Island Ice Shelf (PIIS) has increased since the 1990 s, which may have a large impact on ice sheet dynamics, sea-level rise, and changes in water mass properties of surrounding oceans. The reason for the PIIS melting is the relatively warm (~1.2 °C) Circumpolar Deep Water (CDW) that penetrates into the PIIS cavity through two submarine glacial troughs located on the Amundsen Sea continental shelf. In this study, we mainly analyze the hydrographic data obtained during ANTXXVI/3 in 2010 with the focus on pathways of the intruding CDW, PIIS melt rates, and the fate of glacial meltwater. We analyze the data by dividing CTD profiles into 6 groups according to intruding CDW properties and meltwater content. From this analysis, it is seen that CDW warmer than 1.23 °C (colder than 1.23 °C) intrudes via the eastern (central) trough. The temperature is controlled by the thickness of the intruding CDW layer. The eastern trough supports a denser CDW layer than the water mass in Pine Island Trough (PIT). The eastern intrusion is modified on the way into PIT through mixing with the lighter and colder CDW from the central trough. Using ocean transport and tracer transport calculations from the ice shelf front CTD section, the estimated melt rate in 2010 is ~30 m yr^{-1}, which is comparable to published values. From spatial distributions of meltwater content, meltwater flows along the bathymetry towards the west. When compared with earlier (2000) observations, a warmer and thicker CDW layer is observed in Pine Island Trough for the period 2007–2010, indicating a recent thickening of the CDW intrusion.

1. Introduction

Pine Island Glacier (PIG) and Thwaites Glacier (TG) are the major ice streams of the West Antarctic Ice Sheet (WAIS), draining around 393,000 km^2, about 25% of the total area, and driving the largest ice loss of the Antarctic ice sheet (e.g. Shepherd et al., 2001; Rignot et al., 2002, 2008, 2011; Wingham et al., 2009; Joughin and Alley, 2011; Shepherd et al., 2012). The observed ice velocity of the PIG has increased since the 1990s even far inland (exceeding 3.5 km yr^{-1} close to the grounding line), leading to the thinning and further acceleration of the PIG (Shepherd et al., 2001; Vaughan et al., 2006; Rignot et al., 2011).

The reason for the large ice loss is increased basal melting due to the interaction of deep-drafted ice shelves with Circumpolar Deep Water (CDW) which is about 3 °C warmer than the surface freezing point (e.g. Jacobs et al., 2011; Pritchard et al., 2012). This relatively warm water flows onto the continental shelf through submarine glacial troughs (Jacobs et al., 2011). Possible pathways of the intrusion have been studied. Walker et al. (2007) reported onshore flow of CDW through the central trough (C, Fig. 1). However, measurements were only conducted at the entrance of trough C due to heavy sea-ice conditions further south, and it is still unknown whether CDW penetrates all the way south to the Pine Island Ice Shelf (PIIS) cavity from trough C. Numerical model results with the most realistic topography available (Nitsche et al., 2007) show that CDW enters the continental shelf mainly through the eastern trough (E, Fig. 1) as a result of an onshore baroclinic eddy transport of warm water and reaches the PIIS cavity (Schodlok et al., 2012). However, there has not been any observation determining the pathway of CDW intrusions.

When this warm water reaches the grounding line, it melts the glacier and forms a buoyant plume of CDW and meltwater. This plume flows out from the ice shelf cavity and drives the continuous intrusion of CDW into the PIIS cavity where it follows an almost clockwise circulation (Payne et al., 2007). The meltwater outflow along the PIIS front is observed at the depth of 100–500 m (Jacobs et al., 1996; Hellmer and Jacobs, 1998; Jenkins et al., 2010; Jacobs et al., 2011). Most recent results show that the averaged melt rate in 2009 is estimated to be about 30 m yr^{-1} (Jacobs et al., 2011) and melting close to the grounding line can be as high as 80–100 m yr^{-1} (Payne et al., 2007; Heimbach and Losch, 2012).

The melting of PIIS and other ice shelves of the WAIS can have large impacts on the global ocean. First, the WAIS has the potential

---

* Corresponding author. Tel.: +49 471 4831 1876.
E-mail addresses: Yoshihiro.Nakayama@awi.de (Y. Nakayama), Michael.Schroeder@awi.de (M. Schröder), Hartmut.Hellmer@awi.de (H.H. Hellmer).

0967-0637/$ - see front matter © 2013 Elsevier Ltd. All rights reserved.
http://dx.doi.org/10.1016/j.dsr.2013.04.001

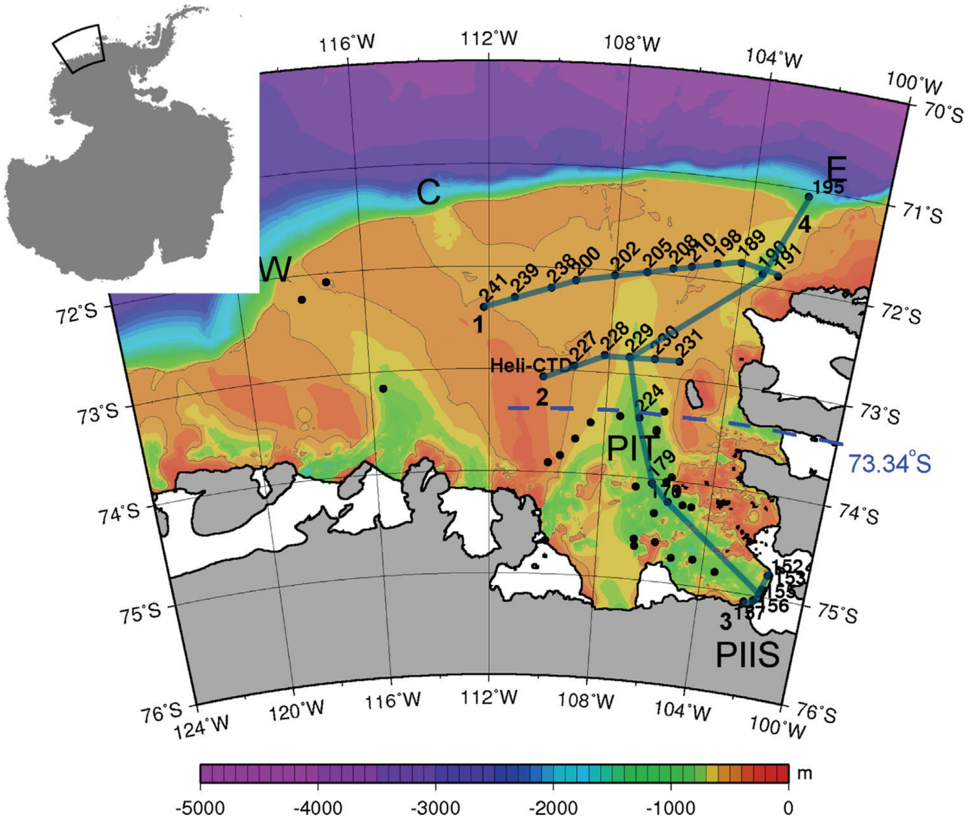

Fig. 1. Distribution of CTD stations in the eastern Amundsen Sea of the cruise in 2010 (ANTXXVI/3) with bathymetry and coastline (gray shade). The 500-m contour is also shown. The upper-left panel shows Antarctica with the enclosed region denoting the location of enlarged portion. Solid dots indicate the position of CTD stations and lines marked 1–4 are the sections discussed in this paper. The location of Pine Island Ice Shelf (PIIS) and Pine Island Trough (PIT) are shown. Letters E, C, and W denote the submarine glacial troughs located on the eastern, central, and western Amundsen Sea continental shelf. The latitude 73.34°S is shown (blue dashed line). Spatial variability of θ–S profiles south of 73.34°S is much smaller than to the north of it. (For interpretation of the references to color in this figure legend, the reader is referred to the web version of this article.)

to raise global sea level by 3.3 m (Bamber et al., 2009), and 10% of the observed sea level rise has been attributed to the thinning of the WAIS (Rignot et al., 2008). Second, it may cause the freshening of the shelf water locally in the Amundsen Sea as well as remotely in the Ross Sea (Jacobs et al., 2002). This may lead to a change in the characteristics of the Antarctic Bottom Water (AABW) formed in the Ross Sea (Jacobs et al., 2002; Rintoul, 2007) and thus may influence the global thermohaline circulation. Therefore, investigations related to the PIIS melting and its impact on the ocean is crucial for understanding climate change in the Southern Ocean.

Due to an extremely low sea-ice coverage on the whole Amundsen Sea continental shelf in austral summer 2010, we were able to conduct CTD measurements during ANTXXVI/3 in its whole eastern region, including the two submarine glacial troughs that may channel CDW beneath the PIIS. Such data is essential to determine the routes of CDW into the PIIS cavity and to detect freshwater input due to ice shelf basal melting. In this study, we analyze hydrographic data focusing on the pathway of CDW into the PIIS cavity, the PIIS melt rate in 2010, and the spreading of the meltwater plume on the Amundsen Sea continental shelf.

2. Data and methods

Sampling was carried out during ANTXXVI/3 from the research ice breaker Polarstern (Gohl, 2010). In total 62 CTD profiles shown in Fig. 1 were collected on this cruise including one Heli-CTD measurement.

The measurements use a Seabird 911+ CTD (SN 561) connected to a caroussel (SBE 32, SN 202) with 24-(12-l) water bottles. This instrument system contains two sensor pairs of conductivity (SBE 4, SN 3607, SN 3590) and temperature (SBE 3, SN 1373, SN 2629), a high precision pressure sensor Digiquartz 410K-105 (SN 68997), one oxygen sensor (SBE 43, SN 743 until station no. 143 and SN 880 from station no. 147 on), one oxygen sensor (Rinko SN 10, optode), a fluorometer (Wetlab ECO-AFL/FL, SN 1365), and a Benthos altimeter Model PSA 916 (SN 1228).

The conductivity and temperature sensor calibrations were performed before and after the cruise at Seabird Electronics. The accuracy of the temperature sensors is 2 mK. The readings for the pressure sensors are better than 2 dbar. The conductivity was corrected using salinity measurements from water samples. IAPSO Standard Seawater from the P-series P149 (K15 = 0.99984) was used. A total of 77 water samples were measured using a Guildline Autosal 8400B. On the basis of the water sample correction, salinity is measured to an accuracy of 0.002. The oxygen was corrected from water samples using the Winkler method with a Dissolved Oxygen Analyser (DOA, built by Sensoren Instrumente Systeme, Germany).

For the identification of meltwater, a few helium and neon samples were taken from the water samples of the CTD casts at the PIIS front section (Fig. 1). They were all sealed in copper tubes and analyzed by mass spectrometer at the IUP Bremen (Sültenfu et al., 2009). The accuracy of measurements is 0.01 nmol kg^{-1} or 1% for He and 0.04 nmol kg^{-1} or 1% Ne, determined from the large number of observations in the western Weddell Sea (Huhn et al., 2008).

In the latter part of the analysis, Nathaniel B. Palmer CTD data from 2000, 2007, and 2009 is used to discuss the temporal variabilities. All data sets we use are taken in austral summer between January and

March, because no observations have been conducted in winter time in the Amundsen Sea up to now.

3. Results

3.1. Observational results

The potential temperature, salinity, and dissolved oxygen for Sections 1 and 2 (Figs. 2 and 3) mainly show Winter Water (WW) with the potential temperature minimum at 100–300 m and warm CDW from 300 to 400 m to the bottom. The north–south section (Fig. 4), which connects the deepest stations of each east–west section (Fig. 1), shows that CDW clearly dominates the lower part of the water column, and that CDW is continuously supplied to the PIIS cavity. A similar result is presented in Jacobs et al. (2011) from their observations in 2009. Along the surface-referenced isopycnal of 27.7, CDW with the potential temperature of 1 °C, salinity of 34.5, and dissolved oxygen of 4.2 ml kg^{-1} flows onto the continental shelf and into the PIIS cavity. The maximum isopycnal that reaches the PIIS is ~27.79. The 27.8-isopycnal advances to the center of a bathymetric trough, which extends to the PIIS and is colored in yellow and green in Fig. 1. Following Jakobsson et al. (2011), we name this trough Pine Island Trough (PIT). The deep water column at the PIIS front is filled with CDW, overlain by the outflowing mixture of meltwater and CDW (Fig. 5).

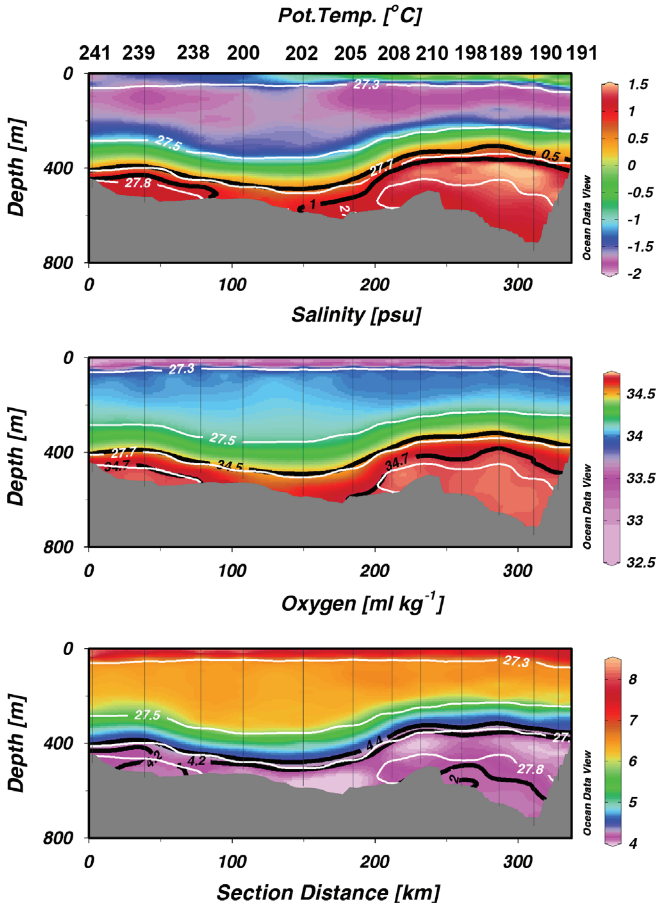

Fig. 2. Vertical sections of potential temperature (top), salinity (middle), and dissolved oxygen (bottom) of Section 1 shown by colors and thick black contours. Surface referenced potential density is indicated by white contours in all panels. The vertical black lines mark the location of CTD profiles with station numbers shown at the top. Bottom topography is based on Rtopo-1 (Timmermann et al., 2010). West is on the left side of the panel. (For interpretation of the references to color in this figure legend, the reader is referred to the web version of this article.)

3.2. Typical θ–S profiles observed on the eastern Amundsen Sea continental shelf

To analyze the intrusion of CDW and spreading of meltwater, we have color-coded the CTD stations on the Amundsen Sea continental shelf. We use maximum potential temperature (T_{max}) and specific meltwater fraction (0.6%), calculated using potential temperature and salinity, to define the color-codes (Table 1). For the calculation of the meltwater fraction (see Appendix A), water mass characteristics are defined for CDW, WW, and meltwater following Jenkins (1999), Jenkins and Jacobs (2008), and Jacobs et al. (2011), summarized in Table 2.

Since the θ–S profiles of color-coded stations (Fig. 6) represent water columns from 100 m to the bottom, the shallower parts represent WW properties while the deeper parts show CDW properties. The profiles with meltwater fraction higher than 0.6% are color-coded green and the ice front profiles are color-coded cyan (Table 1). For all the non-green and non-cyan profiles, two different regimes are observed; θ–S profiles north of 73.34°S show large spatial variability which is much smaller for θ–S profiles south of 73.34°S. Thus, we define all the non-green and non-cyan profiles south of 73.34°S (dashed blue line in Fig. 1) as the blue group, representing the typical profiles of the PIT (Fig. 7a). Other northern profiles are color-coded red, pink, or orange according to the T_{max} (Table 1 and Fig. 7b–d). From the definition of the color-code (Table 1), the green and cyan profiles have higher meltwater fraction at shallower depth than the blue profiles, but their CDW properties are similar (Fig. 7e and f). The blue profiles have the maximum potential temperature of ~1.13–1.23 °C (Fig. 6). The red (orange) group has warmer (colder)

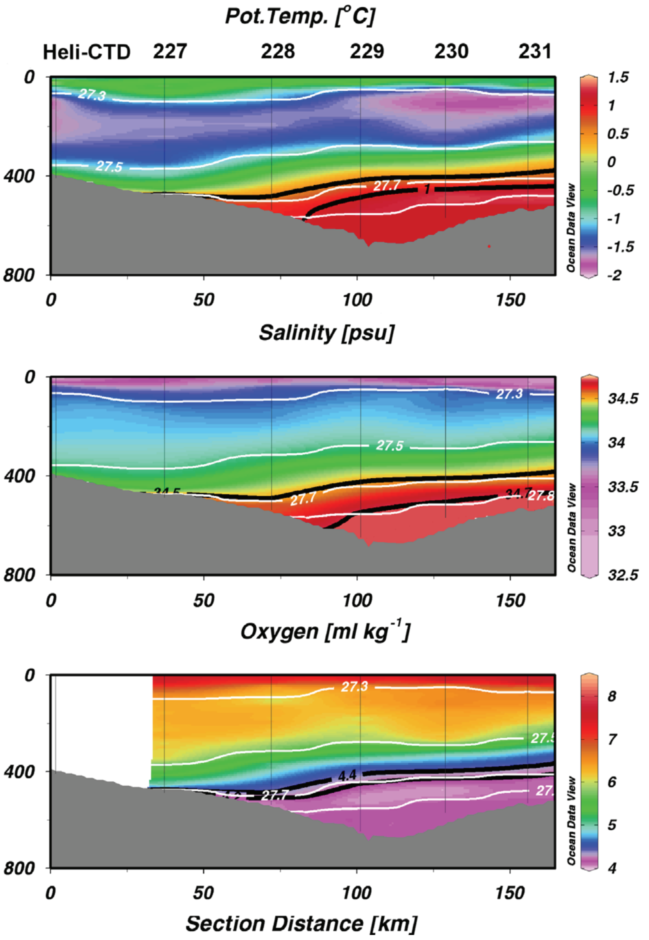

Fig. 3. Same as Fig. 2 but along Section 2. The vertical section of dissolved oxygen (bottom) is shorter, because dissolved oxygen was not measured with the heli-CTD.

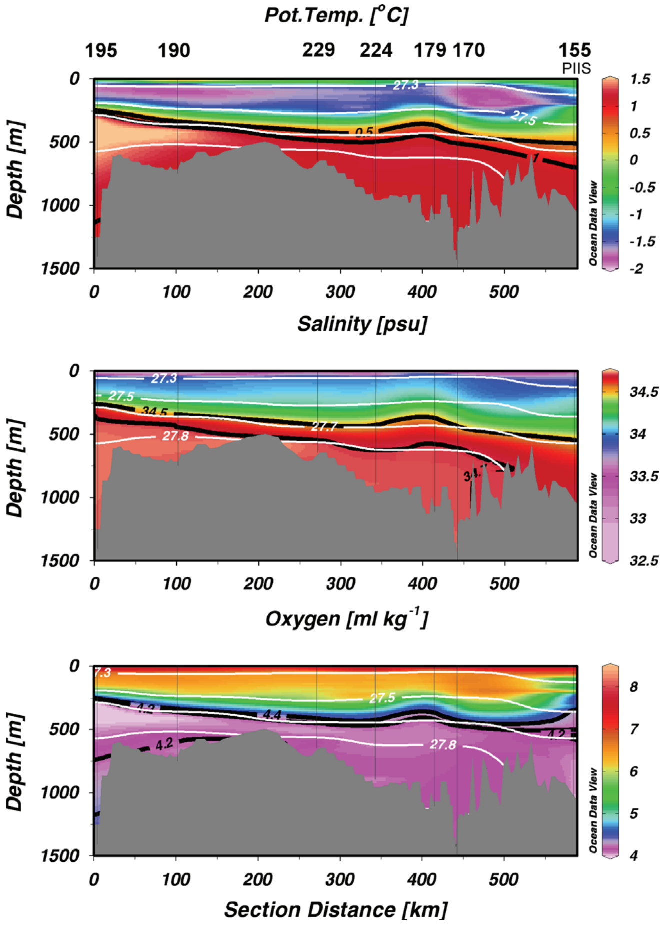

Fig. 4. Same as Fig. 2 but along Section 4. North (continental slope) is on the left side of the panel.

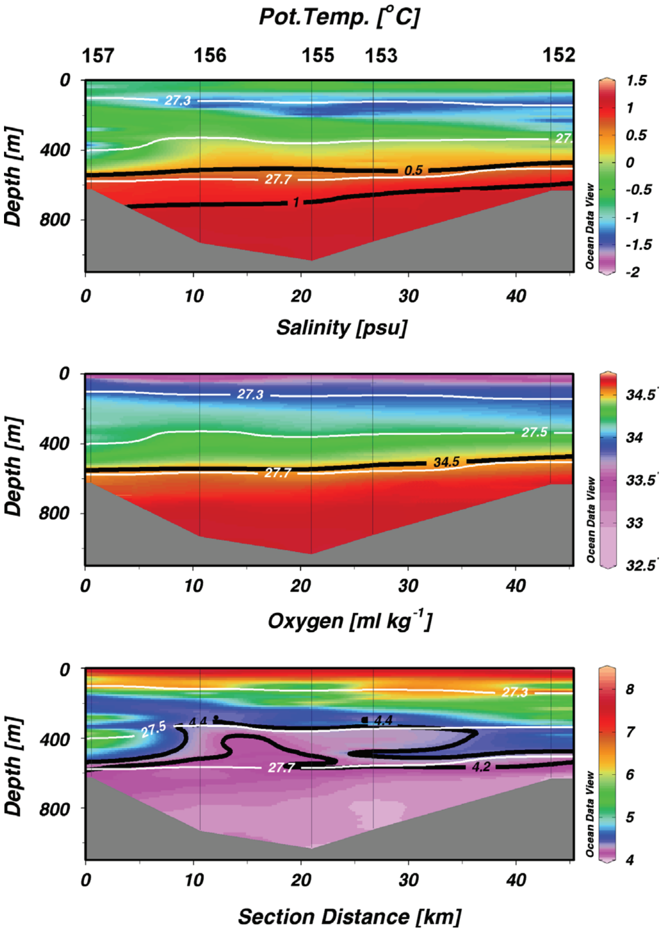

Fig. 5. Same as Fig. 2 but along Section 3. Bottom topography is drawn from the observed depth at the CTD stations. North is the right side of the panel.

Table 1
Definition of the color code used for the eastern Amundsen Sea continental shelf.

Color	Definition
Cyan	Profiles observed at PIIS front
Green	Meltwater fraction exceeding 0.6% in the salinity range of 34.0–34.4
Blue	Non-green and non-cyan profiles south of 73.34°S
Red	Non-green profiles north of 73.34°S and 1.23 °C $< T_{max}$
Pink	Non-green profiles north of 73.34°S and 1.13 °C $< T_{max} <$ 1.23 °C
Orange	Non-green profiles north of 73.34°S and $T_{max} <$ 1.13 °C

Table 2
The water mass characteristics of CDW, WW, and meltwater. The water mass characteristics of CDW and WW in potential temperature, salinity and dissolved oxygen are chosen such that the CDW/WW mixing line is the same as in Jacobs et al. (2011).

Characteristics	CDW	WW	MW
Potential temperature (°C)	1.18	−1.8	−90.8
Salinity (psu)	34.7	34.0	0.0
Dissolved Oxygen (ml kg^{-1})	4.18	6.83	28.5
Helium concentration (nmol kg^{-1})	1.85	1.86	25.7
Neon concentration (nmol kg^{-1})	8.03	8.22	89.2

CDW properties (Fig. 7b and c) than the blue and pink groups, but their WW properties are similar to those of the blue group.

Note that we only focus on the profiles from the eastern part of the continental shelf. The three stations in the western submarine glacial trough are not included in this analysis (gray dots in Fig. 8). The Heli-CTD station is also not used because it has a thick WW layer from ~100 m almost to the bottom, and thus is different from all other profiles (Fig. 3).

For comparison, we also color-coded the profiles of 2007 and 2009 (Fig. 8b). Since the color-code is defined by the potential temperature and the meltwater fraction, the location of each group demonstrates the pathway of the intrusion of CDW and the spreading of meltwater on the eastern Amundsen Sea continental shelf (Fig. 8a). The pattern of the color-code in 2010 and 2007–2010 is similar (Fig. 8a and b), suggesting that the feature of the intrusion of CDW and the spreading of meltwater have not changed significantly during this period.

4. Discussion

4.1. The reason for the warmer and colder CDW intrusion

Two submarine glacial troughs (marked E and C in Fig. 1) exist which may preferentially guide CDW onto the shelf towards the PIIS cavity (Walker et al., 2007; Thoma et al., 2008; Schodlok et al., 2012). From the observations in 2010, the presence of CDW with potential density higher than 27.7 is observed on the eastern and western sides of Section 1 (Fig. 2). In Section 2, CDW is also observed but only on the eastern side (Fig. 3). From the locations of the color-coded stations (Fig. 8), warmer CDW (red, 1.23 °C $< T_{\max}$) penetrates via trough E, and colder CDW (pink and orange, T_{max} $<$ 1.23 °C) flows via trough C onto the continental shelf. In this subsection, we focus on the profiles on the continental shelf north of 73.34°S, especially the red and orange

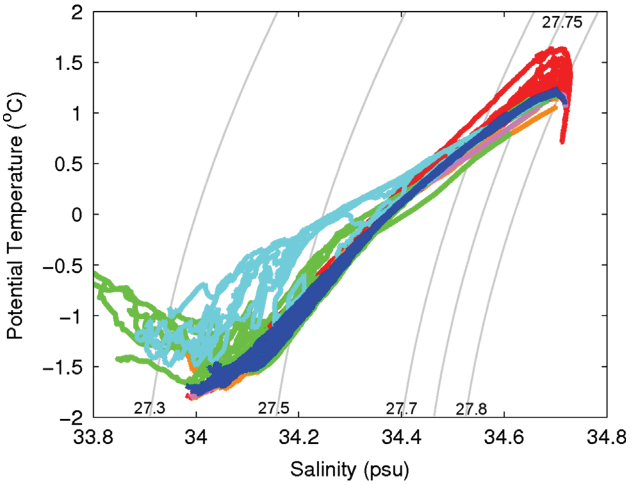

Fig. 6. The θ–S diagram of all CTD stations for 2010 cruise on the eastern Amundsen Sea continental shelf. The definition of the color-code is shown in Table 1 and locations of the color-coded stations are shown in Fig. 8a. All the profiles are plotted from 100 m to the bottom. Surface referenced potential density contours are shown as gray lines.

groups, and investigate why different potential temperatures are observed for the CDW intrusions from troughs E and C.

The vertical profiles of potential temperature and potential density of the red, orange, and blue groups (Fig. 9) show fairly uniform CDW properties below a CDW/WW thermocline (where potential temperature increases rapidly with depth). Since the T_{max} is observed just below the WW/CDW thermocline, we define the intruding CDW layer as the depth range between the T_{max} and the bottom. A thick CDW layer is observed for the red group (100–300 m) in contrast to a thin CDW layer at the bottom for the orange group (Fig. 9). The offshore profiles show that CDW temperature decreases with increasing potential density within the range of 27.76 to the bottom. Thus, the difference in T_{max} can be explained by the different thicknesses of the CDW intrusion; the thick intrusion from trough E contains light and warm (red, $1.23\ ^{\circ}\mathrm{C} < T_{max}$) CDW as well as dense and cold (pink and orange, $T_{max} < 1.23\ ^{\circ}\mathrm{C}$) CDW, while the thin intrusion from trough C contains only dense and cold CDW (Fig. 10). We define the potential density range of the intruding CDW as the density range between the T_{max} and the bottom. Although the variability of the red and orange groups is high, the potential density of the intruding CDW at T_{max} is 27.77 and 27.82 (T_{max} is observed at the bottom) for the red and orange groups, respectively, based on the isopycnally averaged (increment of 0.01) θ–S profiles from the data of 2007, 2009, and 2010 (Fig. 11). This indicates that the intruding CDW of the red group is ~0.35 °C warmer than that of the orange group. Thus, the red, pink, and orange groups can also indicate the thickness of the CDW intrusion. However, it is important to note that the T_{max} can get modified as a result of mixing with surrounding water away from the continental shelf break. For example, pink stations in the middle of the continental shelf are considered to be formed by the mixing of the red and orange groups. In addition, the potential density at the bottom of most orange profiles does not reach 27.82 (Fig. 9). This means that all orange profiles should originally have formed due to the intrusion of CDW at ~27.82, but CDW already gets modified (colder and less saline) due to vertical mixing as it progresses southward (Fig. 12).

The different thicknesses of both CDW intrusions may be related to Ekman transport induced by along-slope currents over the continental slope and shelf break (Wåhlin et al., 2012). The CDW observed at the bottom near the shelf break has a potential density of ~27.81–27.82, i.e. this CDW is withdrawn from a depth of ~700–900 m (consistent with Wåhlin et al., 2012). The thickness and transport of the Ekman layer depends on the topography and depth of the shelf break, which may be the reason for the different characteristics of the red and orange groups (MacCready and Rhines, 1993; Wåhlin et al., 2012). The occurrence of warmer (colder) CDW in trough E (C) may also be related to the cyclonic circulation in the PIT, which cools the CDW entering from trough C, as proposed in Schodlok et al. (2012).

4.2. *The pathway of CDW intrusion on the continental shelf*

Dense CDW, intruding onto the continental shelf and cascading down to the PIT, descends deep and flows in the clockwise direction as a result of the Coriolis force. Thus, possible pathways of the CDW intrusion should follow the bathymetry as indicated by the two gray arrows in Fig. 8a. Schodlok et al. (2012) show, based on numerical modeling, that most of the PIT is dominated by a cyclonic gyre that extends to the north of Section 1 (consistent with possible pathways in Fig. 8a).

Since dense CDW cascades into the PIT, the intruding CDW should be denser than the water mass at the bottom of PIT (blue), where the potential density is ~27.81 (gray line in Fig. 9). The 27.81-contour (Fig. 12) indicates that CDW denser than 27.81 originates from the eastern shelf break, trough E (102°W–108°W), but not from trough C. Thus, the eastern trough plays the most important role for dense CDW flowing into the PIT. Since the blue group has the same T_{max} as the pink group, the formation of 'blue' characteristics could be easily explained if the pink group would dominantly exist on the continental shelf. However, when we focus on the intrusion via trough E, the CDW is mostly in the red group and CDW properties at the density of 27.75–27.81 are largely modified. This modification is obvious as the T_{max} changes from ~1.4 °C to ~1.2 °C (blue) on the way from trough E to PIT (lower left panel of Fig. 12). Since mainly red and orange groups exist on the continental shelf (except for a few pink stations which are considered to be formed by mixing of red and orange groups) and the 27.78-contour (Fig. 8b) shows the intrusion of CDW from both troughs, it is considered that the orange group (from trough C) mixes with the red group (from trough E) modifying and forming the blue group. Several red profiles on the western side of trough E (e.g. two stations surrounded by black squares in lower left box of Fig. 12) show the mixing between the red and orange groups (Fig. 11, red dashed lines). To analyze the contribution of the red and orange groups for forming the blue group, we assume that the averaged red, orange and blue groups are representative and the contribution of each group can be calculated from the distance of each θ–S profile to the blue θ–S profile. The ratio of red to orange contributions to form the blue is calculated to be roughly 1:1.5 below the 27.78-isopycnal (Fig. 11).

Because all the CTD measurements were conducted in austral summer, it cannot be excluded that the intrusion of CDW has a seasonal cycle. Thoma et al. (2008) show that the inflow via trough C is weakest in austral summer. However, the distribution of CDW-layer thickness in their model always shows a thicker CDW layer in trough C than in trough E, which is not consistent with the observations between 2007 and 2010. This may be due to old topographic data, which does not include the eastern submarine glacial trough (trough E). Arneborg et al. (2012) show results from the first mooring observations in trough W (Fig. 1) where they did not find any strong seasonal cycle, which is also not consistent with Thoma et al. (2008). Schodlok et al. (2012), on the other hand, show that the warm CDW only penetrates from trough E, and the intrusion is the strongest in austral summer. Our observed modification of the CDW intrusion from trough E to the PIT and the spatial distribution of cold and warm CDW intrusions from troughs E and C are consistent with their model results (Schodlok et al., 2012, Fig. 3). Thus, our CTD measurements may show the

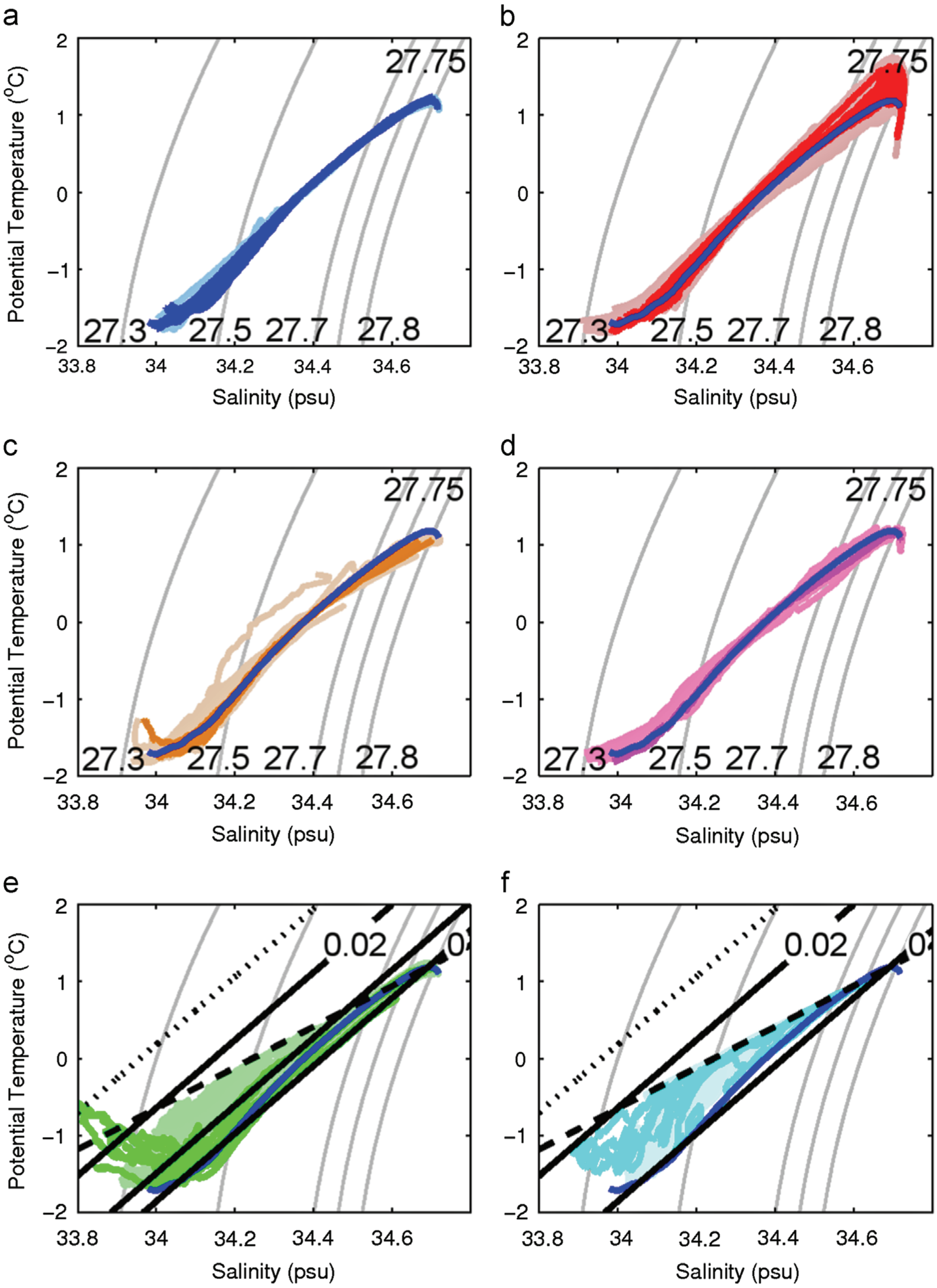

Fig. 7. Color-coded θ–S diagrams with the same profiles shown in Fig. 6. The blue, red, orange, pink, green, and cyan groups are shown separately in (a)–(f), respectively. For all figures, 2010-data are plotted with dark color, and 2007-data and 2009-data are plotted with light color. For (b)–(f), averaged profiles of blue are always shown as reference. In (e) and (f), the thick black lines are meltwater fractions (contour of 0%, 0.6% (only in d), and 2%) and the black dotted contour is the theoretical upper bound of the meltwater fraction. The dashed line indicates the CDW/meltwater mixing trend.

intrusion from trough E at its peak level, but the seasonality of the intrusion requires further investigation.

4.3. *Melting of PIIS*

4.3.1. *Meltwater fraction at the ice shelf front*

We calculate the meltwater fraction (see Appendix A) for the ice front section. From the θ–S diagrams of the green and cyan groups (Fig. 7e and f), the zero meltwater fraction contour connects the characterized WW and CDW properties (Table 2). The deviations from this contour, especially for the cyan group, indicate the inclusion of glacial melt (Fig. 7e and f).

The vertical profiles of the meltwater fraction in θ–S, O_2–S, and O_2–θ spaces from the ice shelf front section (Fig. 13) show strong meltwater signals at the depth of 100–500 m with a somewhat larger meltwater fraction (~1.5%) at the depth of 200–300 m. The meltwater fraction is also calculated from the concentration of dissolved noble gases (neon and helium), which are supersaturated in seawater when air bubbles are released from the ice by basal melting. Due to their low solubility, these supersaturated noble gas signals show the clearest signature of meltwater from meteoric ice (Schlosser, 1986;

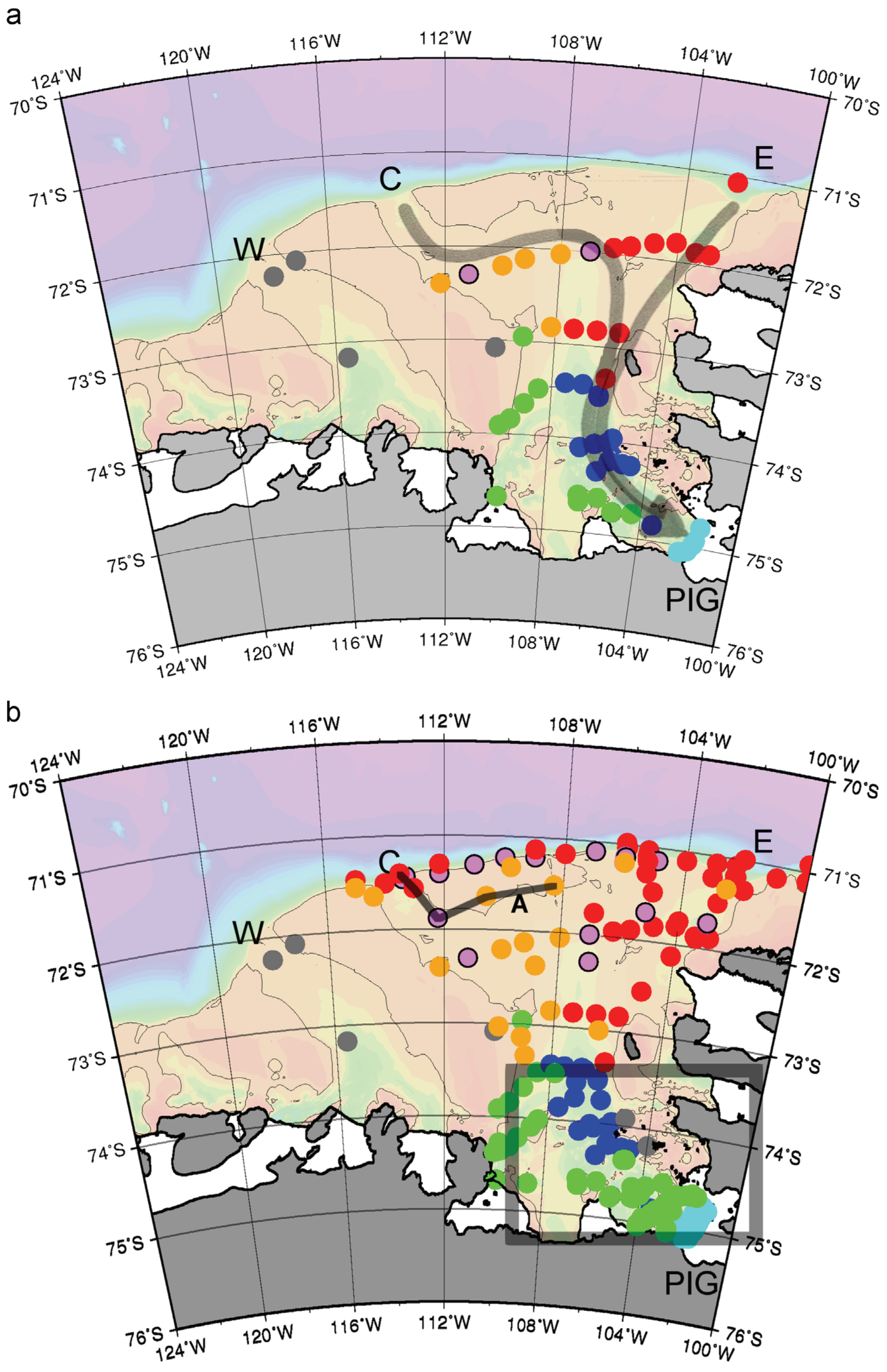

Fig. 8. Locations of the color-coded CTD stations in (a) 2010 and (b) 2007, 2009, and 2010 on the eastern Amundsen Sea continental shelf (all stations on the shelf east of the subsurface ridge extending out from Bear Peninsula are shown). Pink stations are surrounded by black circles. Stations not used for the analysis are shown in gray. The enclosed region indicates the location referred to in Fig. 15. Two stations in 2009 are not used because of a thick WW layer reaching almost to the bottom. The two arrows in (a) show the possible pathway of the CDW intrusion.

Hohmann et al., 2002). We define representative helium and neon concentrations in CDW, WW, and meltwater for CDW following Hohmann et al. (2002), for meltwater following Hohmann et al. (2002) and Huhn et al. (2008), and Huhn et al. (2008) for WW (Table 2). Helium and neon samples are only available at some specific depths because of the limited amount of sample devices having been available on the cruise. The vertical profiles of meltwater fractions (Fig. 13) show that the fractions in θ–S, O_2–S, and O_2–θ spaces are mostly consistent with the meltwater fractions in He–S and Ne–S spaces. The causes for some small disagreements are considered to be due to nonuniform WW properties. It is not possible to fit all the meltwater fractions in θ–S, O_2–S, and O_2–θ spaces to the meltwater fractions obtained from helium and neon, even though the defined water mass characteristics are adjusted (not shown). It is

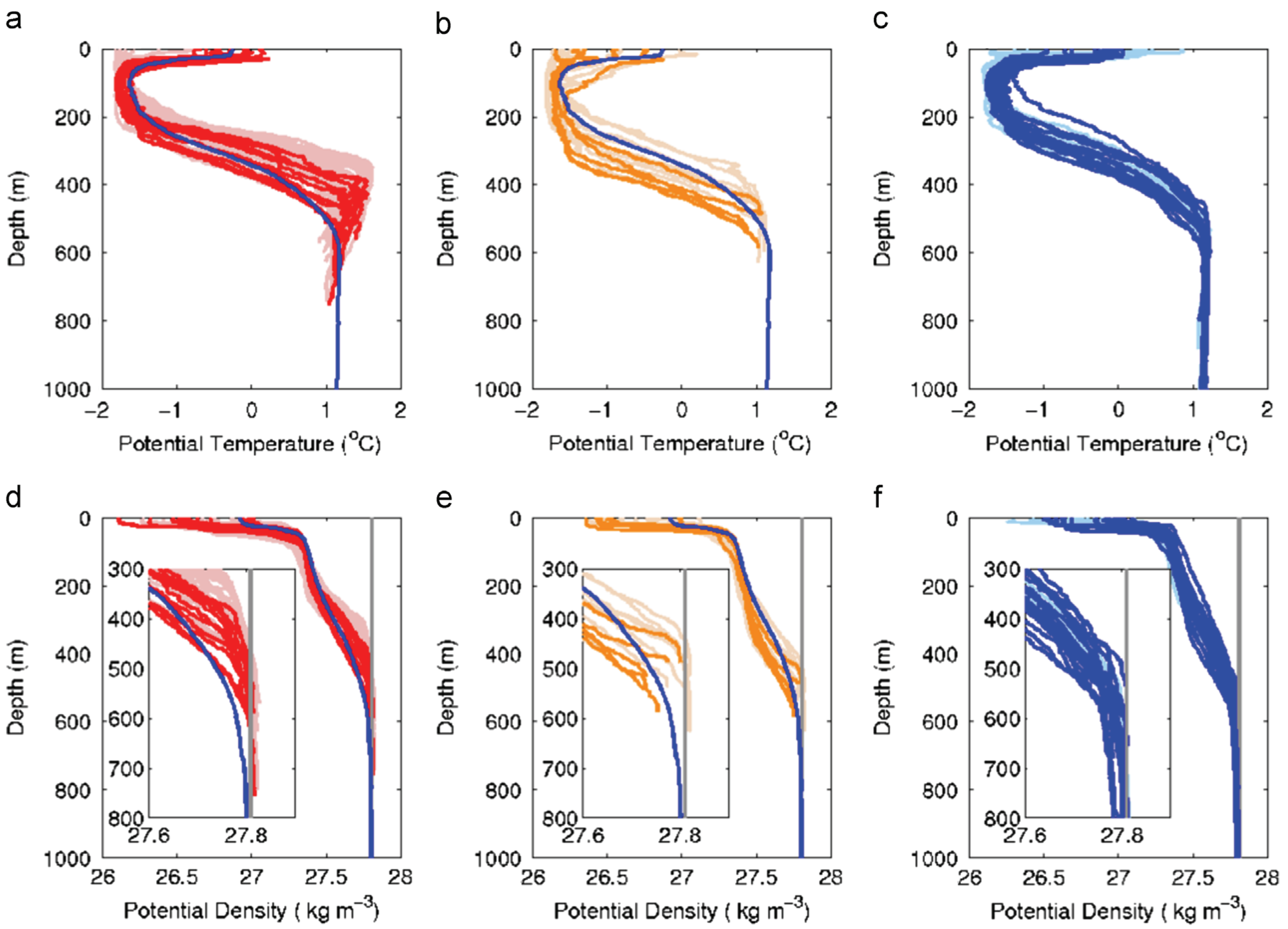

Fig. 9. Vertical profiles of potential temperature (a–c) and potential density (d–f) of the red, orange, and blue groups from 2010-(dark color), 2007-, and 2009-data (light color). In a, b, d, and e the blue lines are the depth-averaged profile of the blue group. In (d–f), the gray lines mark the 27.81-isopycnal and the insets magnify the bottom part of the profiles.

important to note that the meltwater fractions derived in He–S and Ne–S spaces are as low as 0.3% at 800 m (station 153), which will be discussed below. Since the detection limits of the meltwater fraction for helium and neon are in the order of 0.1%, these signals are clearly above the detection limit.

The calculation of the meltwater fraction is invalid for the surface mixed layer, because equilibration with the atmosphere raises the dissolved oxygen concentration toward saturation, and other sources of freshwater reduce the salinity (Jenkins, 1999; Jenkins and Jacobs, 2008). Thus, the meltwater fractions derived from θ–S, O_2–S, and O_2–θ spaces show larger disagreement at depths shallower than ~150 m (Fig. 13). In the following analysis, the average of these three meltwater fractions is calculated, while the meltwater fractions for depth <150 m, where the standard deviation of these three meltwater fractions is larger than half of the theoretical upper bound (Appendix A) is excluded from the analysis.

4.3.2. Basal melt rate of the PIIS

We calculate the transport of meltwater into and out of the cavity beneath the PIIS by analyzing the CTD ice front section (Fig. 5). Since direct observations of ocean currents do not exist, we estimate the velocity assuming hydrostatic and geostrophic balance. In estimating the full-depth ocean current, however, it is difficult to define the barotropic reference velocity (Jenkins and Jacobs, 2008). Thus, we first provide a simple estimate of the melt rate using geostrophic balance and conservation of salt between inflow and outflow.

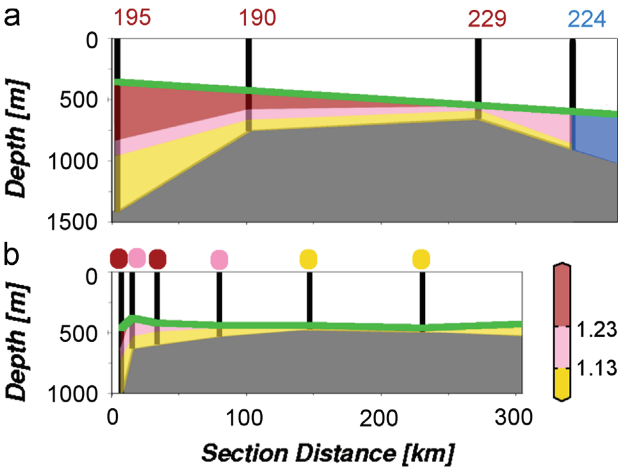

Fig. 10. Vertical sections of potential temperature of (a) Section 1 (but from stations 195–224) and (b) Section Appendix A from 2009 shown in Fig. 8. Green lines show T_{max} and, shading is drawn for only the part deeper than T_{max}, which corresponds to the intruding CDW layer. Shading colors are defined according to the red, pink, and orange groups. The vertical black lines mark the location of CTD profiles. For Section 1, color-coded station numbers are shown. For Section Appendix A, color-coded circles are shown. Bottom topography is drawn based on the bottom depth of each profile. For (a), south of station 224 is shaded blue to indicate that there stations are defined as the blue group. (For interpretation of the references to color in this figure legend, the reader is referred to the web version of this article.)

Our first estimate of the melt rate is based on the assumption that the level of no motion is at the depth of 500 m following Jacobs et al. (2011) and CDW flows into the cavity below that level. The mean geostrophic velocity below 500 m is 1.89 cm s^{-1}, resulting in an inflow of 228 mSv (1 mSv$=10^3$ m^3 s^{-1}). In addition, salt should be conserved and $(V_{in}+V_{melt})S_{out}=V_{in}S_{in}$ should be satisfied, where V_{in} and V_{melt} are the volume transport of inflow and meltwater, respectively and S_{in} and S_{out} are the salinity of the inflow and outflow, respectively. The average salinity for the inflow and outflow are calculated to be 34.59 and 34.28 (average outflow salinity is calculated between 200 and 500 m depth). Thus, V_{melt} is calculated to be 2.05 mSv, which is equivalent to an ice loss of 72.3 km^3 yr^{-1}, or a mean melt rate of 30 m yr^{-1}, assuming a cavity size of 70 × 35 km^2. (Note that the cavity size might have increased from 2009 to 2010 to ~74 × 35 km^2, causing our result to be overestimated by ~5%.)

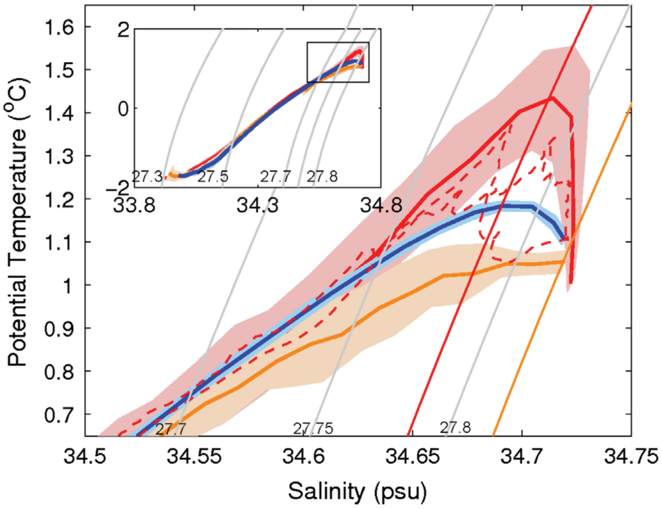

Fig. 11. Isopycnally averaged (increment of 0.01) θ–S profiles of the red, orange, and blue groups from the data of 2007, 2009, and 2010 with 1σ shaded in light color. The inset in upper left panel denotes the enlarged portion. The averaged profiles shown by the red (orange) line are calculated using all the CTD profiles of the stations marked in red (orange) with the bottom shallower than 800 m (Fig. 7b). The averaged profiles shown by the blue line are calculated using all the CTD profiles of the stations marked in blue with no bottom depth limit. In the enlarged portion, the contours of 27.786 (red) and 27.817 (orange) are additionally shown. Two θ–S profiles of the red profile (surrounded by black square in lower left panel of Fig. 12) are shown (red dashed) to illustrate the isopycnal mixing between the red and orange groups.

Although a somewhat realistic melt rate was obtained with this simple approach, we employ the more sophisticated method by Wunsch (1978), Jenkins and Jacobs (2008), and Jacobs et al. (2011) (see Appendix B). Following Jacobs et al. (2011), we assume that the level of no motion is set to the depth where the meltwater fraction is 0.5% (yellow dashed line in Fig. 14) and the surface layer, where the meltwater fractions show large disagreements, is excluded from the calculation (region surrounded by black dashed line in Fig. 14). In this calculation, half of the theoretical upper bound (Appendix A) is used to investigate the accuracy of the meltwater fraction, while a quarter of theoretical upper bound was used in Jacobs et al. (2011) to obtain a more realistic circulation.

The adjusted geostrophic velocity profile along the PIIS front (Fig. 14) shows inflow mostly in the north and outflow mostly in the south, indicating a clockwise sub-ice shelf circulation. Our estimated inflow, outflow, and difference are 602 mSv, 604 mSv and 1.98 mSv, respectively, which is equivalent to a basal melting of 70 km^3 yr^{-1} of ice. Jacobs et al. (2011) calculated for inflow, outflow, and difference 400 mSv, 402 mSv, and 2.26 mSv (80 km^3 yr^{-1} of ice) for 2009 and 219 mSv, 220 mSv, and 1.49 mSv (53 km^3 yr^{-1} of ice) for 1994. If all the meltwater transported out of the cavity originated from the central region of the ice shelf, whose area is 70 × 35 km^2, the basal melt rate would be 29 m yr^{-1} in 2010, 33 m yr^{-1} in 2009, and 22 m yr^{-1} in 1994 (Jacobs et al., 2011).

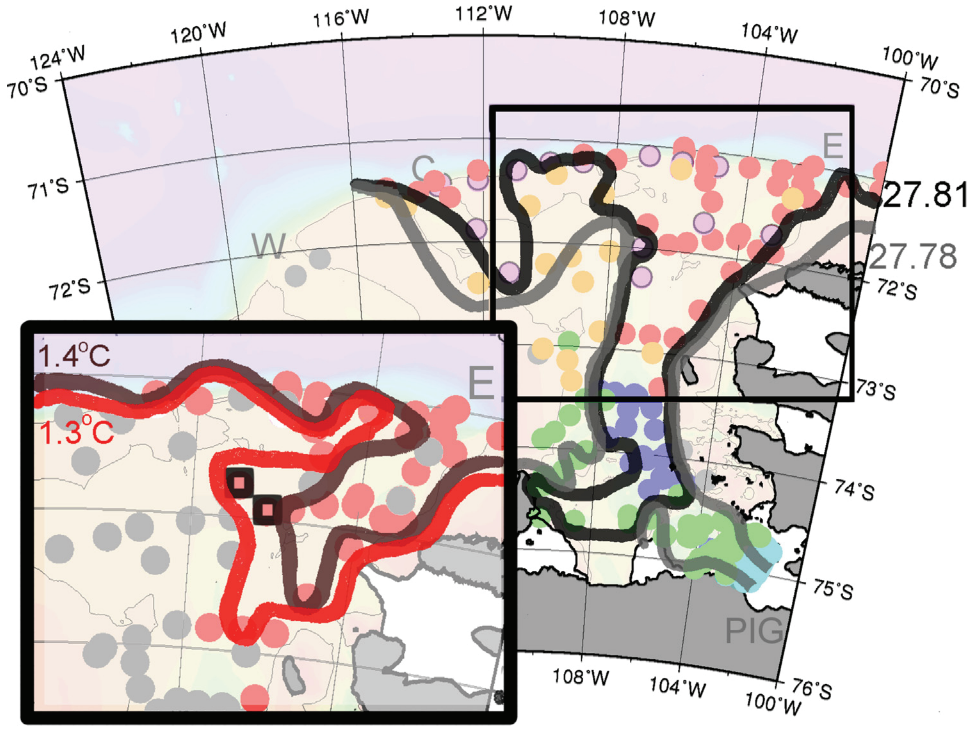

Fig. 12. Same as Fig. 8 but with bottom potential density contours. The enclosed region denotes the enlarged portion. Here, the maximum potential temperature (T_{max}) contours are shown only for red group. Other groups are shown in gray. Two red stations surrounded in the enlarged portion are referred to in Fig. 11. (For interpretation of the references to color in this figure legend, the reader is referred to the web version of this article.)

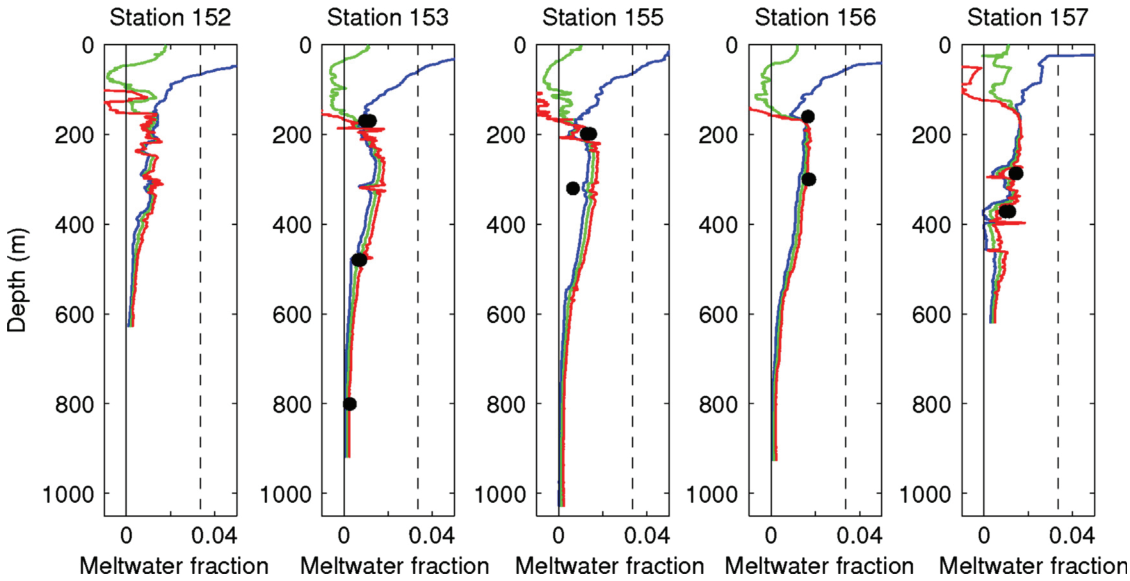

Fig. 13. Vertical profiles of meltwater fraction of Section 3. Continuous profiles are the meltwater fractions from θ–S (blue), O_2–S (green), and O_2–θ (red) spaces. The discrete values at bottle depths (black dots) are the meltwater fractions derived from He–S and Ne–S space. The vertical dashed line indicates the theoretical upper bound of the meltwater fraction. (For interpretation of the references to color in this figure legend, the reader is referred to the web version of this article.)

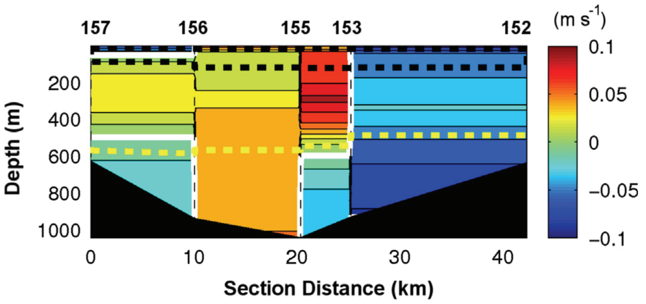

Fig. 14. Adjusted geostrophic velocity along the PIIS front looking out of the cavity (positive denotes for the outflow). CTD station numbers are shown on top. Zero velocity contour is indicated by the white line. The domain surrounded by the black dashed lines is the excluded surface layer. The yellow dashed line is the depth with 0.5% meltwater fraction where the level of no motion is initially assumed before adding the barotropic reference velocity. (For interpretation of the references to color in this figure legend, the reader is referred to the web version of this article.)

The melt rate in 2010 is similar to that of 2009 (~30 m yr^{-1}), but both are significantly higher than the rate of 1994. However, transport in and out of the PIIS cavity increased from 1994 to 2010 with a 50% rise from 2009 to 2010. From 1994 to 2009, large changes in the shape of the cavity might have occurred causing the significant increase in the strength of sub-ice shelf circulation and melt rate (Jacobs et al., 2011). However, since ice shelf geometry changes with a time scale of decades (Jenkins et al., 2010), it is unlikely that an altered cavity shape increased the sub-ice shelf circulation from 2009 to 2010. The enhanced sub-ice shelf circulation in 2010 may be the result of capturing the recirculation of CDW, caused by short term variability of the clockwise eddy located in front of PIIS (Mankoff et al., 2012; Jacobs et al., 2012). Because average inflow and outflow potential temperature are 0.5 °C and 0.0 °C, respectively, in 2009 (calculated from Jacobs et al., 2012) and 0.5 °C and 0.1 °C in 2010, more of the CDW flowed in and out without melting the ice shelf. However, it might be erroneous to assume that our CTD stations effectively closed off the cavity. Because the southernmost station is located too far south, our measurements could not capture the primary meltwater outflow, which should be to the south of Section 4. To test the sensitivity of our result, we substitute temperature, salinity, and oxygen of station 157 by those of station 16 from 2009 (Jacobs et al., 2011, Figs. 1 and 2) but keeping the geostrophically calculated velocity. This lead to a similar melt rate with an inflow and outflow closer to the result of Jacobs et al. (2012), also indicating that the strong inflow and outflow in 2010 may be an artifact of sparse CTD observations.

4.4. *The pathway of meltwater*

The location of the green group shows that the meltwater flows along the bathymetry towards the west (Fig. 8). This flow may be considered as a current supplied by the constant outflow of buoyant meltwater from the PIIS and other cavities. On the isopycnal of 27.5–27.7, meltwater fractions of about 0.4% are observed in the blue group (Fig. 7a, e, and f). Since the meltwater fractions are fairly small, we investigate whether these values are meaningful. In general, when two water masses mix, the θ–S diagram shows a straight line between these two water masses. The blue θ–S profiles, however, curve toward a higher meltwater fraction at the potential density of 27.5–27.7, which cannot be formed as a mixing of CDW and WW only. In addition, the helium and neon concentrations at the PIIS front at the depth of 800 m also show a meltwater signal (~0.3%, clearly above the detection limit), indicating the addition of meltwater to the CDW layer. Thus, the meltwater signal observed at the isopycnal of 27.7 should be meaningful, possibly caused by the recirculation of meltwater in PIT.

4.5. *Comparison with previous observations*

At the locations of the color-coded CTD stations (Fig. 8b), the characteristics of the intruding CDW remain similar during the years 2007, 2009, and 2010. We thus compare the blue profiles (PIT) of the three years with five CTD profiles from 2000 in PIT (black dots within black box in Fig. 15). Although Jacobs et al. (2012) stated that the temporal variability of CDW intrusion is large, the temporal variability of the θ–S profiles in PIT (blue) is extremely small compared to the red and orange group on the outer shelf. Thus, the θ–S profile in PIT can be used for detecting changes in the CDW intrusion.

Compared to the 2000-data, the θ–S profiles of 2007–2010 (Fig. 15) are warmer and saltier. The main difference, however, is

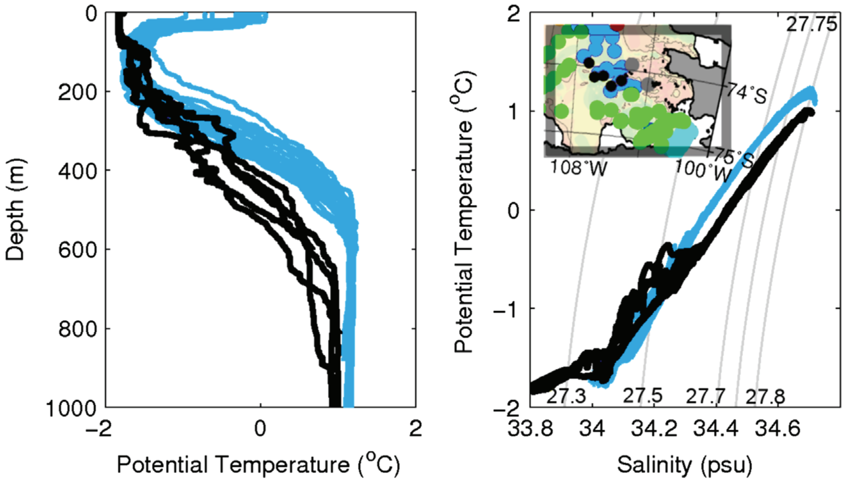

Fig. 15. Comparison of vertical profiles (left) and θ–S diagram (right) of all the blue stations (light blue, 2007–2010) and five stations from 2000 (black) for the gray marked region in Fig. 8. The locations of the stations in 2000 (black dots) are shown in the upper left panel of the right figure. (For interpretation of the references to color in this figure legend, the reader is referred to the web version of this article.)

the thicker CDW layer, while the thickness of the WW layer (potential temperature ~−1.8 °C) remained similar. The potential temperature of the CDW increased by ~ 0.15 °C and the gradient of the WW/CDW thermocline became steeper in 2009–2010, but the density of the CDW remained almost the same. Thus, a thicker CDW layer with higher temperature was able to penetrate onto the continental shelf in 2007–2010 compared to 2000.

5. Summary

After the discovery in 1994 that PIIS is rapidly melting due to the presence of CDW on the Amundsen Sea continental shelf (Jacobs et al., 1996), several observations were conducted. To understand the melting of PIIS, we studied the CDW flow onto the Amundsen Sea continental shelf, basal melting of PIIS, and spreading of the resulting meltwater. In this study, we mainly analyzed the data from observations in 2010 done by the German expedition ANTXXVI/3.

CDW intrudes onto the eastern Amundsen Sea continental shelf through the eastern and central submarine glacial troughs (Fig. 1). The potential temperature of the CDW intrusion is controlled by the thickness of the CDW layer. The thick intrusion via trough E contains light and warm CDW (warmer than 1.23 °C) as well as dense and cold CDW (colder than 1.23 °C), while the thin intrusion via trough C only contains dense and cold CDW (Figs. 8 and 10).

To fill PIT with CDW, the potential density of the intruding CDW has to be denser than the water mass at the bottom of PIT (blue). The course of the 27.81-isopycnal of bottom potential density shows that the CDW intrusion denser than 27.81 reaches PIT only from trough E (red). However, this CDW is largely modified and the T_{max} changes from ~1.4 °C to ~1.2 °C on the way from trough E to PIT (lower left panel of Fig. 12). This modification occurs as a result of mixing with the orange group (CDW typically seen in the vicinity of trough C). The mixing ratio of the red and orange groups is calculated to be about 1:1.5 below the 27.78-isopycnal (Fig. 11).

The vertical profiles of meltwater fractions at the PIIS front show the outflow of meltwater at the depth of 100–500 m (Fig. 13), consistent with the meltwater fractions obtained in He–S and Ne–S spaces. The estimated melt rate in 2010 ranges from 29 to 30 m yr^{-1} depending on the method applied. This is significantly larger than the melt rate in 1994 (~22 m yr^{-1}) and similar to the melt rate in 2009 (Jacobs et al., 2011). However, the calculated inflow and outflow shows a rather suspicious 50% increase from 2009 to 2010. This is either caused by capturing short term variability in Pine Island Bay or the assumption that our CTD section effectively closes off the cavity.

The meltwater spreads along the bathymetry towards the west (green group in Fig. 8). From the meltwater fraction on the isopycnals 27.5–27.7 and the helium and neon concentrations at the ice shelf front at the depth of 800 m, the meltwater signal of the intruding CDW is calculated to be 0.3–0.4%, indicating that some of the meltwater mixes with CDW.

The characteristics of the intruding CDW remain similar from 2007 to 2010 (Fig. 8b). The main difference is that the CDW layer became thicker and warmer, containing warm and light CDW as well as cold and dense CDW (Fig. 15). Such potential temperature increase in the CDW of PIT is not considered to be the cause for increased melting of PIIS, which seems to be the consequence of a change in cavity shape as reported by Jenkins et al. (2010) and Jacobs et al. (2011).

Despite numerous observations and modeling studies on PIIS, we still do not fully understand how PIIS melting is controlled and how it will respond to climate change. Understanding PIIS melting is important, because CDW is also melting some other glaciers in West Antarctica in a similar way. Numerical modeling also shows that intrusion of CDW can occur on the southern Weddell Sea continental shelf, resulting in rapid basal melting in the near future (Hellmer et al., 2012). Thus, a detailed understanding of CDW intrusion onto the continental shelf and ice sheet-ocean interaction is crucial for predicting the consequences of climate change in the Southern Ocean.

Acknowledgments

We thank Adrian Jenkins, Andreas Wisotzki, Pierre Dutrieux, Oliver Huhn, and Stanley S. Jacobs for their useful comments and suggestions. We also thank Adrian Jenkins for providing his scripts for the meltwater fraction and melt rate calculation. Noble gas measurements are conducted by Jürgen Sültenfu and Oliver Huhn (University of Bremen, Institute of Environmental Physics). Insightful comments from two anonymous reviewers and John Klinck were very helpful for improving the manuscript. We also thank the oceanographic team on the research ice breaker Polarstern during ANTXXVI/3. Some of the figures are produced with Ocean Data View (Schlitzer, 2004).

Appendix A. Meltwater fraction calculations

The meltwater fraction is calculated simply as the mixture of three water masses (Jenkins, 1999; Jenkins and Jacobs, 2008; Jacobs et al., 2011) as shown in the following equations:

$$\chi^1_{mix} = A\chi^1_{CDW} + B\chi^1_{MW} + C\chi^1_{WW}, \tag{A.1}$$

$$\chi^2_{mix} = A\chi^2_{CDW} + B\chi^2_{MW} + C\chi^2_{WW}, \tag{A.2}$$

$$A + B + C = 1, \tag{A.3}$$

where A, B, and C are fractions of CDW, meltwater, and WW, respectively, and χ is a tracer that is conserved during mixing. Two tracers χ^1 and χ^2 are chosen from the available parameter sets of potential temperature, salinity, dissolved oxygen, and concentrations of helium and neon.

The subscripts of χ indicate defined water mass characteristics for CDW, WW, and meltwater following Jenkins (1999), Jenkins and Jacobs (2008), and Jacobs et al. (2011), summarized in Table 2. By solving for B, the meltwater fraction can be obtained as

$$B = \frac{(\chi^1_{mix} - \chi^1_{CDW}) - (\chi^2_{mix} - \chi^2_{CDW})\left(\frac{\chi^1_{WW} - \chi^1_{CDW}}{\chi^2_{WW} - \chi^2_{CDW}}\right)}{(\chi^1_{melt} - \chi^1_{CDW}) - (\chi^2_{melt} - \chi^2_{CDW})\left(\frac{\chi^1_{WW} - \chi^1_{CDW}}{\chi^2_{WW} - \chi^2_{CDW}}\right)}. \tag{A.4}$$

The theoretical upper bound is the maximum meltwater fraction ($C=0$ in Eq. (A.1)) which occurs when the potential temperature of CDW (χ^1_{mix}) is reduced to the freezing point and no further melting can occur (the intersection point of freezing point and CDW/meltwater mixing line in Fig. 7, Jenkins and Jacobs, 2008).

Appendix B. Transport calculations

We use the same techniques used near George VI Ice Shelf (Jenkins and Jacobs, 2008) to estimate the basal melt rate, which is based on the classical inverse method (Wunsch, 1978). We assume that our CTD sections effectively close off the cavity, and the total mass transport must satisfy

$$\sum_{j=1}^{n} (M_{out} - M_{in})_j = M_{melt}, \tag{B.1}$$

where M_{in}, M_{out} and M_{melt} are the mass transport of inflow, outflow and meltwater, respectively and n is the number of vertical velocity profiles between n+1 CTD stations. Assuming that cavity properties are in steady state, a similar equation must be satisfied for the transport of each tracer χ across the section shown as

$$\sum_{j=1}^{n} \{(M\chi)_{out} - (M\chi)_{in}\}_j = M_{melt}\chi_{MW}. \tag{B.2}$$

Combining the conservations of total mass transport and tracer transport, Eqs. (B.1) and (B.2) can be reduced to

$$\sum_{j=1}^{n} \frac{1}{g} \int_{P_{bot}}^{P_{top}} (v_j^{adj} + \overline{v}(p))[\overline{\chi}(p) - \chi_{MW}]\Delta x(p)\, dp = 0, \tag{B.3}$$

where overbars indicate averages over the width Δx between stations, g is the acceleration due to gravity, p is the pressure, v_j^{adj} is the barotropic reference velocity and $\overline{v}(p)$ is the velocity obtained from the geostrophic balance. In our calculation, n equals to four with four unknown barotropic reference velocities, while we have only three equations for potential temperature, salinity, and dissolved oxygen. Since, this problem has many possible solutions, we choose the one that minimizes the sum of the squares of the barotropic reference velocities.

References

Arneborg, L., Wåhlin, A., Björk, G., Liljebladh, B., Orsi, A., 2012. Persistent inflow of warm water onto the central Amundsen shelf. Nat. Geosci. 5, 876–880.

Bamber, J.L., Riva, R.E.M., Vermeersen, B.L.A., LeBrocq, A.M., 2009. Reassessment of the potential sea-level rise from a collapse of the West Antarctic Ice Sheet. Science 324, 901–903.

Gohl, K., 2010. The expedition of the Research Vessel Polarstern to the Amundsen Sea, Antarctica, in 2010 (ANT-XXIV/3). Rep. Polar Mar. Res. 617, 173.

Heimbach, P., Losch, M., 2012. Adjoint sensitivities of sub-ice shelf melt rates to ocean circulation under Pine Island Ice Shelf, West Antarctica. Ann. Glaciol. 53, 59–69.

Hellmer, H.H., Jacobs, S.S., Jenkins, A., 1998. Oceanic erosion of a floating Antarctic glacier in the Amundsen Sea. In: Jacobs, S., Weiss, R. (Eds.), Ocean, Ice, and Atmosphere: Interactions at the Antarctic continental margin. Antarctic Research Series, AGU, Washington DC, USA 75, pp. 319–339.

Hellmer, H.H., Kauker, F., Timmermann, R., Determann, J., Rae, J., 2012. Twenty-first-century warming of a large Antarctic ice-shelf cavity by a redirected coastal current. Nature 485, 225–228.

Hohmann, R., Schlosser, P., Jacobs, S., Ludin, A., Weppernig, R., 2002. Excess helium and neon in the southeast Pacific: tracers for glacial meltwater. J. Geophys. Res. 107, 3198.

Huhn, O., Hellmer, H.H., Rhein, M., Rodehacke, C., Roether, W., Schodlok, M.P., Schröder, M., 2008. Evidence of deep-and bottom-water formation in the western Weddell Sea. Deep Sea Res. Part II: Top. Stud. Oceanogr. 55, 1098–1116.

Jacobs, S., Jenkins, A., Hellmer, H., Giulivi, C., Nitsche, F., Huber, B., Guerrero, R., 2012. The Amundsen Sea and the Antarctic Ice Sheet. Oceanography 25, 154–163.

Jacobs, S.S., Giulivi, C.F., Mele, P.A., 2002. Freshening of the Ross Sea during the late 20th century. Science 297, 386.

Jacobs, S.S., Hellmer, H.H., Jenkins, A., 1996. Antarctic ice sheet melting in the Southeast Pacific. Geophys. Res. Lett. 23, 957–960.

Jacobs, S.S., Jenkins, A., Giulivi, C.F., Dutrieux, P., 2011. Stronger ocean circulation and increased melting under Pine Island Glacier ice shelf. Nat. Geosci. 4, 519–523.

Jakobsson, M., Anderson, J.B., Nitsche, F.O., Dowdeswell, J.A., Gyllencreutz, R., Kirchner, N., Mohammad, R., O'Regan, M., Alley, R.B., Anandakrishnan, S., et al., 2011. Geological record of ice shelf break-up and grounding line retreat, Pine Island Bay, West Antarctica. Geology 39, 691–694.

Jenkins, A., 1999. The impact of melting ice on ocean waters. J. Phys. Oceanogr. 29, 2370–2381.

Jenkins, A., Dutrieux, P., Jacobs, S.S., McPhail, S.D., Perrett, J.R., Webb, A.T., White, D., 2010. Observations beneath Pine Island Glacier in West Antarctica and implications for its retreat. Nat. Geosci. 3, 468–472.

Jenkins, A., Jacobs, S., 2008. Circulation and melting beneath George VI ice shelf, Antarctica. J. Geophys. Res. 113, C04013.

Joughin, I., Alley, R.B., 2011. Stability of the West Antarctic ice sheet in a warming world. Nat. Geosci. 4, 506–513.

MacCready, P., Rhines, P., 1993. Slippery bottom boundary layers on a slope. J. Phys. Oceanogr. 23, 5–22.

Mankoff, K., Jacobs, S., Tulaczyk, S., Stammerjohn, S., 2012. The role of Pine Island Glacier ice shelf basal channels in deep-water upwelling, polynyas and ocean circulation in Pine Island Bay, Antarctica. Ann. Glaciol. 53, 123.

Nitsche, F.O., Jacobs, S.S., Larter, R.D., Gohl, K., 2007. Bathymetry of the Amundsen Sea continental shelf: implications for geology, oceanography, and glaciology. Geochem. Geophys. Geosyst. 8, Q10009.

Payne, A.J., Holland, P.R., Shepherd, A.P., Rutt, I.C., Jenkins, A., Joughin, I., 2007. Numerical modeling of ocean–ice interactions under Pine Island Bay's ice shelf. J. Geophys. Res. 112, C10019.

Pritchard, H., Ligtenberg, S., Fricker, H., Vaughan, D., Van den Broeke, M., Padman, L., 2012. Antarctic ice-sheet loss driven by basal melting of ice shelves. Nature 484, 502–505.

Rignot, E., Bamber, J.L., den Broeke, M.R.V., Davis, C., Li, Y., de Berg, W.J.V., Meijgaard, E.V., 2008. Recent Antarctic ice mass loss from radar interferometry and regional climate modelling. Nat. Geosci. 1, 106–110.

Rignot, E., Mouginot, J., Scheuchl, B., 2011. Ice flow of the Antarctic ice sheet. Science 333, 1427–1430.

Rignot, E., Vaughan, D.G., Schmeltz, M., Dupont, T., MacAyeal, D., 2002. Acceleration of Pine island and Thwaites Glaciers, West Antarctica. Ann. Glaciol. 34, 189–194.

Rintoul, S.R., 2007. Rapid freshening of Antarctic Bottom Water formed in the Indian and Pacific oceans. Geophys. Res. Lett. 34, L06606.

Schlitzer, R., 2004. Ocean Data View. Alfred Wegener Institute for Polar and Marine Research, Bermerhaven, Germany.

Schlosser, P., 1986. Helium: a new tracer in Antarctic oceanography. Nature 321, 233–235.

Schodlok, M.P., Menemenlis, D., Rignot, E., Studinger, M., 2012. Sensitivity of the ice shelf ocean system to the sub-ice shelf cavity shape measured by NASA IceBridge in Pine Island Glacier, West Antarctica. Ann. Glaciol. 53, 156–162.

Shepherd, A., Ivins, E., Geruo, A., Barletta, V., Bentley, M., Bettadpur, S., Briggs, K., Bromwich, D., Forsberg, R., Galin, N., et al., 2012. A reconciled estimate of ice-sheet mass balance. Science 338, 1183–1189.

Shepherd, A., Wingham, D.J., Mansley, J.A.D., Corr, H.F.J., 2001. Inland thinning of Pine Island Glacier, West Antarctica. Science 291, 862.

Sültenfu, J., Roether, W., Rhein, M., 2009. The Bremen mass spectrometric facility for the measurement of helium isotopes, neon, and tritium in water. Isot. Environ. Health Stud. 45, 83–95.

Thoma, M., Jenkins, A., Holland, D., Jacobs, S., 2008. Modelling circumpolar deep water intrusions on the Amundsen Sea continental shelf, Antarctica. Geophys. Res. Lett. 35, 555.

Timmermann, R., Brocq, A.L., Deen, T., Domack, E., Dutrieux, P., Galton-Fenzi, B., Hellmer, H., Humbert, A., Jansen, D., Jenkins, A., et al., 2010. A consistent data set of Antarctic ice sheet topography, cavity geometry, and global bathymetry. Earth Syst. Sci. Data 2, 261–273.

Vaughan, D.G., Corr, H.F.J., Ferraccioli, F., Frearson, N., O'Hare, A., Mach, D., Holt, J.W., Blankenship, D.D., Morse, D.L., Young, D.A., 2006. New boundary conditions for the West Antarctic ice sheet: subglacial topography beneath Pine Island Glacier. Geophys. Res. Lett. 33, 555.

Wåhlin, A.K., Muench, R.D., Arneborg, L., Björk, G., Ha, H.K., Lee, S.H., Alsén, H., 2012. Some implications of Ekman layer dynamics for cross shelf exchange in the Amundsen Sea. J. Phys. Oceanogr. 42, 1461–1474.

Walker, D.P., Brandon, M.A., Jenkins, A., Allen, J.T., Dowdeswell, J.A., Evans, J., 2007. Oceanic heat transport onto the Amundsen Sea shelf through a submarine glacial trough. Geophys. Res. Lett. 34, 1–4.

Wingham, D.J., Wallis, D.W., Shepherd, A., 2009. Spatial and temporal evolution of Pine Island Glacier thinning, 1995–2006. Geophys. Res. Lett. 36, L17501.

Wunsch, C., 1978. The North Atlantic general circulation west of 50°W determined by inverse methods. Rev. Geophys. 16, 583–620.

4

On the difficulty of modeling Circumpolar Deep Water intrusions onto the Amundsen Sea continental shelf

Yoshihiro Nakayama, Ralph Timmermann, Michael Schröder, and Hartmut H. Hellmer

Alfred Wegener Institute, Helmholtz Centre for Polar and Marine Research
in Bremerhaven, Germany

published in Journal of Ocean Modeling, 84 (2014), 26-34

Y. Nakayama conducted all the model experiments. Y. Nakayama wrote all the text of the paper and prepared all the figures. All authors participated in the discussion of model results and in revising the paper.

Ocean Modelling 84 (2014) 26–34

Contents lists available at ScienceDirect

Ocean Modelling

journal homepage: www.elsevier.com/locate/ocemod

On the difficulty of modeling Circumpolar Deep Water intrusions onto the Amundsen Sea continental shelf

Y. Nakayama*, R. Timmermann, M. Schröder, H.H. Hellmer

Alfred Wegener Institute, Bussestrasse 24, D-27570 Bremerhaven, Germany

ARTICLE INFO

Article history:
Received 22 May 2014
Received in revised form 17 September 2014
Accepted 21 September 2014
Available online 30 September 2014

Keywords:
Finite Element Sea ice–ice shelf-Ocean Model
Amundsen Sea
Circumpolar Deep Water
Ice shelf basal melting

ABSTRACT

In the Amundsen Sea, warm Circumpolar Deep Water (CDW) intrudes onto the continental shelf and flows into the ice shelf cavities of the West Antarctic Ice Sheet, resulting in high basal melt rates. However, none of the high resolution global models resolving all the small ice shelves around Antarctica can reproduce a realistic CDW flow onto the Amundsen Sea continental shelf, and previous studies show simulated bottom potential temperature at the Pine Island Ice Shelf front of about −1.8 °C. In this study, using the Finite-Element Sea ice–ice shelf-Ocean Model (FESOM), we reproduce warm CDW intrusions onto the Amundsen Sea continental shelf and realistic melt rates of the ice shelves in West Antarctica. To investigate the importance of horizontal resolution, forcing, horizontal diffusivity, and the effect of grounded icebergs, eight sensitivity experiments are conducted. To simulate the CDW intrusion realistically, a horizontal resolution of about 5 km or smaller is required. The choice of forcing is also important and the cold bias in the NCEP/NCAR reanalysis over the eastern Amundsen Sea prevents warm CDW from intruding onto the continental shelf. On the other hand, the CDW intrusion is not highly sensitive to the strength of horizontal diffusion. The effect of grounded icebergs located off Bear Peninsula is minor, but may act as a buffer to an anomalously cold year.

1. Introduction

Surrounding Antarctica, cold and dense water is formed due to intense sea-ice formation in coastal polynyas (e.g. Haid and Timmermann, 2013). This water spreads over the bottom of the continental shelf, in some cases interacts with ice shelves, descends the continental slope, and contributes to the Antarctic Bottom Water (AABW). The AABW is mainly formed in the Weddell and Ross Seas and off Adélie land (Orsi et al., 1999). Since the AABW formation is one of the drivers of the global thermohaline circulation, transporting heat from the tropics to higher latitudes (Schmitz, 1995), the understanding of AABW formation is important for assessing the global climate.

In contrast to other continental shelf regions surrounding Antarctica, warm Circumpolar Deep Water (CDW) can be found over the continental shelves of the Amundsen and Bellingshausen Seas (e.g. Jacobs et al., 1996, 2011, 2013; Moffat et al., 2009; Jenkins et al., 2010; Martinson and McKee, 2012; Wåhlin et al., 2013; Walker et al., 2013). This warm water intrudes onto the continental shelf through submarine glacial troughs and flows into the ice shelf cavities of the West Antarctic Ice sheet (WAIS) resulting in high basal melt rates (e.g. Jacobs et al., 1996, 2011, 2013; Jenkins and Jacobs, 2008; Jenkins et al., 2010). For instance, Pine Island Ice Shelf (PIIS) and Thwaites Glacier (TG) together are melting rapidly, draining ∼4% of the entire Antarctic ice sheet (e.g. Wingham et al., 2009; Joughin and Alley, 2011; Shepherd et al., 2012; Rignot et al., 2013).

Melting of ice shelves attached to the WAIS can have large impacts on the global ocean. First, a collapse of the WAIS has the potential to raise global sea level by 3.3 m (Bamber et al., 2009), and 10% of the observed sea level rise has been attributed to the thinning of the WAIS (Rignot et al., 2008). Second, it may cause the freshening of the shelf water locally in the Amundsen Sea as well as remotely in the Ross Sea (Jacobs et al., 2002; Jacobs and Giulivi, 2010). This may lead to a change in the characteristics of the Antarctic Bottom Water (AABW) formed in the Ross Sea (Jacobs et al., 2002; Rintoul, 2007) and thus may influence the global thermohaline circulation. Therefore, investigations on possible interactions between the melting of small ice shelves in West Antarctica and the large-scale ocean circulation are crucial for understanding climate change in the Southern Ocean.

Several regional models successfully simulate the CDW intrusion onto the Amundsen Sea continental shelf (Thoma et al.,

---

* Corresponding author.
E-mail addresses: Yoshihiro.Nakayama@awi.de (Y. Nakayama), Ralph.Timmermann@awi.de (R. Timmermann), Michael.Schroeder@awi.de (M. Schröder), Hartmut.Hellmer@awi.de (H.H. Hellmer).

http://dx.doi.org/10.1016/j.ocemod.2014.09.007
1463-5003/

2008; Schodlok et al., 2012; Assmann et al., 2013). Schodlok et al. (2012) show that CDW intrudes mainly through the submarine glacial trough on the eastern Amundsen Sea continental shelf (trough E in Fig. 1) all the way into the PIIS cavity. Thoma et al. (2008) and Assmann et al. (2013), on the other hand, show the importance of both trough C (Fig. 1) as well as trough E. Assmann et al. (2013) and Walker et al. (2013) demonstrate that the interaction between an eastward undercurrent and the trough bathymetry steadily provides warm CDW for the continental on-shelf flow.

To study the possible interaction between ice shelf melting in the Amundsen Sea and freshening of the Ross Sea, however, a high resolution circumpolar or global model resolving all the small ice shelves of the WAIS is required. Based on the published model studies investigating ice shelf-ocean interaction, only Timmermann et al. (2012) and Kusahara and Hasumi (2013) resolve all the ice shelves around Antarctica, but both models do not show realistic basal melt rates in the Amundsen Sea especially for PIIS; simulated melt rates for PIIS are 8–13 $\mathrm{Gt\,yr^{-1}}$ for Timmermann et al. (2012) and Kusahara and Hasumi (2013), while observation-based estimates range from 28 to 101 $\mathrm{Gt\,yr^{-1}}$ (Jacobs et al., 1996; Rignot, 1998; Jacobs et al., 2011; Depoorter et al., 2013; Nakayama et al., 2013; Rignot et al., 2013; Dutrieux et al., 2014). Timmermann et al. (2012) attributed the deficiency mainly to a cold bias in the NCEP/NCAR Reanalysis (NCEP-REAN) winter temperature (Assmann et al., 2005). However, a suite of sensitivity studies revealed that even with a warmer forcing, the model still shows an Amundsen Sea much colder than in reality (Nakayama et al., 2013). Using a circumpolar model, Holland et al. (2014) reproduce CDW intrusion onto the Amundsen and Bellingshausen Seas for modeling trends in Antarctic sea ice thickness, but an analysis of the sensitivities of CDW intrusion is not conducted.

With this study, we aim to clarify the main factors controlling warm water intrusions onto the Amundsen Sea continental shelf. We have conducted several sensitivity studies with regard to horizontal resolution, forcing, and horizontal diffusivity (Table 1). We also briefly discuss the importance of grounded icebergs in this region.

2. Model Description

We use the global Finite-Element Sea ice–ice shelf-Ocean Model (FESOM), the details of which are described in Timmermann et al. (2009, 2012) and Timmermann and Hellmer (2013). For the CTRL case, we use a tetrahedral mesh with a horizontal spacing of 100 km along non-Antarctic coasts, which is refined to ~20 km along the Antarctic coast, 10–20 km under the large ice shelves in the Ross and Weddell Seas, ~5 km in the central Amundsen and Bellingshausen Seas, and ~2.5 km in the eastern Amundsen Sea (e.g. Fig. 1). Although St-Laurent et al. (2013) argue that a model resolution of ~1 km is needed to fully resolve mesoscale processes, the maximum resolution is set to ~2.5 km due to computational constraints. While the mesh size varies between 30 and 40 km in the offshore Southern Ocean, it increases to about 400–450 km in the vast basins of the Atlantic and Pacific Oceans. In total, the grid comprises about 3 million grid nodes.

To allow for an adequate representation of ice shelf cavities, we apply a hybrid vertical coordinate system with 46 layers and a z-level discretization in the mid- and low-latitude ocean basins. The top 21 layers along the Antarctic coast are terrain-following (sigma coordinate) for depths shallower than 650 m (Fig. 2). As pointed out by some studies (e.g. Mellor et al., 1994; Griffies et al., 2000; Lemarié et al., 2012), sigma-coordinates have difficulties in accurately computing the horizontal pressure gradient, advection and diffusion, and they induce artificial advection and diffusion along the sigma layers. At the shelf break of the Amundsen Sea, the surface-referenced isopycnals are nearly horizontal (e.g. Fig. 4 of Nakayama et al., 2013), and thus the main diffusion and advection take place horizontally. Therefore, to avoid unrealistic mixing along sigma layers, we restrict sigma levels to the upper 650 m of the water column. In the z-coordinate region, bottom nodes are allowed to deviate from their nominal layer depth in order to allow for a correct representation of bottom topography, similar to the shaved-cells approach in finite-difference z-coordinate models. We note that steep slopes of sigma layers at the entrance to the cavities might influence sub-ice circulation

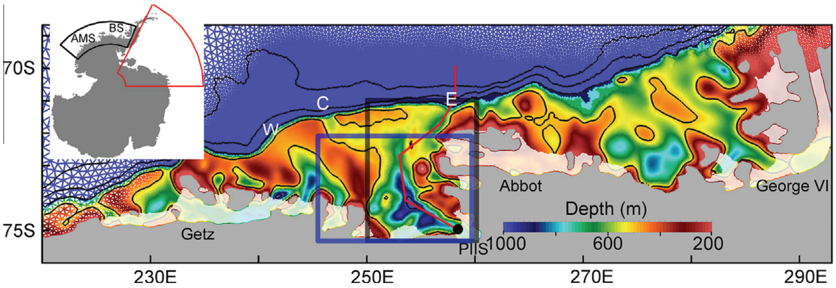

Fig. 1. Horizontal grid of the Amundsen and Bellingshausen region of the global model domain for the CTRL case (HG1), where the color indicates the depth of the model bathymetry. The bathymetry contours of 500, 1000, 2000, and 3000 m are also shown (black lines). Letters E, C, and W denote the submarine glacial troughs located on the eastern, central, and western Amundsen Sea continental shelf, respectively. The location of Getz, Pine Island, Abbot and George VI Ice Shelves are shown. The red line represents the section shown in Fig. 2. The time series of ice front bottom potential temperature (black dot) are shown in Fig. 3. In the area enclosed by the gray rectangle, air temperature and mixed layer depth are averaged, which is shown in Fig. 8. Satellite pictures of the area enclosed by the blue rectangle are shown in Fig. 10. The inset shows Antarctica with regions surrounded by black and red lines denoting the location of the enlarged portion and the location where temperature and salinity are restored, respectively. AMS and BS stand for Amundsen and Bellingshausen Seas. (For interpretation of the references to colour in this figure caption, the reader is referred to the web version of this article.)

Table 1
Description of all the sensitivity cases. The case name, horizontal grid, diffusivity, forcing, and switch for grounded iceberg setting are shown.

Case	CTRL	HG2	HG3	HG4	kh1	kh2	NCEP-REAN	Grounded icebergs	Grounded icebergs with NCEP-REAN
Horizontal grid	HG1	HG2	HG3	HG4	HG1	HG1	HG1	HG1	HG1
k_h	0.9	0.9	0.9	0.9	0.45	0.05	0.9	0.9	0.9
Forcing	NCEP-CFSR	NCEP-CFSR	NCEP-CFSR	NCEP-CFSR	NCEP-CFSR	NCEP-CFSR	NCEP-REAN	NCEP-CFSR	NCEP-REAN
Grounded icebergs	Off	Off	Off	Off	Off	Off	Off	On	On

to some extent. We minimize the error by smoothing ice shelf topography using the criteria of Haney (1991).

Ice shelf draft, cavity geometry, and global ocean bathymetry have been derived from the RTopo-1 dataset (Timmermann et al., 2010). Ocean bathymetry of the Amundsen and Bellingshausen region of the global model is shown in Fig. 1. A Gaussian function with a width depending on the model's horizontal resolution is applied to smooth sea-floor topography in the sigma-coordinate region. Following Timmermann et al. (2012), a steady state for ice shelf thickness and cavity geometry is assumed. For this study, we force the model with 6-hourly atmospheric data from the National Centers for Environmental Prediction Climate Forecast System Reanalysis (NCEP-CFSR, Saha et al., 2010) for the period 1979–1988. Initial temperature and salinity are derived from the World Ocean Atlas (WOA01, Conkright et al., 2002) January mean dataset. In addition, temperature and salinity are restored to the initial values in the Weddell Sea (sector indicated by the red line in the upper left panel of Fig. 1) with a time scale of 30 days, because too coarse vertical and horizontal resolutions do not allow for the descent of dense water in this region in our configuration.

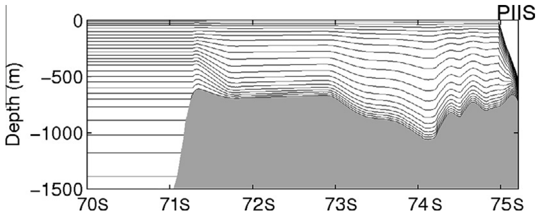

Fig. 2. Vertical coordinate system following the red line in Fig. 1.

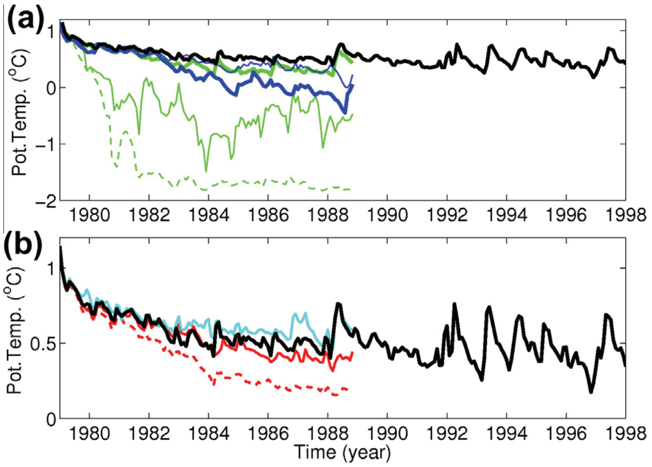

Fig. 3. Time series of ice front bottom potential temperature at 101°W and 75°S (black dot in Fig. 1) (a) for CTRL (black), HG2 (green), HG3 (thin green), HG4 (thin dashed green), NCEP-REAN (blue), and NCEP-REAN with Grounded Iceberg (thin blue) and (b) CTRL (black), kh1 (red), kh2 (dashed red), and Grounded Iceberg (cyan).

3. Results of the control simulation

As shown for slightly different configurations in Timmermann et al., 2012 and Timmermann and Hellmer, 2013, the model reproduces many features of ocean circulation and sea-ice distribution in good agreement with observations. For the region close to the Amundsen Sea in our configuration, the transport of the Ross Gyre is ~26 Sv and the Antarctic Circumpolar Current (ACC) through Drake Passage carries ~140 Sv.

Based on summer CTD observations in the Amundsen Sea, the interannual variation of CDW properties at the bottom of the continental shelf is fairly small. Temporal variations at the PIIS front are less than 0.3 °C for potential temperature and 0.05 for salinity (Fig. 3(a) in Jacobs et al., 2011). Consistent with this, the modeled bottom potential temperature at the PIIS front (101°W and 75°S, black dot in Fig. 1) is fairly stable at ~0.5 °C and fluctuates between ~0.3 °C and ~0.7 °C (1985–1998, black line in Fig. 3) after the initial model spin up (1979–1984). Thus, we validate the model results by comparing the modeled mean bottom potential temperature and salinity with CTD data from 1994 (Nathaniel B. Palmer) and 2010 (Polarstern). We note that the years 1994 and 2010 are selected for a better spatial coverage, but, as mentioned above, interannual variability of bottom temperature is small and observations in other years also show similar results. The modeled intruding CDW properties near the Amundsen/Bellingshausen Sea continental shelf break are close to observations and differences are mostly smaller than 0.3 °C for potential temperature and 0.05

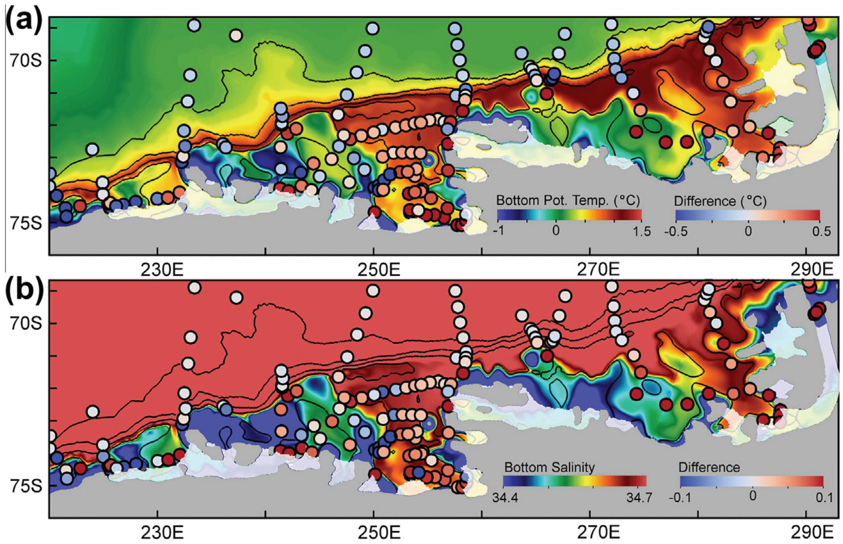

Fig. 4. Simulated mean (a) bottom potential temperature and (b) bottom salinity over 1984 to 1998 for the Amundsen and Bellingshausen Sea continental shelves. The circles indicate the location of CTD data from 1994 and 2010, and the color of the circle shows the difference between observation and model (positive indicates higher observed property than modeled). The bathymetry contours of 500, 1000, 2000, and 3000 m are also shown (black lines).

for salinity (Fig. 4). The difference becomes larger inward from the continental shelf break closer to the coast and some of the largest differences can be found at the ice shelf fronts (Fig. 4). For instance, modeled mean PIIS front potential temperature at the bottom is ~0.5 °C colder than the observed values of ~1.1 °C (Fig. 3). The larger difference near the coast is likely caused by a still too weak CDW intrusion there, which may be related to the influence of horizontal and vertical resolution and/or due to the fact that smoothing of bottom topography in the model has removed some of the smaller scale features. For example, the maximum bottom depth in the deep trough at the PIIS front is around 100–200 m shallower than observed.

Annual means of modeled basal mass loss rates are also nearly stable throughout the model run after initialization (1984–1998, Fig. 5(a)). The mean modeled basal mass loss rates for George VI, Abbot, Pine Island, and Getz Ice Shelves are 88 Gt yr^{-1}, 55 Gt yr^{-1}, 31 Gt yr^{-1}, and 127 Gt yr^{-1}, respectively (Fig. 5 and Table 2), mostly consistent with other observation-based estimates (e.g. Jenkins and Jacobs, 2008; Jacobs et al., 2013; Depoorter et al., 2013; Nakayama et al., 2013; Rignot et al., 2013; Dutrieux et al., 2014). We note that the basal mass loss of PIIS in the model is slightly lower than the lower bound of observation-based estimates. This may be related to the modeled bottom PIIS front temperature ~0.5 °C colder than the observed temperature.

Despite the differences in the ice front potential temperature, the modeled bottom CDW properties on the Amundsen Sea continental shelf are fairly close to the observations, and thus we refer to this simulation as the CTRL case. It is important to note that the modeled physical process of CDW intrusion is also close to the observations. As discussed in Assmann et al. (2013), Nakayama et al. (2013), Walker et al. (2013) and Dutrieux et al. (2014), CDW intrudes onto the continental shelf through submarine glacial troughs (E and C) as an eastward undercurrent and it steadily transports warm CDW close to the shelf break (Fig. 13 in Assmann et al., 2013). This feature is also reproduced in our model (Fig. 6). The CDW intruding from both troughs E and C flows towards PIIS following the bathymetry. For the CDW layer thickness, defined as the thickness of the watermass warmer than 0 °C, thick (~300 m) and thin (~200 m) intrusions originate from troughs E and C, respectively, which is similar to the intrusions observed in 2010 by Nakayama et al. (2013).

4. Sensitivity studies

In this section, we discuss the results of sensitivity studies on horizontal resolution, forcing, horizontal diffusivity, and the effect

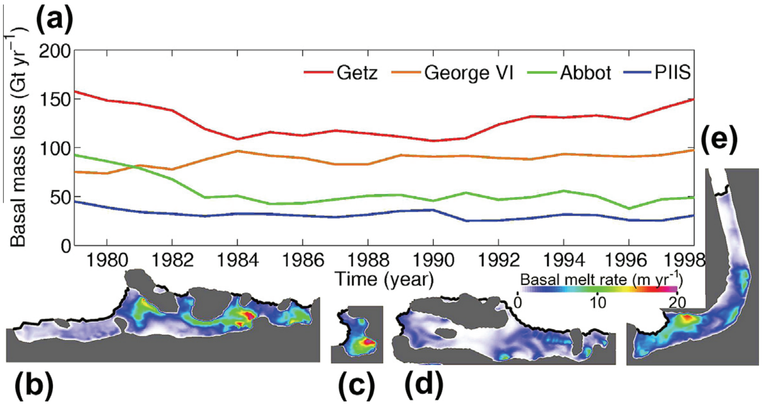

Fig. 5. (a) Annual means of modeled basal ice loss and averaged horizontal distribution of basal melt rates over 1984 to 1998 for (b) Getz, (c) Pine Island, (d) Abbot, and (e) George VI Ice Shelves.

Table 2
Modeled (this study) and observation-based estimates of annual mean basal mass loss (bold) and melt rates. For the model results, annual-means are calculated for the period 1984–1998. In the Method column, G, O, and S stand for glaciological estimate, oceanographic estimate, and satellite estimate, respectively. Difference in the individual estimates might be related to diverging reference periods. Note that ice shelf areas used for conversion between mass losses and melt rates are not identical for the various studies.

Ice shelf	Reference	Mass loss (Gt yr^{-1})	Melt rate (m yr^{-1})	Method
George VI	This study	**88**	3.3	–
	Potter et al. (1984)	**53**	2.1	G, O
	Corr et al. (2002)	**64**	2.8	G, Radar
	Jenkins and Jacobs (2008)	**78–119**	3.1–4.8	O
	Rignot et al. (2013)	**72–106**	3.1–4.5	S
Abbot	This study	**55**	1.8	–
	Depoorter et al. (2013)	**75–97**	2.0–3.4	S
	Rignot et al. (2013)	**33–71**	1.1–2.3	S
Pine Island	This study	**31**	6.6	–
	Jacobs et al. (2011)	**53–85**	22–33	O
	Depoorter et al. (2013)	**81–109**	14–18	S
	Nakayama et al. (2013)	**74**	29	O
	Rignot et al. (2013)	**93–109**	15–17	S
	Dutrieux et al. (2014)	**38–114**	8–24	O
Getz	This study	**127**	3.8	–
	Depoorter et al. (2013)	**117–155**	4–5	S
	Jacobs et al. (2013)	**36–135**	1–4	S
	Rignot et al. (2013)	**135–165**	4–5	S

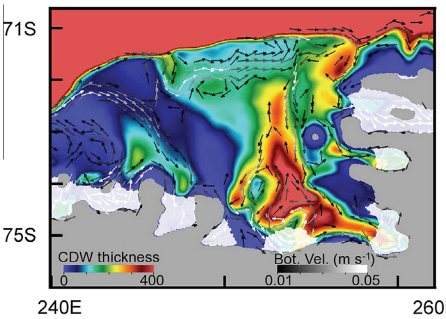

Fig. 6. Simulated mean CDW layer thickness (color) and mean bottom velocity (arrows) averaged over 1984–1998. CDW layer thickness is defined as the thickness of the watermass warmer than 0 °C. Velocity arrows for speeds lower than 0.01 m s^{-1} are not shown. Land and ice shelves are shaded in gray and white, respectively.

of grounded icebergs, summarized in Table 1. For all sensitivity studies, all the model parameters are kept the same as in the CTRL case except for those summarized in Table 1. Experiments are carried out for 10 years.

4.1. Horizontal resolution

For the sensitivity study on horizontal resolution, four experiments with different horizontal grids in the Amundsen and Bellingshausen Seas (HG1, HG2, HG3, and HG4) are performed. We note that the CTRL case uses HG1 (Table 1). The mean resolutions in the Amundsen and Bellingshausen Seas of HG2, HG3, and HG4 are ~5 km, 10 km, and 20 km, respectively (upper left panels of Fig. 7(b)–(d)). For HG1, the horizontal resolution over the eastern Amundsen Sea continental shelf is further increased to ~2.5 km (upper left panel of Fig. 7(a)). Among these four cases, the CTRL run (Fig. 7(a)) shows the warmest PIIS ice front bottom temperature. The HG2 case shows a temporal variability similar to the CTRL case with a slightly lower (~0.2 °C) PIIS ice front bottom temperature, while those of HG3 and HG4 illustrate a sudden decrease of the bottom temperature to around −0.5 °C and −1.8 °C at the PIIS ice front, respectively (Fig. 3, top panel).

The high sensitivity of intruding CDW properties to the horizontal model resolutions indicates that the main physical processes can only be resolved with the resolutions used in HG1 and HG2. Several previous studies investigated the controlling mechanism of the CDW intrusion onto continental shelves (e.g. Klinck and Dinniman, 2010; Wåhlin et al., 2012; Assmann et al., 2013;

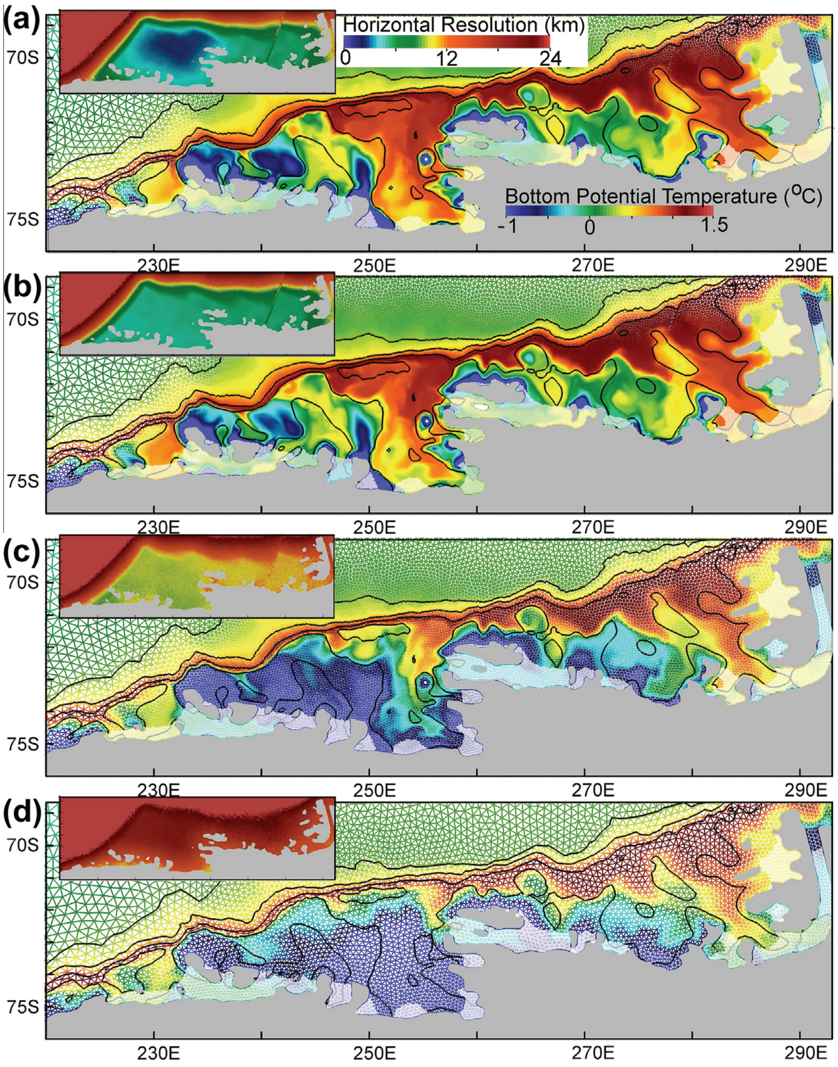

Fig. 7. Horizontal grids of (a) CTRL, (b) HG2, (c) HG3, and (d) HG4 runs with line color showing the simulated monthly mean bottom potential temperature in March 1988. The upper-left panels indicate the horizontal resolution of each grid (HG1–HG4).

St-Laurent et al., 2013). Based on an idealized bathymetry of the Bellingshausen Sea where the Rossby radius of deformation is ~6 km, St-Laurent et al. (2013) found that the mean flow-topography and wave-topography interactions are important. They also show that the latter becomes particularly important when an ocean current is not present off the continental shelf break, and that a model resolution of ~1 km is required to resolve this process. In our model, the wave-topography interaction can not be resolved.

In CTRL and HG2, the interaction between an eastward undercurrent and the trough bathymetry steadily provides warm CDW onto the continental shelf. Thus, as also discussed in Thoma et al. (2008) and Assmann et al. (2013), the mean flow-topography interaction is important for CDW inflow. This agrees with the fact that the mean flow-topography interaction is well reproduced in both St-Laurent et al. (2013) and Assmann et al. (2013) with a model resolutions of ~3 km. On the other hand, HG3 shows a weaker intrusion compared to CTRL and HG2 (Fig. 7(c)). The coarsest mesh, HG4 does not show any signature of CDW in the Amundsen Sea (Fig. 7(d)), and bottom temperature is at ~-1.8 °C. This is because the mean flow-topography interaction can not be resolved with coarse model resolutions. Thus, to resolve CDW intrusions onto the Amundsen Sea continental shelf, a horizontal resolution of about 5 km is required. However, the modeled ice front temperature of the CTRL run is still ~0.5 °C lower than observed. This may be related to the still insufficient resolution; a horizontal resolution of ~1 km, resolving wave-topography interaction, may transport more warm water across the continental shelf break, which remains, however, for future considerations.

4.2. Forcing

For the sensitivity study on forcing, an experiment with NCEP-REAN forcing (NCEP-REAN) is conducted. The NCEP-REAN run shows a continuous bottom temperature decrease at the PIIS front, dropping below 0 °C in 1988 (Fig. 3). The difference between NCEP-REAN and NCEP-CFSR runs is mainly caused by the different air temperature over the eastern Amundsen Sea. Averaged over the eastern Amundsen Sea (area enclosed by the gray line in Fig. 1), the NCEP-CFSR winter air temperature is ~20 °C warmer than that of the NCEP-REAN fields (Fig. 8). As suggested by Timmermann et al. (2012), this cold bias in the NCEP-REAN forcing results in deeper mixed layer depths (here defined as the greatest depth with potential temperature below −1 °C) over large areas of the eastern Amundsen Sea continental shelf. The depth continues to grow until the end of the simulation, reaching more than 300 m (Fig. 8). This deepening of the mixed layer weakens the CDW intrusion. In contrast, the depth of the cold surface mixed layer adjusts to about 220 m for the NCEP-CFSR run, which is consistent with observations (e.g. Fig. 4 in Nakayama et al., 2013).

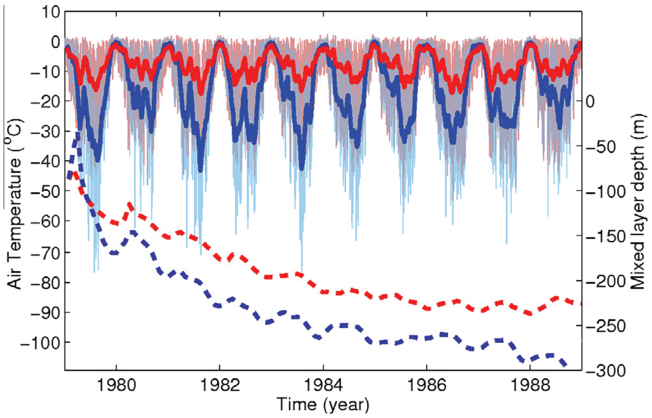

Fig. 8. The mean air temperature for NCEP-CFSR (light red) and NCEP-REAN (light blue) runs in the region enclosed by the gray rectangle in Fig. 1 and 1 month moving averages of these two (NCEP-CFSR: red, NCEP-REAN: blue). The averaged mixed layer depths for CTRL (red dashed) and NCEP-REAN (blue dashed) cases averaged over the same region are also shown. (For interpretation of the references to colour in this figure caption, the reader is referred to the web version of this article.)

4.3. Horizontal diffusivity

Following Timmermann et al. (2009), the lateral diffusivity ν_i is given as a linear function of the element area Δ_i as $\nu_i = 4.0 \times 10^{-7} k_h \Delta_i$, where i and k_h is the number of the element and the scaling factor for diffusion, respectively. For the following sensitivity study, different values of k_h are chosen to investigate the effect of diffusion, which are named kh1 and kh2 cases as in Table 1.

Comparison of the time series of kh1, and kh2 with CTRL shows that the kh1 time series is similar with a slightly lower potential temperature of ~0.2 °C, while kh2 shows a continuous potential temperature decreases to ~ 0.2 °C until 1988 (Fig. 3). The difference is considered to be caused by two factors. With a larger k_h, CDW of open ocean origin can approach closer to the continental shelf. This results in warmer CDW properties covering the shelf break. For instance, CDW temperatures intruding via trough E are about 1 °C, 0.95 °C, and 0.85 °C for the period Jan–March 1988 for CTRL, kh1, and kh2, respectively (Fig. 9). In addition, higher diffusivity also increases horizontal mixing and thus transports more warm CDW onshore. The averaged bottom temperature of CTRL, kh1, and kh2 are 0.5 °C, 0.4 °C, and 0.2 °C between 1984–1988 at the bottom of PIIS front, respectively (Fig. 3). Thus, both the intrusion of slightly warmer CDW as well as increased onshore transport causes warmer ice front bottom temperatures, but the difference is small compared to the sensitivities on horizontal resolution and forcing.

4.4. Grounded icebergs

As shown in the ENVISAT AVSAR images from 21 and 22 June 2010 (Fig. 10), several icebergs are grounded off the Bear Peninsula along the 400-m isobath. Based on other ENVISAT images (not shown), these grounded icebergs are always present between 2003 and 2010. Considering the bottom bathymetry and the amount of icebergs produced to the east of this region, a barrier of grounded iceberg is considered to exist nearly permanently. This barrier prevents a sea-ice transport from the eastern to the central Amundsen Sea. Since the wind is mostly blowing westwards close to the coast (Assmann et al., 2013), polynyas are formed near the PIIS front and off the Bear Peninsula (Fig. 10). Following Arrigo et al. (2012), they are named Pine Island polynya and Amundsen polynya, respectively, and they are also visible in the satellite pictures of this region (e.g. Fig. 10). During autumn and winter, polynyas are areas of enhanced sea-ice formation. Mapping of annual ice production in the Southern Ocean based on a heat budget calculation with satellite-derived sea-ice thickness (Tamura et al., 2008), as well as circum-Antarctic coastal polynya areas (Kern, 2009) both indicate the persistent formation of these two polynyas in the 1990s and the 2000s. However, in our model, the Amundsen polynya is not present due to the absence of grounded icebergs. Therefore, in the Grounded Iceberg run, the sea-ice velocity in the region enclosed by the cyan line in Fig. 10 is set to zero to mimic the influence of grounded icebergs on sea-ice drift.

The ice front potential temperature in the Grounded Iceberg experiment is slightly warmer (~0.1 °C) than in the CTRL simulation, and several CDW intrusion signals are only present in the Grounded Iceberg run (Fig. 3). This is because the blocking effect of grounded icebergs reduces sea-ice export from Pine Island polynya and decreases sea-ice formation there. This likely

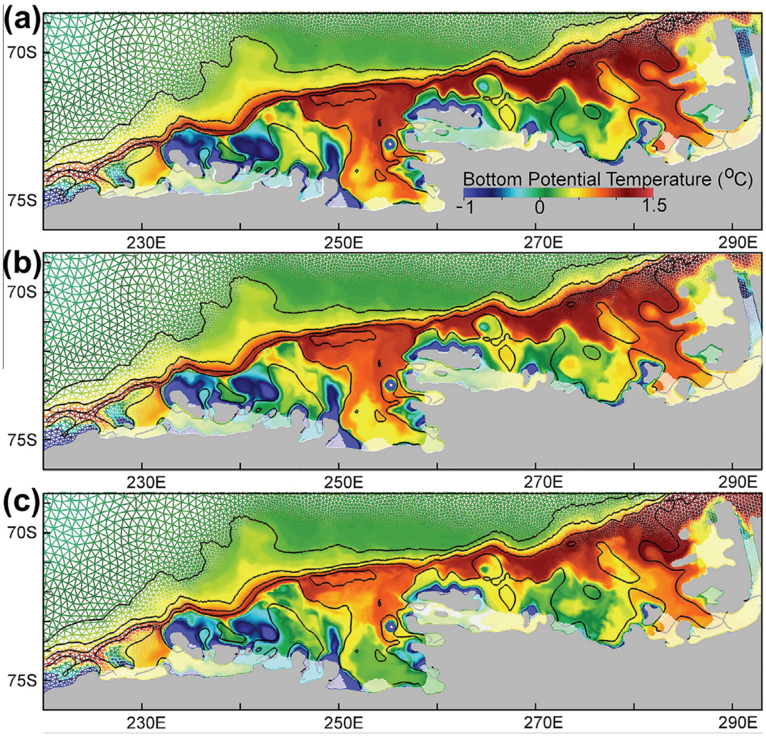

Fig. 9. Horizontal grids of (a) CTRL, (b) kh1, and (c) kh2 runs. Colors indicate the monthly mean simulated bottom potential temperature in March 1988.

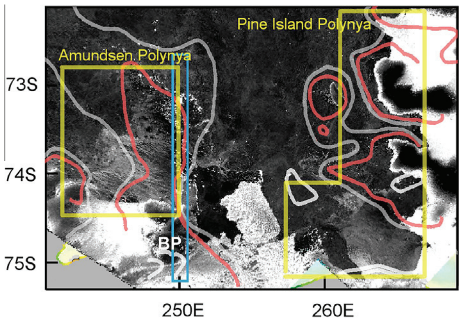

Fig. 10. ENVISAT quick-look image from 25 and 26 June 2010. The 400 m (white) and 500 m (red) bathymetric contours are shown. In the region enclosed with the cyan rectangles, sea-ice velocity is restored to zero to mimic the effect of grounded icebergs. The locations of the Amundsen polynya and the Pine Island polynya are enclosed with yellow lines. BP denote the Bear Peninsula. (For interpretation of the references to colour in this figure caption, the reader is referred to the web version of this article.)

decreases the Winter Water (WW) layer thickness at the ice front, making it easier for CDW to penetrate into the PIIS cavity. The difference of the sea-ice formation rate between these two experiments is large (about 30% reduction of total sea-ice production in the Pine Island Polynya in the Grounded Iceberg case). This influence becomes more prominent for a colder forcing: For the grounded iceberg setting with NCEP-REAN forcing, the ice front potential temperature mostly remains at ~0.4 °C (Fig. 3), which is ~ 0.4 °C warmer than in the NCEP-REAN run without grounded icebergs. This may indicate that the grounded icebergs stabilize the CDW intrusions in the case of a cold event, but the influence of grounded icebergs is not large in runs with NCEP-CFSR forcing.

5. Summary

Warm CDW intrudes onto the continental shelves of the Amundsen and Bellingshausen Seas through submarine glacial troughs and flows into the cavities beneath the floating extensions of the WAIS, resulting in high basal melt rates (e.g. Walker et al., 2007; Wåhlin et al., 2010; Jacobs et al., 2011; Jenkins et al., 2010; Assmann et al., 2013). However, none of the high-resolution global models, resolving all small Antarctic ice shelves, has been able to reproduce the CDW intrusion into the Amundsen and Bellingshausen Seas so far. In this study, we are able to reproduce CDW intrusions and ice shelf basal melting in the Amundsen and Bellingshausen Seas using a combination of grid refinement and NCEP-CFSR forcing in the global Finite-Element Sea ice–ice shelf-Ocean Model (FESOM).

Modeled melt rates of George VI, Abbot, Pine Island, and Getz Ice Shelves in the CTRL simulation are within the range of observation-based estimates (Table 2) (e.g. Jacobs et al., 2011, 2012; Depoorter et al., 2013; Rignot et al., 2013). Although CDW properties at several ice shelf fronts away from the continental shelf break still remain colder than reality by ~0.5 °C, our model is able to reproduce CDW intrusion onto the Amundsen Sea continental shelf much closer to the reality than in the models of Timmermann et al. (2012) or Kusahara and Hasumi (2013) (Fig. 4). As discussed in Thoma et al. (2008), Assmann et al. (2013) and Walker et al. (2013) CDW intrudes onto the continental shelf through submarine glacial troughs supported by an eastward undercurrent along the continental shelf break, which steadily provides warm CDW (Fig. 6). To investigate the importance of horizontal resolution, atmospheric forcing, horizontal diffusivity, and the effect of grounded icebergs, several sensitivity studies have been conducted. A horizontal resolution of about 5 km or smaller (about the length scale of the Rossby deformation radius) is required over the continental shelves of Amundsen and Bellingshausen Seas to simulate the CDW intrusion realistically (Fig. 7). Such small horizontal resolution is required to resolve the mean flow-topography interaction. A cold bias in the NCEP/NCAR reanalysis data makes it difficult for CDW to intrude onto the continental shelf, which is related to the deepening of the cold surface mixed layer (Fig. 8). The CDW intrusion is not overly sensitive to the strength of diffusion. The effect of grounded icebergs located off Bear Peninsula is minor, but they may act as a buffer to an anomalously cold year.

The total basal melting is estimated to be $\sim 660\,\mathrm{Gt\,yr^{-1}}$ for all ice shelves in the Bellingshausen and Amundsen Seas (Rignot et al., 2013). This melting might cause the freshening of shelf water in the Amundsen Sea, downstream in the Ross Sea (Jacobs et al., 2002), and in the Ross Gyre with consequences for the global thermohaline circulation (Jacobs et al., 2002; Rintoul, 2007). This suggests a possible link between the small ice shelves in West Antarctica and the large-scale ocean circulation, which may be crucial for the understanding of climate change in the Southern Ocean. Our study shows that such complex systems can only be investigated with a high-resolution circumpolar or global model resolving all the small ice shelves around Antarctica, and the small-scale topographic features, namely the submarine glacial troughs on the Amundsen Sea continental shelf. A finite-element model provides an appropriate framework to follow this direction, but the increase of the computational burden remains as a severe limitation here.

Acknowledgments

We thank Sergey Danilov, Dmitry Sidorenko, and Qiang Wang for their help and support and Shigeru Aoki, Karen M. Assmann, Pierre Dutrieux, Hiroyasu Hasumi, Paul Holland, Adrian Jenkins, Kazuya Kusahara, Yoshimasa Matsumura, and Kay I. Ohshima, for their useful comments and suggestions. Insightful comments from two anonymous reviewers were very helpful for improving the manuscript.

References

Arrigo, K.R., Lowry, K.E., van Dijken, G.L., 2012. Annual changes in sea ice and phytoplankton in polynyas of the Amundsen Sea, Antarctica. Deep Sea Res. II 71, 5–15.

Assmann, K.M., Hellmer, H.H., Jacobs, S.S., 2005. Amundsen sea ice production and transport. J. Geophys. Res. 110.

Assmann, K., Jenkins, A., Shoosmith, D., Walker, D., Jacobs, S., Nicholls, K., 2013. Variability of circumpolar deep water transport onto the Amundsen Sea continental shelf through a shelf break trough. J. Geophys. Res. 118, 6603–6620.

Bamber, J.L., Riva, R.E.M., Vermeersen, B.L.A., LeBrocq, A.M., 2009. Reassessment of the potential sea-level rise from a collapse of the West Antarctic Ice Sheet. Science 324, 901–903.

Conkright, M., Antonov, J., Baranova, O., Boyer, T., Garcia, H., Gelfeld, R., Johnson, D., Locarnini, R., O'Brien, T., Smolyar, I., et al., 2002. In: Levitus, S. (Ed.), World ocean database 2001, vol. 1, NOAA Atlas NESDIS, vol. 42. US Government Printing Office, Washington, DC.

Corr, H.F., Jenkins, A., Nicholls, K.W., Doake, C., 2002. Precise measurement of changes in ice-shelf thickness by phase-sensitive radar to determine basal melt rates. Geophys. Res. Lett. 29, 73–1.

Depoorter, M., Bamber, J., Griggs, J., Lenaerts, J., Ligtenberg, S., van den Broeke, M., Moholdt, G., 2013. Calving fluxes and basal melt rates of Antarctic ice shelves. Nature.

Dutrieux, P., De Rydt, J., Jenkins, A., Holland, P.R., Ha, H.K., Lee, S.H., Steig, E.J., Ding, Q., Abrahamsen, E.P., Schröder, M., 2014. Strong sensitivity of pine island ice-shelf melting to climatic variability. Science 343, 174–178.

Griffies, S.M., Pacanowski, R.C., Hallberg, R.W., 2000. Spurious diapycnal mixing associated with advection in a z-coordinate ocean model. Mon. Weather Rev. 128, 538–564.

Haid, V., Timmermann, R., 2013. Simulated heat flux and sea ice production at coastal polynyas in the southwestern Weddell Sea. J. Geophys. Res. 118, 2640–2652.

Haney, R.L., 1991. On the pressure gradient force over steep topography in sigma coordinate ocean models. J. Phys. Oceanogr. 21, 610–619.

Holland, P.R., Bruneau, N., Enright, C., Losch, M., Kurtz, N.T., Kwok, R., 2014. Modelled trends in Antarctic sea ice thickness. J. Clim. 27, 3784–3801.

Jacobs, S.S., Giulivi, C.F., 2010. Large multidecadal salinity trends near the Pacific–Antarctic continental margin. J. Clim. 23, 4508–4524.

Jacobs, S.S., Hellmer, H.H., Jenkins, A., 1996. Antarctic ice sheet melting in the Southeast Pacific. Geophys. Res. Lett. 23, 957–960.

Jacobs, S.S., Giulivi, C.F., Mele, P.A., 2002. Freshening of the Ross Sea during the late 20th century. Science 297, 386–389.

Jacobs, S.S., Jenkins, A., Giulivi, C.F., Dutrieux, P., 2011. Stronger ocean circulation and increased melting under Pine Island Glacier ice shelf. Nat. Geosci. 4, 519–523.

Jacobs, S., Jenkins, A., Hellmer, H., Giulivi, C., Nitsche, F., Huber, B., Guerrero, R., 2012. The Amundsen Sea and the Antarctic Ice Sheet. Oceanography 25, 154–163.

Jacobs, S., Giulivi, C., Dutrieux, P., Rignot, E., Nitsche, F., Mouginot, J., 2013. Getz Ice Shelf melting response to changes in ocean forcing. J. Geophys. Res. 118, 4152–4168.

Jenkins, A., Jacobs, S., 2008. Circulation and melting beneath George VI ice shelf, Antarctica. J. Geophys. Res 113, C04013.

Jenkins, A., Dutrieux, P., Jacobs, S.S., McPhail, S.D., Perrett, J.R., Webb, A.T., White, D., 2010. Observations beneath Pine Island Glacier in West Antarctica and implications for its retreat. Nat. Geosci. 3, 468–472.

Joughin, I., Alley, R.B., 2011. Stability of the West Antarctic ice sheet in a warming world. Nat. Geosci. 4, 506–513.

Kern, S., 2009. Wintertime Antarctic coastal polynya area: 1992–2008. Geophys. Res. Lett. 36.

Klinck, J., Dinniman, M., 2010. Exchange across the shelf break at high southern latitudes. Ocean Sci. Discuss. 6, 513–524.

Kusahara, K., Hasumi, H., 2013. Modeling Antarctic ice shelf responses to future climate changes and impacts on the ocean. J. Geophys. Res. 118, 2454–2475.

Lemarié, F., Kurian, J., Shchepetkin, A.F., Jeroen Molemaker, M., Colas, F., McWilliams, J.C., 2012. Are there inescapable issues prohibiting the use of terrain-following coordinates in climate models? Ocean Modell. 42, 57–79.

Martinson, D., McKee, D., 2012. Transport of warm Upper Circumpolar Deep Water onto the western Antarctic Peninsula continental shelf. Ocean Sci. 8, 433–442.

Mellor, G., Ezer, T., Oey, L., 1994. The pressure gradient conundrum of sigma coordinate ocean models. J. Atmos. Ocean. Technol. 11, 1126–1134.

Moffat, C., Owens, B., Beardsley, R.C., 2009. On the characteristics of Circumpolar Deep Water intrusions to the west Antarctic Peninsula continental shelf. J. Geophys. Res., 114.

Nakayama, Y., Schröder, M., Hellmer, H.H., 2013. From circumpolar deep water to the glacial meltwater plume on the eastern Amundsen Shelf. Deep Sea Res. I 77, 50–62.

Nakayama, Y., Timmermann, R., Hellmer, H., 2013. On the difficulties of modeling the Amundsen Sea embayment. EGU Gen. Assembly Conf. Abst. 15, 1072.

Orsi, A.H., Johnson, G.C., Bullister, J.L., 1999. Circulation, mixing, and production of Antarctic Bottom Water. Prog. Oceanogr. 43, 55–109.

Potter, J., Paren, J., Loynes, J., 1984. Glaciological and oceanographic calculations of the mass balance and oxygen isotope ratio of a melting ice shelf. J. Glaciol. 30, 161–170.

Rignot, E.J., 1998. Fast recession of a West Antarctic glacier. Science 281, 549.

Rignot, E., Bamber, J.L., den Broeke, M.R.V., Davis, C., Li, Y., de Berg, W.J.V., Meijgaard, E.V., 2008. Recent Antarctic ice mass loss from radar interferometry and regional climate modelling. Nat. Geosci. 1, 106–110.

Rignot, E., Jacobs, S.S., Mouginot, J., Scheuchl, B., 2013. Ice-shelf melting around Antarctica. Sci. Express 341, 226–270.

Rintoul, S.R., 2007. Rapid freshening of Antarctic Bottom Water formed in the Indian and Pacific oceans. Geophys. Res. Lett. 34, L06606.

Saha, S., Moorthi, S., Pan, H.L., Wu, X., Wang, J., Nadiga, S., Tripp, P., Kistler, R., Woollen, J., Behringer, D., et al., 2010. The NCEP climate forecast system reanalysis. Bull. Am. Meteorol. Soc. 91, 1015–1057.

Schmitz, J.W.J., 1995. On the interbasin-scale thermohaline circulation. Rev. Geophys. 33, 151–173.

Schodlok, M.P., Menemenlis, D., Rignot, E., Studinger, M., 2012. Sensitivity of the ice shelf ocean system to the sub-ice shelf cavity shape measured by NASA IceBridge in Pine Island Glacier, West Antarctica. Ann. Glaciol. 53, 156–162.

Shepherd, A., Ivins, E., Geruo, A., Barletta, V., Bentley, M., Bettadpur, S., Briggs, K., Bromwich, D., Forsberg, R., Galin, N., et al., 2012. A reconciled estimate of ice-sheet mass balance. Science 338, 1183–1189.

St-Laurent, P., Klinck, J.M., Dinniman, M.S., 2013. On the Role of Coastal Troughs in the Circulation of Warm Circumpolar Deep Water on Antarctic Shelves. J. Phys. Oceanogr. 43, 51–64.

Tamura, T., Ohshima, K.I., Nihashi, S., 2008. Mapping of sea ice production for Antarctic coastal polynyas. Geophys. Res. Lett. 35, L07606.

Thoma, M., Jenkins, A., Holland, D., Jacobs, S., 2008. Modelling circumpolar deep water intrusions on the Amundsen Sea continental shelf, Antarctica. Geophys. Res. Lett. 35.

Timmermann, R., Hellmer, H.H., 2013. Southern Ocean warming and increased ice shelf basal melting in the twenty-first and twenty-second centuries based on coupled ice-ocean finite-element modelling. Ocean Dyn. 63, 1011–1026.

Timmermann, R., Danilov, S., Schröter, J., Böning, C., Sidorenko, D., Rollenhagen, K., 2009. Ocean circulation and sea ice distribution in a finite element global sea ice–ocean model. Ocean Modell. 27, 114–129.

Timmermann, R., Brocq, A.L., Deen, T., Domack, E., Dutrieux, P., Galton-Fenzi, B., Hellmer, H., Humbert, A., Jansen, D., Jenkins, A., et al., 2010. A consistent data set of Antarctic ice sheet topography, cavity geometry, and global bathymetry. Earth Syst. Sci. Data 2, 261–273.

Timmermann, R., Wang, Q., Hellmer, H., 2012. Ice-shelf basal melting in a global finite-element sea-ice/ice-shelf/ocean model. Ann. Glaciol. 53, 303–314.

Wåhlin, A.K., Yuan, X., Björk, G., Nohr, C., 2010. Inflow of Warm Circumpolar Deep Water in the Central Amundsen Shelf. J. Phys. Oceanogr. 40, 1427–1434.

Wåhlin, A.K., Muench, R.D., Arneborg, L., Björk, G., Ha, H.K., Lee, S.H., Alsén, H., 2012. Some implications of Ekman layer dynamics for cross shelf exchange in the Amundsen Sea. J. Phys. Oceanogr. 42, 1461–1474.

Wåhlin, A., Kalén, O., Arneborg, L., Björk, G., Carvajal, G., Ha, H., Kim, T., Lee, S., Lee, J., Stranne, C., 2013. Variability of Warm Deep Water Inflow in a Submarine Trough on the Amundsen Sea Shelf. J. Phys. Oceanogr., 43.

Walker, D.P., Brandon, M.A., Jenkins, A., Allen, J.T., Dowdeswell, J.A., Evans, J., 2007. Oceanic heat transport onto the Amundsen Sea shelf through a submarine glacial trough. Geophys. Res. Lett. 34, 1–4.

Walker, D.P., Jenkins, A., Assmann, K.M., Shoosmith, D.R., Brandon, M.A., 2013. Oceanographic observations at the shelf break of the Amundsen Sea, Antarctica. J. Geophys. Res. 118, 2906–2918.

Wingham, D.J., Wallis, D.W., Shepherd, A., 2009. Spatial and temporal evolution of Pine Island Glacier thinning, 1995–2006. Geophys. Res. Lett. 36, L17501.

5

Modeling the spreading of glacial melt water from the Amundsen and Bellingshausen Seas

Yoshihiro Nakayama [1], Ralph Timmermann [1],
Christian B. Rodehacke [2], Michael Schröder [1], and Hartmut H. Hellmer [1]

*1: Alfred Wegener Institute, Helmholtz Centre for Polar and Marine Research
in Bremerhaven, Germany*

2: Danish Meteorological Institute, Copenhagen, Denmark

accepted in Journal of Geophysical Research Letters

Y. Nakayama conducted the all the model experiments. Implementation of the ocean-atmosphere gas exchange modules was mainly conducted by Y. Nakayama with support from C.B. Rodehacke. Y. Nakayama wrote all the text of the paper and prepared all the figures. All authors participated in the discussion of the model results and in revising the paper.

Modeling the spreading of glacial melt water from the Amundsen and Bellingshausen Seas

Y. Nakayama,[1] R. Timmermann[1], C. B. Rodehacke[2], M. Schröder[1], H. H. Hellmer[1]

Corresponding author: Y. Nakayama, Alfred Wegener Institute Bussestrasse 24 D-27570 Bremerhaven, Germany. (Yoshihiro.Nakayama@awi.de)

[1]Alfred Wegener Institute, Bremerhaven, Germany.

[2]Danish Meteorological Institute, Copenhagen, Denmark

It has been suggested that an increased melting of continental ice in the Amundsen Sea (AS) and Bellinghausen Sea (BS) is a likely source of the observed freshening of Ross Sea (RS) water. To test this hypothesis, we simulate the spreading of glacial melt water using the Finite-Element Sea-ice/ice-shelf/Ocean Model. Based on the spatial distribution of simulated passive tracers, most of the basal melt water from AS ice shelves flows towards the RS with more than half of the melt originating from the Getz Ice Shelf. Further, the model results show that a slight increase of the basal mass loss can substantially intensify the transport of melt water into the RS due to a strengthening of the melt-driven shelf circulation and the westward flowing coastal current. This supports the idea that the basal melting of AS and BS ice shelves is one of the main sources for the RS freshening.

1. Introduction

The ice shelves and glaciers of the West Antarctic Ice Sheet (WAIS) are thinning rapidly especially in the Amundsen Sea (AS) and Bellingshausen Sea (BS) [e.g. *Pritchard et al.*, 2012; *Shepherd et al.*, 2012; *Rignot et al.*, 2013]. This is mainly caused by strong basal melting due to the interaction of deep-drafted ice shelves with warm Circumpolar Deep Water (CDW, about 3 °C warmer than the in-situ freezing point) flowing onto the continental shelves through submarine glacial troughs [e.g. *Jacobs et al.*, 2011; *Pritchard et al.*, 2012]. Basal mass loss of the AS and BS ice shelves is estimated to be $\sim$ 500 and 150 Gt yr^{-1}, respectively, according to satellite analyses [*Rignot et al.*, 2013]. This is about half of the total basal melting of all Antarctic ice shelves [*Depoorter et al.*, 2013; *Rignot et al.*, 2013].

In the Ross Sea (RS), shelf water salinity has declined by 0.03 per decade over the past 50 years [*Jacobs et al.*, 2002; *Jacobs and Giulivi*, 2010]. Since the freshening may be responsible for a change in the characteristics of the Antarctic Bottom Water (AABW) formed in the RS [*Jacobs et al.*, 2002; *Rintoul*, 2007] and thus may influence the global thermohaline circulation, understanding the possible link between the melting of West Antarctic ice shelves and the freshening of the RS is crucial for assessing climate change in the Southern Ocean. Although changes in precipitation, sea-ice production, and ocean circulation are considered to be possible reasons for the freshening, increased melting of continental ice upstream in the AS and BS is suggested to be the likely source of the additional freshwater [*Jacobs et al.*, 2002; *Jacobs and Giulivi*, 2010]. The salinity of the westward flowing coastal current into the RS has decreased by 0.08 per decade over the past 30 years, and oxygen isotope data of the shelf water show an increasing glacial melt signal, supporting this hypothesis [*Jacobs and Giulivi*, 2010].

Although high-resolution circumpolar or global models resolving all the small ice shelves of the WAIS are required to study this hypothesis, it has been difficult to simulate the CDW intrusions onto the AS and BS continental shelves in these models [*Timmermann et al.*, 2012; *Kusahara and Hasumi*, 2013]. However, *Nakayama et al.* [2014] successfully reproduced the CDW intrusions onto the continental shelf and basal mass loss rates of the major AS and BS ice shelves using the global Finite-Element Sea-ice/ice-shelf/Ocean Model (FESOM, *Timmermann et al.* [2012]). In this study, we simulate the spreading of basal melt water from the AS and BS ice shelves using FESOM, and investigate whether the basal melt water from these ice shelves flows into the RS. We also conduct two sensitivity experiments, assessing this hypothesis, and discuss the sensitivity of basal melt water transport into the RS to the strength of the basal mass loss of AS and BS ice shelves.

2. Model

We use the global FESOM, the details of which are described in *Timmermann et al.* [2009, 2012]; *Timmermann and Hellmer* [2013], and *Nakayama et al.* [2014]. We use a tetrahedral mesh with a horizontal spacing of 100 km along non-Antarctic coasts, which is refined to ∼20 km along the Antarctic coast, 10-20 km under the large ice shelves in the RS, ∼5 km in the central AS and BS, and ∼2.5 km in the eastern AS (Fig. 1). To allow for an adequate representation of ice shelf cavities, we apply a hybrid vertical coordinate system with 46 layers and a z-level discretization in the mid- and low-latitude ocean basins. The top 21 layers along the Antarctic coast are terrain-following (sigma coordinate) for depths shallower than 650 m (Fig.2 in *Nakayama et al.* [2014]). In the z-coordinate region (open ocean), bottom nodes are allowed to deviate from their nominal layer depth in order to allow for a correct representation of bottom topography, similar to the shaved-cell approach in finite difference models. Ice shelf draft, cavity geometry, and global ocean bathymetry have been derived from the RTopo-1 dataset (*Timmermann et al.* [2010]). Ocean bathymetry of the AS, BS, and RS regions of the global model is shown in Fig. 1. A Gaussian function with a width depending on the model's horizontal resolution is applied to smooth ice shelf draft and sea-floor topography in the sigma-coordinate region.

Following *Timmermann et al.* [2012], we assume a steady state for ice shelf thickness and cavity geometry, and compute basal mass loss rate at ice-shelf bases as proposed by *Hellmer and Olbers* [1989] and refined by *Holland and Jenkins* [1999]. Turbulent fluxes of heat and salt are computed with coefficients depending on the friction velocity, following *Jenkins* [1991]. To trace the basal melt water, we do not implement geochemical tracers [*Rodehacke et al.*, 2007] but we use virtual passive tracers, which are released at the same rate as melting occurs at the ice shelf bases. Several independent virtual passive tracers are used to identify detailed pathways of basal melt water from the different ice shelves in the AS and BS.

For this study, we force the model with 6-hourly atmospheric data from the National Centers for Environmental Prediction Climate Forecast System Reanalysis (NCEP-CFSR, *Saha et al.* [2010]) for the period 1979-1988. The model is spun-up for 5 years by repeating the 1979-forcing, because ice-shelf basal mass loss for most ice shelves approaches a quasi-steady state within the first 5 years of integration [*Timmermann et al.*, 2012]. Initial temperature and salinity are derived from the World Ocean Atlas (WOA01, *Conkright et al.* [2002]) January mean data set. In addition, temperature and salinity are restored to the initial values with a time scale of 30 days in the vicinity of Antarctic Peninsula at depths deeper than 150 m (sector indicated by the black line in the upper left panel of Fig. 1), because too coarse vertical and horizontal resolutions there do not allow for the descent of dense water to great depths.

3. Results

3.1. Model Validation

As shown for slightly different configurations in *Timmermann et al.* [2012] and *Timmermann and Hellmer* [2013], the model reproduces many features of ocean circulation and sea-ice distribution in good agreement with observations. In the configuration used here, e.g., the transport of the Ross Gyre is ∼26 Sv and the Antarctic Circumpolar Current (ACC) carries ∼140 Sv through Drake Passage (Fig. 1). For the AS, BS, and RS regions (160°E-70°W), the modeled winter (September) sea-ice extent is similar to observations [*Cavalieri et al.*, 2006], while summer (March) sea-ice extent is overestimated by ∼24%. However, the spatial distribution of summer sea ice is now closer to reality with more sea ice remaining in the AS and BS compared to *Timmermann et al.* [2012] (not shown). The model results show CDW intrusions through submarine glacial troughs into the ice shelf cavities, consistent with observations and regional model studies [*Jacobs and Giulivi*, 2010; *Schodlok et al.*, 2012; *Assmann et al.*, 2013; *Nakayama et al.*, 2013; *Walker et al.*, 2013], and simulated mean bottom temperature and salinity in the AS and BS are mostly close to near-bottom CTD observations (Fig. 4 in *Nakayama et al.* [2014]). Modeled melt water fractions are about 1-2 % at the southern George VI and Pine Island Ice Shelf fronts at a depth of ∼200m, which is also consistent with observations [*Jenkins and Jacobs*, 2008; *Jacobs et al.*, 2011; *Nakayama et al.*, 2013].

There are several studies estimating the basal mass loss of West Antarctic ice shelves based on satellite, glaciological, and oceanographic observations ([e.g., *Jacobs et al.*, 2011; *Depoorter et al.*, 2013; *Rignot et al.*, 2013]). After the spin-up phase, modeled basal mass loss is nearly stable throughout the integration [*Nakayama et al.*, 2014]. For the ice shelves in the AS and BS, the rates of total basal mass loss are 262 Gt yr^{-1} and 162 Gt yr^{-1}, respectively, which are consistent with the observation-based estimates (Supplementary Table S1). For the individual ice shelves in the AS and BS, modeled basal mass loss rates are mostly within or close to the ranges of observation-based estimates ([e.g., *Jacobs et al.*, 2011; *Depoorter et al.*, 2013; *Rignot et al.*, 2013]) (Supplementary Tables S1 and S2) . The differences are large, however, for the Thwaites, Crosson, and Doston Ice Shelves, where the modeled (observed) basal mass loss is 27 (91-105), 3.3 (35-43), and 20 (41-49) Gt yr^{-1}, respectively. The modeled basal mass loss of Pine Island Ice Shelf is slightly lower than the lower bound of the observation-based estimates, and it is highly underestimated when compared to the estimates from *Jacobs et al.* [2011], *Depoorter et al.* [2013], and *Rignot et al.* [2013]. These discrepancies may be caused by modeled CDW intrusions still being too weak [*Nakayama et al.*, 2014], and ice front temperatures still being lower than observed (e.g., ∼0.5 °C lower at the Pine Island Ice Shelf front). It is also possible that the

Rignot et al. [2013] estimates, using the volume flux divergence of ice shelves in 2007 and 2008, are biased towards higher values. For Pine Island Ice Shelf, the *Rignot et al.* [2013] estimate is close to the upper bound of the observation-based estimates (Supplementary Table S2). It is also known that the basal mass loss of Pine Island Ice Shelf decreased to less than half of the estimate from *Rignot et al.* [2013] in summer 2012 [*Dutrieux et al.*, 2014]. For ice shelves in the RS (Land, Nickerson, Sulzberger, Swinburne, and Ross Ice Shelves), the total basal mass loss is 159 Gt yr^{-1}, which is overestimated by $\sim$ 25-50% compared to the observation-based estimate. However, our results are closer to reality compared to the results from *Timmermann et al.* [2012].

Although there are some differences between our model results and observations, we are able to reproduce warm CDW intrusions and basal melting of ice shelves in the AS and BS. Thus, we refer to this as the CTRL case.

3.2. Spreading of the basal melt water from West Antarctic ice shelves

After 10 years of simulation, about 70% of the basal melt water from the BS flows westward, while the rest flows northeastward (east of 70°W) along the path of the ACC (Fig. 2a). For the basal melt water from the BS, 16% reaches the AS (west of 100°W), and only 2% reaches the RS (west of 134°W). On the other hand, basal melt water from the AS mostly flows westward with 36% reaching the RS (Fig. 2b). Investigating the four largest sources, the basal melt water from the George VI Ice Shelf spreads both eastward and westward (not shown), but is very similar to Fig 2a. The melt water from the Abbot and Pine Island Ice Shelves flows westward, but only 20% and 25% reaches the RS, respectively (Figs. 3a and b). The melt water from the Getz Ice Shelf flows westwards and more than 50% influences the RS (Fig. 3c). For the amount of basal melt water from the AS and BS in the RS (160°E-134°W), 95% (5%) originates from the AS (BS). The basal melt water in the RS originating from the AS consists of 58% from the Getz, 8% from the Pine Island, and 11% from the Abbot Ice Shelves, respectively. This confirms the importance of the Getz Ice Shelf for the melt water transport into the RS, as also suggested by *Jacobs et al.* [2013]. However, we note that the contributions of Pine Island Ice Shelf and Thwaites Glacier may be underestimated in our model, because the simulated basal mass losses are too small for these ice shelves.

In contrast, *Kusahara and Hasumi* [2014], who investigated the spreading of melt water from all Antarctic ice shelves, show that most of the basal melt water originating from the AS and BS flows eastward along the path of the ACC. However, since their focus was rather on East Antarctica with coarser resolution in the AS and BS (∼20 km), CDW intrusions and ice shelf basal melting in these regions are not well reproduced [*Kusahara and Hasumi*, 2013]. This might explain the different pathways of melt water.

3.3. Sensitivity of melt water transport into the Ross Sea

We also investigate the sensitivity of basal melt water transport into the RS associated with the strength of the basal mass loss. In these sensitivity experiments, we increase the basal melt water flux by a factor k_m, so that

$$F_w = k_m M_{melt}, \tag{1}$$

where M_{melt} is the melt rate obtained from the fluxes of heat and salt at the ice shelf base and F_w is the melt water flux applied to the model ocean at the ice-ocean interface. For the CTRL case, obviously, $k_m = 1$. For the two sensitivity experiments 1.3×Melt and

2.0×Melt, we set $k_m = 1.3$ and $k_m = 2.0$, respectively, for all ice shelves in West Antarctica (in the region 140-65°W). In our simulation we assume that M_{melt} is proportional to $(T_{in} - T_f)$, where T_{in} and T_f are in-situ temperature and in-situ freezing point temperature, respectively. Thus, one can associate the increase of k_m with an increase of CDW temperature reaching the ice shelf base. For instance, the case $k_m = 1.3(2.0)$ mimics the situation with CDW temperature 30% (100%) warmer than simulated in the CTRL case. The CDW temperature is ~ 0.5°C at the Pine Island Ice Shelf front for the CTRL case, and the 1.3×MELT (2.0×MELT) case mimics the situation with a CDW temperature of 1.2 (2.8) °C. We note that inflowing CDW temperatures are simulated lower than observations at some of the ice shelf fronts (e.g., observed CDW temperature is ~ 1.1°C at the Pine Island Ice Shelf front). Therefore, the 1.3×MELT case may reproduce the situation closer to reality for some AS ice shelves. The total basal mass loss of the AS and BS ice shelves for the 1.3×MELT case are comparable to the maximum of the observation-based estimates (Supplementary Table S1).

In the 1.3×MELT and 2.0×MELT cases, more basal melt water is transported into the RS (Fig. 4), and vertically integrated melt water content is 4-5 times larger in the 2.0×MELT case than in the CTRL case at the Ross Ice Shelf front, increasing non-linearly (Fig. 4). For the 1.3×MELT and 2.0×MELT cases, the melt water transport quickly increases after the basal mass loss increases. The total amount of basal melt water transported into the RS is 1.8 (4.9) times more than in the CTRL case by volume after 10 years of simulation (Supplementary Table S3), although k_m is set to only 1.3 (2.0) in the 1.3×MELT (2.0×MELT) case. This leads to a freshening of 0.1 and 0.4, respectively, at the eastern side of the Ross Ice Shelf front after 10 years of simulation. This indicates that basal melt water release significantly influences the dynamics of shelf circulation and the transport of basal melt water into the RS.

If CDW properties intruding into the ice shelf cavities would remain similar to the CTRL case, the basal mass loss of the 1.3×MELT and 2.0×MELT cases should be $\sim$ 1.3 and 2.0 times larger than in the CTRL case, respectively. However, the total combined basal mass loss of AS and BS ice shelves becomes 1.6 and 4.0 times larger for the 1.3×MELT and 2.0×MELT cases than for the CTRL case, correspondingly (Supplementary Table. S1). When bottom potential temperatures of the three cases are compared, ice front bottom temperatures are increasing in most of the regions of the AS (the lower right panels of Fig. 4) and BS (not shown), and the Pine Island Ice Shelf front temperature increases by nearly 0.3 °C for the 2.0×MELT case. This is most likely caused by a strengthening of the shelf circulation and a freshening of the surface waters. The strengthening of the shelf circulation makes CDW intrusions stronger. For example, annual mean velocities at a depth of 500 m along the pathway of the CDW intrusion from the eastern and central submarine glacial troughs (see Fig. 6 in *Nakayama et al.* [2014]) both become $\sim$1.5 times and more than 2 times faster for the 1.3×MELT and 2.0×MELT cases, respectively. In addition, the freshening of the surface waters weakens the strength of vertical mixing, allowing for a warmer CDW to reach the sub-ice shelf cavities. At the Pine Island Ice Shelf front, mixed layer depth becomes $\sim$ 50 m and 150 m shallower in winter for the 1.3×MELT and 2.0×MELT cases, respectively.

As already mentioned, the total basal melt water transport into the RS becomes 1.8 and 4.9 times larger for the 1.3×MELT and 2.0×MELT cases than in the CTRL case, respectively. This cannot be simply explained by the increase of the basal mass loss alone. Instead, we consider this to be a result of the strengthening of the westward flowing coastal current due to a stronger density gradient (caused by lower shelf salinity) produced by stronger basal melting. For the coastal current crossing 155°W, the mean (averaged for the last five years of model simulation) potential densities at a depth of 100 m are 27.3, 27.2, and 27.0 kg m^{-3}, and mean westward velocities are 0.03, 0.04, 0.08 m s^{-1} for the CTRL, 1.3×MELT, and 2.0×MELT cases, respectively, confirming the strengthening of coastal current.

Our sensitivity experiments, thus, reveal that a slight increase of the basal mass loss (by warming of inflowing CDW temperature) rapidly intensifies the basal melt water transport into the RS. The mechanism, which represents a positive feedback, can be summarized as follows. In response to an increase of basal mass loss, the shelf circulation becomes stronger and mixed layer depth becomes shallower due to the surface freshening, leading to the strengthening and warming of CDW intrusions, which again increases the basal mass loss. Further, the larger input of basal melt water increases the density contrast at the continental shelf break and thus intensifies the coastal current, leading to a more efficient transport of basal melt water into the RS.

4. Discussion

Based on the time series of averaged shelf water salinity observed in McMurdo Sound and north of Ross Island (Fig. 3 in *Jacobs and Giulivi* [2010]), salinity remains at ∼34.85

between 1958-1968, but decreases to ∼34.80 for the period 1977-1984. The salinity decreases at a rate of ∼0.03 decade $^{-1}$ for 1958-2008 [*Jacobs and Giulivi*, 2010]. A freshening of the 600-m deep RS continental shelf by 0.05, assuming a mean salinity of 34.8, corresponds to a vertically integrated melt water content increase of ∼1 m. Based on our sensitivity experiments, the change of the vertically integrated melt water content between the CTRL and 1.3×MELT cases is ∼1 m, which is comparable to the magnitude of the freshening observed on the RS continental shelf. In addition, the integrated melt water contents in the Ross Sea originating from ice shelves in the AS and BS are 1.1×10^3 km^3 and 2.0×10^3 km^3 for the CTRL and 1.3×MELT cases, respectively, after 10 years of simulation (Supplementary Table S3). Thus, the change of the integrated melt water content in the Ross Sea between the CTRL and 1.3×MELT cases is 900 km^3. On the other hand, *Comiso et al.* [2011] estimate about 20 km^3 of increased sea-ice volume transport out of the Ross Sea every year, leading to a freshwater decrease of 200 km^3 in 10 years. Thus, the increment of freshwater due to basal melting between the CTRL and 1.3×MELT cases is about 5 times larger than the estimate of increased freshwater export from *Comiso et al.* [2011].

We note that the transport of basal melt water rapidly increases (in less than 10 years) in response to an increased basal melting in the AS and BS. Thus, considering that mass loss rates of AS and BS ice shelves increased by about 60% between 1996 and 2006 [*Rignot et al.*, 2008], the recent freshening observed on the RS continental shelf may be explained by the positive feedback mechanism proposed in this study. Although no data is available for basal mass loss of AS and BS ice shelves from the 1960s to the 1980s, it is plausible to assume that the earlier RS freshening may go back to the same mechanism. This, in turn, implies that the basal mass loss of the AS ice shelves would have already increased from the 1960s.

5. Summary

It has been suggested that an increased melting of continental ice in the AS and BS is the likely source of the RS freshening [*Jacobs et al.*, 2002; *Jacobs and Giulivi*, 2010]. So far, this hypothesis could not be assessed using numerical models, because it has been difficult to reproduce warm CDW intrusions onto the AS and BS continental shelves in circumpolar or global models. In this study, we reproduce the warm CDW intrusions onto the AS and BS continental shelves and, thus are able to investigate the spreading of the melt water of AS and BS ice shelves in the Southern Ocean.

Using virtual passive tracers indicating the ice shelf melt water fraction per unit ocean volume, we find that basal melt water from the BS mostly flows westward, towards the AS, but only a small fraction reaches the RS after 10 years of simulation. On the other hand, more than one third of basal melt water from the AS ice shelves reaches the RS with more than half of the melt water originating from the Getz Ice Shelf in our simulation. Our results confirm that the basal melting of the ice shelves in the AS could be the reason for the observed RS freshening. Further, our results reveal that a slight increase of the basal mass loss (by warming of the inflowing CDW) can substantially intensify the transport of basal melt water into the RS as a result of the strengthening of the shelf circulation, the weakening of deep convection due to a freshening of the surface waters, and the acceleration of buoyancy driven coastal current.

Although this study provides one possible explanation for the RS freshening, basal melting of ice shelves is strongly influenced by many factors such as large-scale atmospheric and ocean circulation (which determine the strength and pathway of CDW intrusions), cavity shape, local sea-ice formation, issues remaining with continental shelf CDW properties, and basal melting parametrization. Due to the complexity of these processes, our sensitivity experiments, using a uniform increase of the basal mass loss for all the West Antarctic ice shelves, could be too simple. Therefore, further investigation into the reasons for the RS freshening and of the interaction between the different sectors of the Southern Ocean seems necessary.

Acknowledgments. We thank Dmitry Sidorenko, and Qiang Wang for their help and support and Shigeru Aoki, Karen M. Assmann, Sergey Danilov, Pierre Dutrieux, Paul Holland, Adrian Jenkins, and Kazuya Kusahara for their useful comments and suggestions. The model code, processing tools, and raw model output are difficult to make publicly available, and the authors recommend contacting the corresponding author for those interested in accessing the data. Insightful comments from two anonymous reviewers were very helpful for the improvement of the manuscript.

References

Assmann, K., A. Jenkins, D. Shoosmith, D. Walker, S. Jacobs, and K. Nicholls (2013), Variability of circumpolar deep water transport onto the Amundsen Sea continental shelf through a shelf break trough, *J. Geophys. Res.*, *118*(12), 6603–6620.

Cavalieri, D., C. Parkinson, P. Gloersen, and H. Zwally (2006), Sea ice concentrations from Nimbus-7 SMMR and DMSP SSM/I passive microwave data, January 1979-June 2006.

Comiso, J. C., R. Kwok, S. Martin, and A. L. Gordon (2011), Variability and trends in sea ice extent and ice production in the ross sea, *J. Geophys. Res.*, *116*(C4).

Conkright, M., J. Antonov, O. Baranova, T. Boyer, H. Garcia, R. Gelfeld, D. Johnson, R. Locarnini, T. O'Brien, I. Smolyar, et al. (2002), World Ocean Database 2001, Volume 1. Introduction, ed. by S. Levitus, NOAA Atlas NESDIS 42, *US Government Printing Office, Washington, DC.*

Corr, H. F., A. Jenkins, K. W. Nicholls, and C. Doake (2002), Precise measurement of changes in ice-shelf thickness by phase-sensitive radar to determine basal melt rates, *Geophys. Res. Lett.*, *29*(8), 73–1.

Depoorter, M., J. Bamber, J. Griggs, J. Lenaerts, S. Ligtenberg, M. van den Broeke, and G. Moholdt (2013), Calving fluxes and basal melt rates of Antarctic ice shelves, *Nature*, *502*(7469), 89–92.

Dutrieux, P., J. De Rydt, A. Jenkins, P. R. Holland, H. K. Ha, S. H. Lee, E. J. Steig, Q. Ding, E. P. Abrahamsen, and M. Schröder (2014), Strong sensitivity of Pine Island ice-shelf melting to climatic variability, *Science*, *343*(6167), 174–178.

Hellmer, H., and D. Olbers (1989), A two-dimensional model for the thermohaline circulation under an ice shelf, *Antarctic Science*, *1*(04), 325–336.

Holland, D. M., and A. Jenkins (1999), Modeling thermodynamic ice-ocean interactions at the base of an ice shelf, *J. Phys. Oceanogr.*, *29*(8), 1787–1800.

Jacobs, S., C. Giulivi, P. Dutrieux, E. Rignot, F. Nitsche, and J. Mouginot (2013), Getz Ice Shelf melting response to changes in ocean forcing, *J. Geophys. Res.*, *118*(9), 4152–4168.

Jacobs, S. S., and C. F. Giulivi (2010), Large multidecadal salinity trends near the Pacific-Antarctic continental margin, *J. Clim.*, *23*(17), 4508–4524.

Jacobs, S. S., C. F. Giulivi, and P. A. Mele (2002), Freshening of the Ross Sea during the late 20th century, *Science*, *297*(5580), 386–389.

Jacobs, S. S., A. Jenkins, C. F. Giulivi, and P. Dutrieux (2011), Stronger ocean circulation and increased melting under Pine Island Glacier ice shelf, *Nat. Geosci.*, *4*(8), 519–523.

Jenkins, A. (1991), A one-dimensional model of ice shelf-ocean interaction, *J. Geophys. Res.*, *96*(C11), 20,671–20,677.

Jenkins, A., and S. Jacobs (2008), Circulation and melting beneath George VI ice shelf, Antarctica, *J. Geophys. Res*, *113*, C04,013.

Kusahara, K., and H. Hasumi (2013), Modeling Antarctic ice shelf responses to future climate changes and impacts on the ocean, *J. Geophys. Res.*, *118*(5), 2454–2475.

Kusahara, K., and H. Hasumi (2014), Pathways of basal meltwater from Antarctic ice shelves: A model study, *J. Geophys. Res. Lett.*, *119*(9), 5690–5704.

Nakayama, Y., M. Schröder, and H. H. Hellmer (2013), From circumpolar deep water to the glacial meltwater plume on the eastern Amundsen Shelf, *Deep Sea Res. I*, *77*, 50–62.

Nakayama, Y., R. Timmermann, M. Schröder, and H. H. Hellmer (2014), On the difficulty of modeling Circumpolar Deep Water intrusions onto the Amundsen Sea continental shelf, *Ocean Model. 84*, 26–34.

Potter, J., J. Paren, and J. Loynes (1984), Glaciological and oceanographic calculations of the mass balance and oxygen isotope ratio of a melting ice shelf, *J. Glaciol.*, *30*(105), 161–170.

Pritchard, H. D., S. R. M. Ligtenberg, H. A. Fricker, D. G. Vaughan, M. R. Van den Broeke, and L. Padman (2012), Antarctic ice-sheet loss driven by basal melting of ice shelves, *Nature*, *484*(7395), 502–505.

Rignot, E., J. L. Bamber, M. R. V. den Broeke, C. Davis, Y. Li, W. J. V. de Berg, and E. V. Meijgaard (2008), Recent Antarctic ice mass loss from radar interferometry and regional climate modelling, *Nat. Geosci.*, *1*(2), 106–110.

Rignot, E., S. S. Jacobs, J. Mouginot, and B. Scheuchl (2013), Ice-shelf melting around Antarctica, *Science Express*, *341*, 226–270.

Rintoul, S. R. (2007), Rapid freshening of Antarctic Bottom Water formed in the Indian and Pacific oceans, *Geophys. Res. Lett.*, *34*(6), L06,606.

Rodehacke, C. B., H. H. Hellmer, O. Huhn, and A. Beckmann (2007), Ocean/ice shelf interaction in the southern weddell sea: results of a regional numerical helium/neon simulation, *Ocean dynamics*, *57*(1), 1–11.

Saha, S., S. Moorthi, H.-L. Pan, X. Wu, J. Wang, S. Nadiga, P. Tripp, R. Kistler, J. Woollen, D. Behringer, et al. (2010), The NCEP climate forecast system reanalysis, *Bull. Am. Meteorol. Soc.*, *91*(8), 1015–1057.

Schodlok, M. P., D. Menemenlis, E. Rignot, and M. Studinger (2012), Sensitivity of the ice shelf ocean system to the sub-ice shelf cavity shape measured by NASA IceBridge in Pine Island Glacier, West Antarctica, *Ann. Glaciol.*, *53*, 156–162.

Shepherd, A., E. Ivins, A. Geruo, V. Barletta, M. Bentley, S. Bettadpur, K. Briggs, D. Bromwich, R. Forsberg, N. Galin, et al. (2012), A reconciled estimate of ice-sheet mass balance, *Science*, *338*(6111), 1183–1189.

Timmermann, R., and H. H. Hellmer (2013), Southern Ocean warming and increased ice shelf basal melting in the twenty-first and twenty-second centuries based on coupled ice-ocean finite-element modelling, *Ocean Dynamics*, *63*(9-10), 1011–1026.

Timmermann, R., S. Danilov, J. Schröter, C. Böning, D. Sidorenko, and K. Rollenhagen (2009), Ocean circulation and sea ice distribution in a finite element global sea ice–ocean model, *Ocean Model.*, *27*(3), 114–129.

Timmermann, R., A. L. Brocq, T. Deen, E. Domack, P. Dutrieux, B. Galton-Fenzi, H. Hellmer, A. Humbert, D. Jansen, A. Jenkins, et al. (2010), A consistent data set of Antarctic ice sheet topography, cavity geometry, and global bathymetry, *Earth System Science Data*, *2*(2), 261–273.

Timmermann, R., Q. Wang, and H. Hellmer (2012), Ice-shelf basal melting in a global finite-element sea-ice/ice-shelf/ocean model, *Ann. Glaciol.*, *53*(60), 303–314.

Walker, D. P., A. Jenkins, K. M. Assmann, D. R. Shoosmith, and M. A. Brandon (2013), Oceanographic observations at the shelf break of the Amundsen Sea, Antarctica, *J. Geophys. Res.*, *118*(6), 2906–2918.

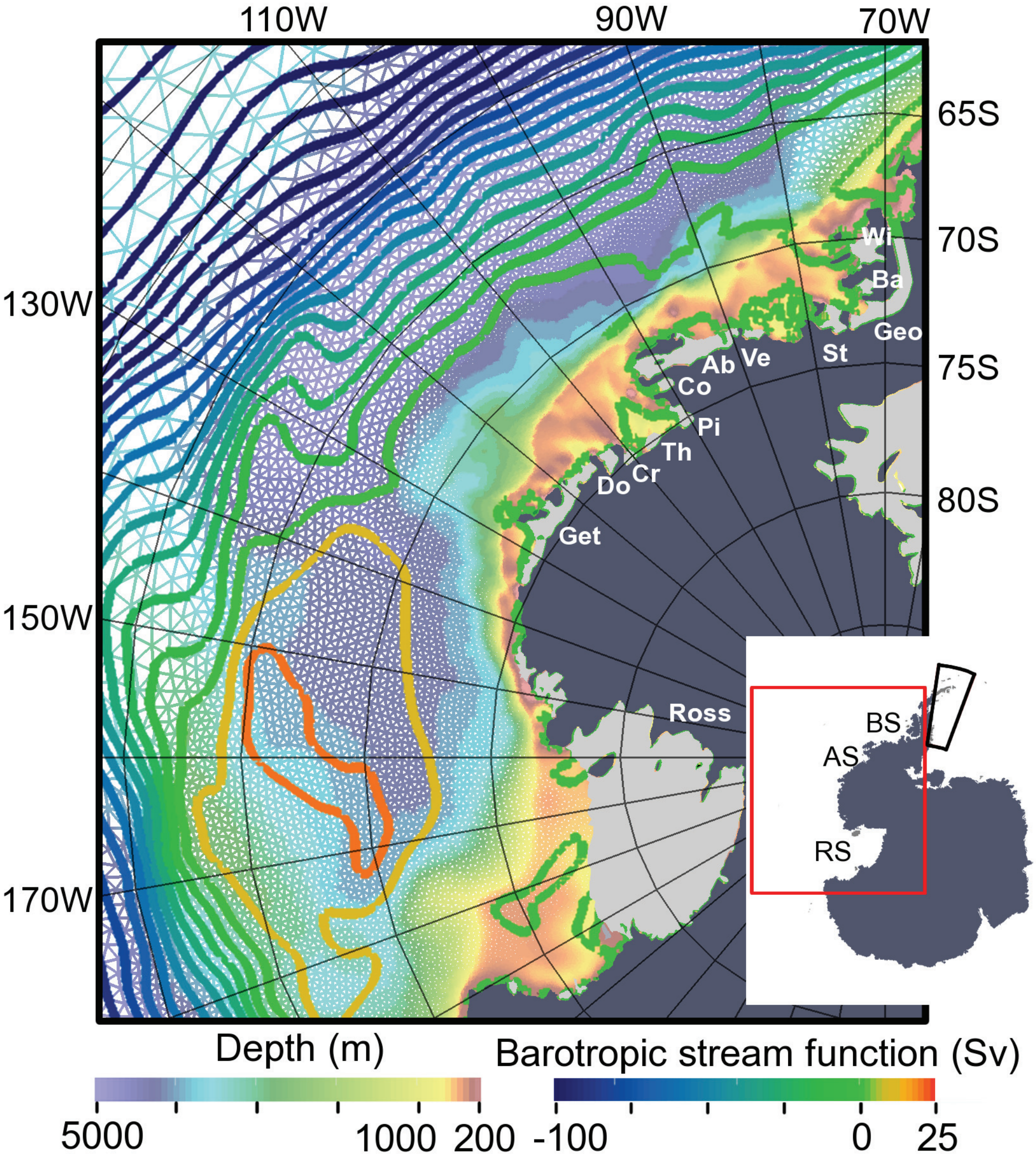

Figure 1. Horizontal grid of the AS, BS, and RS regions of the global model with the depth of the model bathymetry (color) and simulated mean barotropic stream function in the CTRL case (thick contours with contour interval of 10 Sv). The inset (right bottom) shows Antarctica with regions surrounded by red and black lines denoting the location of the enlarged portion and the location where temperature and salinity are restored (black box), respectively. Locations of ice shelves are shown with acronyms that are summarized in Supplementary Table S1.

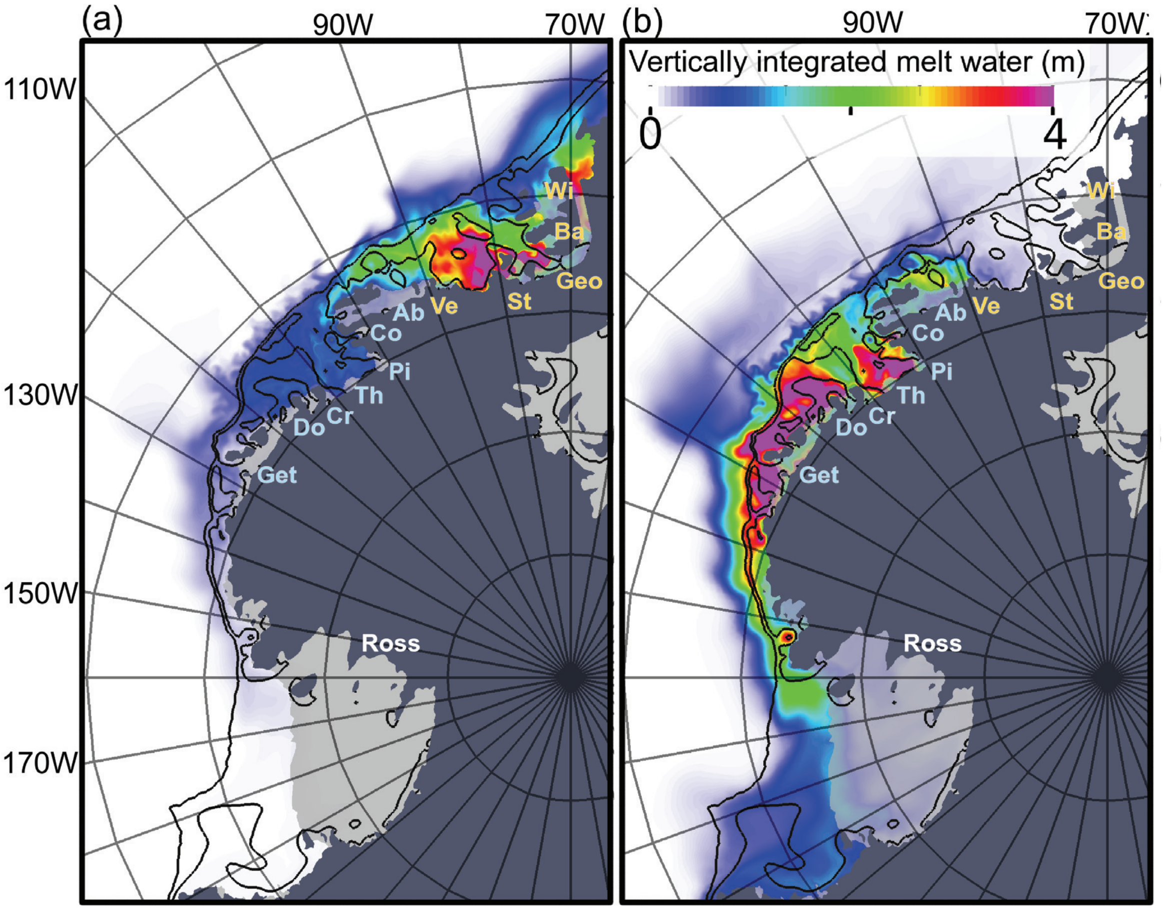

Figure 2. Spatial distributions of vertically integrated melt water content after 10 years of simulation showing the basal melt water from (a) ice shelves in the BS (names in light yellow) and (b) ice shelves in the AS (names in light blue). The bathymetry contours of 500 and 1000 m are shown (black lines). Locations of ice shelves are indicated by acronyms that are summarized in Supplementary Table S1.

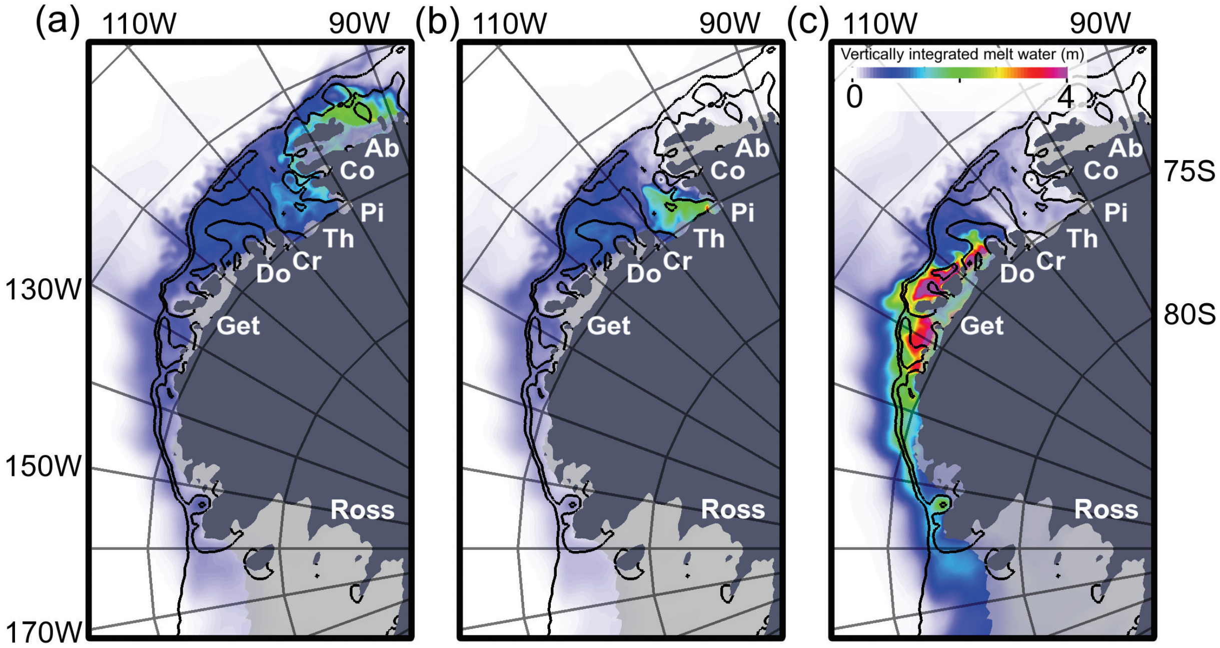

Figure 3. Same as Fig. 2 but showing the spatial distributions of the basal melt water from (a) Abbot Ice Shelf, (b) Pine Island Ice Shelf, and (c) Getz Ice Shelf after 10 years of simulation.

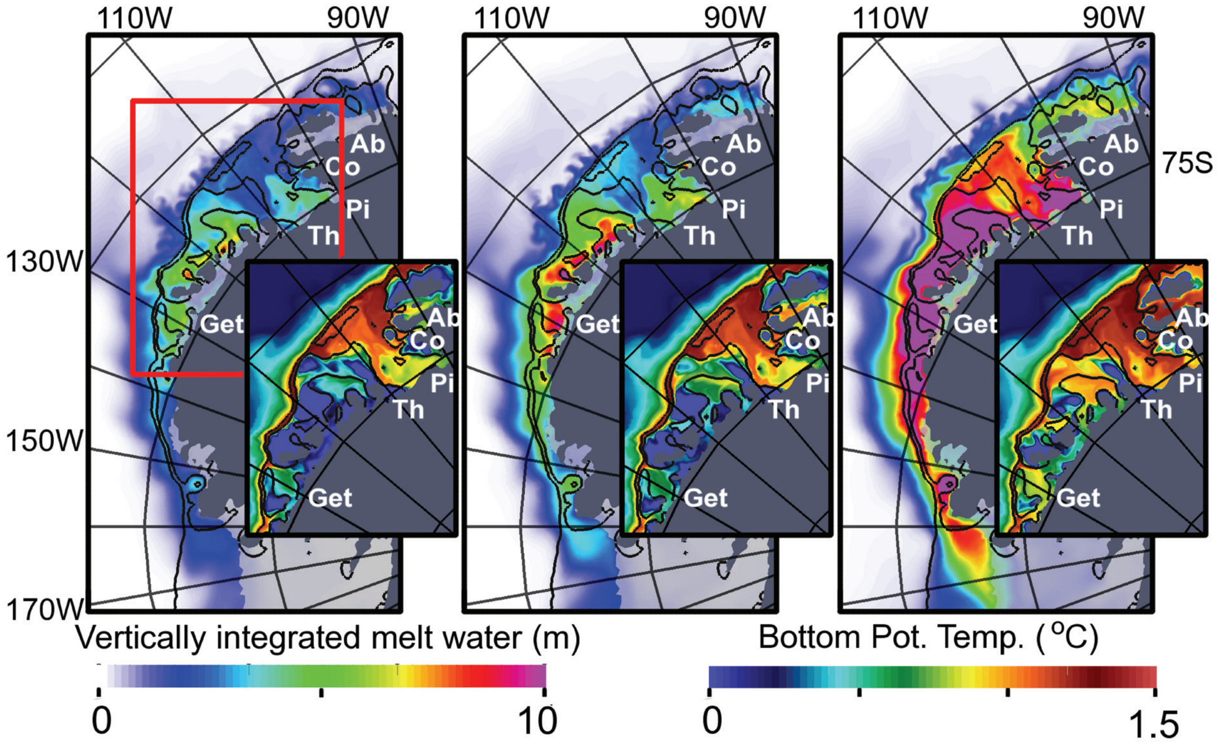

Figure 4. Same as Fig. 2 but showing the spatial distributions of the basal melt water from ice shelves in the AS only for the (a) CTRL (different scale from Fig. 2), (b) 1.3×MELT, and (c) 2.0×MELT cases. The lower-right panels show the bottom potential temperature of the region enclosed by the red line in (a).

Supporting information for
Modeling the spreading of glacial melt water from the Amundsen and Bellingshausen Seas

Yoshihiro Nakayama[1], Ralph Timmermann[1], Christian. B. Rodehacke[2], Michael Schröder[1], Hartmut H. Hellmer[1]

1 Alfred Wegener Institute, Bremerhaven, Germany
2 Danish Meteorological Institute Copenhagen, Denmark
Geophysical Research Letters, 2014

Introduction

The supplementary information for this manuscript contains three tables. Table S1 summarizes the Area, modeled annual-mean basal mass loss, and melt rate of the West Antarctic ice shelves from FESOM (10 year average) for the CTRL, 1.3×MELT, and 2.0×MELT cases together with observation-based estimates. Table S2 summarizes the observation-based estimates of annual-mean basal mass loss and melt rate. Table S3 summarizes the integrated melt water contents in the Ross Sea originating from ice shelves in the AS and BS after 10 years of simulation for the CTRL, 1.3×MELT, and 2.0×MELT cases, respectively.

Table S1. Characteristics of the West Antarctic ice shelves from FESOM (10 year average) for the CTRL, 1.3×MELT, and 2.0×MELT cases and other observation-based estimates summarized in Table S1. Area, modeled annual-mean basal mass loss (Gt yr^{-1}, bold), and melt rate (m yr^{-1}, bracket) are shown. Areas in the left column are derived from RTopo-1 (*Timmermann et al.*, 2010). Acronyms of ice shelves used in the figures are shown in brackets.

Name	Area km^2	CTRL Gt/yr (m/yr)	1.3×MELT Gt/yr	2.0×MELT Gt/yr	Observation-based estimate Gt/yr
George VI (Geo)	27×10^3	**100** (3.6)	**163**	**345**	**53-119**
Wilkins (Wi)	13×10^3	**25** (1.9)	**35**	**86**	**1-35**
Bach (Ba)	3.1×10^3	**5** (1.7)	**9**	**23**	**9-11**
Stange (St)	6.8×10^3	**22** (3.2)	**37**	**96**	**22-34**
Venable (Ve)	2.7×10^3	**10** (3.7)	**15**	**32**	**12-21**
Bellingshausen Sea total	53×10^3	**162** (3.1)	**259**	**582**	**97-220**
Abbot (Ab)	30×10^3	**50** (1.7)	**77**	**206**	**33-97**
Cosgrove (Co)	2.1×10^3	**12** (5.7)	**21**	**59**	**7-14**
Pine Island (PI)	4.7×10^3	**34** (7.2)	**52**	**121**	**38-114**
Thwaites (Th)	3.5×10^3	**27** (7.7)	**43**	**99**	**51-105**
Crosson (Cr)	2.0×10^3	**3** (1.7)	**5**	**14**	**35-43**
Doston (Do)	4.4×10^3	**20** (4.5)	**37**	**101**	**41-49**
Getz (Get)	33×10^3	**116** (3.5)	**203**	**528**	**36-165**
Amundsen Sea total	80×10^3	**262** (3.3)	**438**	**1128**	**241-587**

Table S2. Summary of observation-based estimates of annual-mean basal mass loss (Gt yr^{-1}, bold) and melt rates (m yr^{-1}). In the Method column, G, O, and S stands for glaciological estimate, oceanographic estimate, and satellite estimate, respectively. Difference in the individual estimates might be related to diverging reference periods. Note that ice shelf areas used for conversion between mass losses and melt rates are not identical for the various studies.

Ice Shelf	Reference	Mass loss **(Gt yr^{-1})**	Melt rate (m yr^{-1})	Method
George VI	*Potter et al.* [1984]	**53**	2.1	G, O
	Corr et al. [2002]	**64**	2.7-2.9	G, Radar
	Jenkins and Jacobs [2008]	**78-119**	3-5	O
	Rignot et al. [2013]	**72-106**	3.1-4.5	S
Wilkins	*Rignot et al.* [2013]	**1-35**	0.5-2.5	S
Bach	*Rignot et al.* [2013]	**9-11**	2.0-2.6	S
Stange	*Rignot et al.* [2013]	**22-34**	2.8-4.2	S
Venable	*Depoorter et al.* [2013]	**12-18**	3.9-5.8	S
	Rignot et al. [2013]	**17-21**	5.4-6.8	S
Abbot	*Depoorter et al.* [2013]	**75-97**	2.0-3.4	S
	Rignot et al. [2013]	**33-71**	1.1-2.3	S
Cosgrove	*Depoorter et al.* [2013]	**8-14**	2.9-4.6	S
	Rignot et al. [2013]	**7-11**	2.1-3.5	S
Pine Island	*Jacobs et al.* [2011]	**53-85**	22-33	O
	Depoorter et al. [2013]	**81-109**	14-18	S
	Nakayama et al. [2013]	**74**	29	O
	Rignot et al. [2013]	**93-109**	15.2-17.2	S
	Dutrieux et al. [2014]	**38-114**	8-24	O
Thwaites	*Depoorter et al.* [2013]	**51-87**	11-19	S
	Rignot et al. [2013]	**91-105**	16.7-18.7	S
Crosson	*Rignot et al.* [2013]	**35-43**	11-13	S
Dotson	*Rignot et al.* [2013]	**41-49**	7-8	S
Getz	*Depoorter et al.* [2013]	**117-155**	4-5	S
	Jacobs et al. [2013]	**36-135**	1-4	S
	Rignot et al. [2013]	**135-165**	4-5	S

Table S3. Integrated melt water contents in the Ross Sea (defined as the region east of 140°E, south of 60°S, and west of 134°W) originating from ice shelves in the AS and BS after 10 years of simulation for the CTRL, 1.3×MELT, and 2.0×MELT cases, respectively.

	CTRL (10^3 km^3)	1.3×MELT (10^3 km^3)	2.0× MELT (10^3 km^3)
Melt water content from BS	0.05	0.15	0.83
Melt water content from AS	1.06	1.85	4.57
Total melt water content	1.11	2.00	5.40

6 Summary and Outlook

Jacobs et al. (2002) and *Jacobs and Giulivi* (2010) show that salinity of shelf water in the southwestern Ross Sea (RS) has declined by 0.03 per decade over last 50 years. Based on oceanographic observations, they suggest that the observed freshening may be related to the increased ice shelf melting upstream in the Amundsen Sea (AS). Thus, the objective of this doctoral thesis is to understand the supply of heat from the deep ocean to the ice shelves fringing the Amundsen Sea and to simulate the spreading of glacial melt water in the Southeast Pacific sector of the Southern Ocean. The Finite-Element Sea-ice/ice-shelf/Ocean Model (FESOM, *Timmermann et al.* (2012)) is used as the modeling tool. This study is important for assessing the impact of the West Antarctic Ice Sheet (WAIS) on the global ocean during climate change, because glacial melt water input to the ocean could lead to a change in the water mass characteristics in the AS and downstream in the RS, which may weaken the production of Antarctic Bottom Water (AABW) and, thus, the global thermohaline circulation. For this purpose, I conducted the following three studies.

First, the analysis of the hydrographic data of Polarstern cruise ANTXXVI/3 covering the whole eastern AS continental shelf reveals that:

- A thicker and warmer intrusion of Circumpolar Deep Water (CDW) (∼300 m, warmer than 1.23 °C) and a thinner and colder CDW intrusion (<100 m and colder than 1.23 °C) are observed at the eastern and central troughs, respectively. These intrusions represent the main heat source for melting the fringing ice shelves.
- The ratio between contributions of the eastern and central CDW intrusions towards PIIS is estimated to be roughly 1:1.5 below the 27.78-isopycnal, respectively, assuming that CDW from the eastern and central troughs mixes isopycnally and flows towards PIIS.

- Pine Island Ice Shelf (PIIS) melt rate in 2010 is estimated to be ∼30 m yr $^{-1}$ using PIIS front CTD profiles. This is close to the highest melt rate observed in 2009 (*Jacobs et al.*, 2011).
- Glacial melt water spreads towards the west following the bathymetry, based on the horizontal distribution of the glacial melt water fraction estimated from potential temperature, salinity, and dissolved oxygen.

This study provides valuable information on CDW intrusions, PIIS melting, and spreading of glacial melt water.

A suite of sensitivity experiments, designed to investigate the representation of CDW intrusions in the model, reveals that:

- A horizontal resolution of about 5 km or smaller (about the length scale of the Rossby deformation radius) over the continental shelves of the AS and Bellingshausen Sea (BS) is required to simulate CDW intrusions realistically.
- A cold bias in the NCEP/NCAR reanalysis data (*Assmann and Timmermann*, 2005) tends to erode simulated CDW on the continental shelf due to a spurious deepening of the cold surface mixed layer. This leads to the cooling of PIIS front bottom temperature to ∼0° C, while temperatures of ∼ 1°C are typical at this location in reality.

With a fine horizontal resolution (∼2.5 km in the eastern AS) and NCEP-CFSR forcing, FESOM is able to reproduce CDW intrusions onto the AS and BS continental shelf with PIIS front bottom temperature of ∼0.5°C and basal melt rates of AS and BS ice shelves much closer to the reality.

Finally, the main findings of the simulation of the spreading of glacial melt from AS and BS ice shelves in the Southeast Pacific sector of the Southern Ocean using FESOM are :

- More than one third of basal melt water from the AS ice shelves reaches the RS with more than half of the total melt water originating from the Getz Ice Shelf.

- The model results suggest a positive feedback mechanism: A slight increase of the basal mass loss can substantially intensify the transport of melt water into the RS due to a strengthening of the melt-driven shelf circulation and the westward flowing coastal current. Total melt water transport into the Ross Sea therefore increases more than just by the amount of additional melt water input.

- The observed freshening of the RS in the late 1970s/early 1980s, prior to the remotely sensed increase in ice shelf mass losses, might have been caused by enhanced basal melting already in the 1960s.

The proposed positive feedback mechanism could be critical for the global climate, because further acceleration of WAIS melting might freshen the RS even faster and possibly weaken the production of AABW and the thermohaline circulation. Considering the fact that the ocean around Antarctica is estimated to have warmed at a rate of 0.068°C per decade at depths between 300 and 1000 meters from 1960–2000 (*Böning et al.*, 2008) and that the Southern Annular Mode (SAM) is trending toward a positive phase that is expected to bring more warm water close to the continental shelf, the ocean may provide even more favorable conditions for basal ice shelf melting.

A detailed analysis of the impact of the WAIS in a warmer climate requires accurate future projections of the evolution of the WAIS, which, however, seems to be difficult. Two recent studies based on satellite data and oceanographic observations display conflicting future projections of PIIS. *Rignot et al.* (2014) show that the PIIS grounding line retreated 31 km between 2005 and 2009 and that this may be the onset of an irreversible retreat for the next few centuries as a result of marine ice sheet instability. On the other hand, *Dutrieux et al.* (2014) and *De Rydt et al.* (2014) point out that the ridge in front of the grounding line of PIIS (shown by the white arrow in Fig. 1.1b) largely controls the basal melting of PIIS. They show that the PIIS melt rate decreased by 50% in summer 2012 because of a deeper thermocline (i.e. less warm water intruding into the PIIS cavity), which potentially permits a readvance of the grounding line, if the deep thermocline persists for years. Furthermore, there are several ice sheet models projecting the evolution of PIIS, but their results show different future evolutions

(*Favier et al.*, 2014; *Seroussi et al.*, 2014) . Thus, there seems to be a long way to go before ice sheet and ocean models as well as satellite and oceanographic observations acquire significant predictive skill for the future evolution of PIIS and thus the WAIS. Continuous data acquisition and a further development of the numerical models seem necessary for the understanding of the impact of WAIS on the global ocean in a changing climate.

References

Assmann, K. M., and R. Timmermann (2005), Variability of dense water formation in the Ross Sea, *Ocean Dynamics*, *55*(2), 68–87.

Bamber, J. L., R. E. M. Riva, B. L. A. Vermeersen, and A. M. LeBrocq (2009), Reassessment of the potential sea-level rise from a collapse of the West Antarctic Ice Sheet, *Science*, *324*(5929), 901–903.

Böning, C. W., A. Dispert, M. Visbeck, S. Rintoul, and F. U. Schwarzkopf (2008), The response of the Antarctic Circumpolar Current to recent climate change, *Nat. Geosci.*, *1*(12), 864–869.

Church, J. A., and N. J. White (2011), Sea-level rise from the late 19th to the early 21st century, *Surveys in Geophysics*, *32*(4-5), 585–602.

De Rydt, J., P. Holland, P. Dutrieux, and A. Jenkins (2014), Geometric and oceanographic controls on melting beneath Pine Island Glacier, *J. Geophys. Res.*, *119*(4), 2420–2438.

Dutrieux, P., J. De Rydt, A. Jenkins, P. R. Holland, H. K. Ha, S. H. Lee, E. J. Steig, Q. Ding, E. P. Abrahamsen, and M. Schröder (2014), Strong sensitivity of pine island ice-shelf melting to climatic variability, *Science*, *343*(6167), 174–178.

Favier, L., G. Durand, S. Cornford, G. Gudmundsson, O. Gagliardini, F. Gillet-Chaulet, T. Zwinger, A. Payne, and A. Le Brocq (2014), Retreat of Pine Island Glacier controlled by marine ice-sheet instability, *Nat. Clim. Change*, *4*, 117–121.

Fischer, H. (1995), Vergleichende Untersuchungen eines optimierten dynamisch-thermodynamischen Meereismodells mit Beobachtungen im Weddellmeer, *Berichte zur Polarforschung 166*, alfred-Wegener-Institut, Bremerhaven.

Foldvik, A., and T. Kvinge (1974), Conditional instability of sea water at the freezing point, in *Deep Sea Research and Oceanographic Abstracts*, vol. 21, pp. 169–174, Elsevier.

Gohl, K. (2010), The Expedition of the Research Vessel Polarstern to the Amundsen Sea, Antarctica, in 2010 (ANT-XXIV/3), *Reports on Polar and Marine Research*, *617*, 173.

Hellmer, H., and D. Olbers (1989), A two-dimensional model for the thermohaline circulation under an ice shelf, *Antarctic Science*, *1*(04), 325–336.

Hohmann, R., P. Schlosser, S. Jacobs, A. Ludin, and R. Weppernig (2002), Excess helium and neon in the southeast Pacific: Tracers for glacial meltwater, *J. Geophys. Res.*, *107*(C11), 3198.

Holland, D. M., and A. Jenkins (1999), Modeling thermodynamic ice-ocean interactions at the base of an ice shelf, *J. Phys. Oceanogr.*, *29*(8), 1787–1800.

Holland, P. R., A. Jenkins, and D. M. Holland (2010), Ice and ocean processes in the Bellingshausen Sea, Antarctica, *J. Geophys. Res.*, *115*(C5).

Huhn, O., H. H. Hellmer, M. Rhein, C. Rodehacke, W. Roether, M. P. Schodlok, and M. Schröder (2008), Evidence of deep-and bottom-water formation in the western Weddell Sea, *Deep Sea Res. II*, *55*(8), 1098–1116.

Hunke, E. C., and J. K. Dukowicz (1997), An elastic-viscous-plastic model for sea ice dynamics, *J. Phys. Ocean.*, *27*, 1849–1868.

Hunke, E. C., and W. H. Lipscomb (2010), CICE: The Los Alamos Sea Ice Model, Documentation and Software User's Manual, version 4.1, la-cc-06-012, *Tech. rep.*, Los Alamos National Laboratory, Los Alamos, USA, 76 pages.

Jacobs, S., C. Giulivi, P. Dutrieux, E. Rignot, F. Nitsche, and J. Mouginot (2013), Getz Ice Shelf melting response to changes in ocean forcing, *J. Geophys. Res.*, *118*(9), 4152–4168.

Jacobs, S. S., and C. F. Giulivi (2010), Large multidecadal salinity trends near the Pacific-Antarctic continental margin, *J. Clim.*, *23*(17), 4508–4524.

Jacobs, S. S., H. H. Hellmer, and A. Jenkins (1996), Antarctic ice sheet melting in the Southeast Pacific, *Geophys. Res. Lett.*, *23*(9), 957–960.

Jacobs, S. S., C. F. Giulivi, and P. A. Mele (2002), Freshening of the Ross Sea during the late 20th century, *Science*, *297*(5580), 386–389.

Jacobs, S. S., A. Jenkins, C. F. Giulivi, and P. Dutrieux (2011), Stronger ocean circulation and increased melting under Pine Island Glacier ice shelf, *Nat. Geosci.*, *4*(8), 519–523.

Jenkins, A. (1991), A one-dimensional model of ice shelf-ocean interaction, *J. Geophys. Res.*, *96*(C11), 20,671–20,677.

Jenkins, A. (1999), The impact of melting ice on ocean waters, *J. Phys. Oceanogr.*, *29*(9), 2370–2381.

Jenkins, A., and S. Jacobs (2008), Circulation and melting beneath George VI ice shelf, Antarctica, *J. Geophys. Res*, *113*, C04,013.

Jenkins, A., P. Dutrieux, S. S. Jacobs, S. D. McPhail, J. R. Perrett, A. T. Webb, and D. White (2010), Observations beneath Pine Island Glacier in West Antarctica and implications for its retreat, *Nat. Geosci.*, *3*(7), 468–472.

Leppäranta, M. (1983), A growth model for black ice, snow ice, and snow thickness in subarctic basins, *Nordic Hydrology*, *14*, 59–70.

Maykut, G. A. (1977), Estimates of the regional heat and mass balance of the ice cover, in *A Symposium on Sea Ice Processes and Models*, vol. I, pp. 65–74, University of Washington, Seattle.

Nakayama, Y., M. Schröder, and H. H. Hellmer (2013), From circumpolar deep water to the glacial meltwater plume on the eastern Amundsen Shelf, *Deep Sea Res. I*, *77*, 50–62.

Nakayama, Y., R. Timmermann, M. Schröder, and H. H. Hellmer (2014), On the difficulty of modeling Circumpolar Deep Water intrusions onto the Amundsen Sea continental shelf, *Ocean Model.*, *84*, 26–34.

Nakayama, Y., R. Timmermann, C. B. Rodehacke, M. Schröder, and H. H. Hellmer (accepted), Modeling the spreading of glacial melt water from the Amundsen and Bellingshausen Seas, *Geophys. Res. Lett.*

Orsi, A. H., G. C. Johnson, and J. L. Bullister (1999), Circulation, mixing, and production of Antarctic Bottom Water, *Prog. Oceanogr.*, *43*, 55–109.

Owens, W. B., and P. Lemke (1997), Sensitivity studies with a sea ice-mixed layer-pycnocline model in the Weddell Sea, *J. Geophys. Res.*, *95*(C6), 9527–9538.

Pacanowski, R. C., and S. G. H. Philander (1981), Parameterization of vertical mixing in numerical models of the tropical oceans, *Journal of Physical Oceanography*, *11*, 1443–1451.

Parkinson, C. L., and W. M. Washington (1979), A large-scale numerical model of sea ice, *J. Geophys. Res.*, *84 (C1)*, 311–337.

Pritchard, H. D., S. R. M. Ligtenberg, H. A. Fricker, D. G. Vaughan, M. R. Van den Broeke, and L. Padman (2012), Antarctic ice-sheet loss driven by basal melting of ice shelves, *Nature*, *484*(7395), 502–505.

Rignot, E., S. S. Jacobs, J. Mouginot, and B. Scheuchl (2013), Ice-shelf melting around Antarctica, *Science Express*, *341*, 226–270.

Rignot, E., J. Mouginot, M. Morlighem, H. Seroussi, and B. Scheuchl (2014), Widespread, rapid grounding line retreat of Pine Island, Thwaites, Smith, and Kohler glaciers, West Antarctica, from 1992 to 2011, *Geophys. Res. Lett.*, *41*(10), 3502–3509.

Rignot, E. J. (1998), Fast recession of a West Antarctic glacier, *Science*, *281*(5376), 549–551.

Rintoul, S. R. (2007), Rapid freshening of Antarctic Bottom Water formed in the Indian and Pacific oceans, *Geophys. Res. Lett.*, *34*(6), L06,606.

Saha, S., S. Moorthi, H.-L. Pan, X. Wu, J. Wang, S. Nadiga, P. Tripp, R. Kistler, J. Woollen, D. Behringer, et al. (2010), The NCEP climate forecast system reanalysis, *Bull. Amer. Meteorol. Soc.*, *91*(8), 1015–1057.

Schlosser, P. (1986), Helium: a new tracer in Antarctic oceanography, *Nature*, *321*, 233–235.

Schmitz, W. J., Jr. (1995), On the interbasin-scale thermohaline circulation, *Rev. Geophys.*, *33*, 151–173.

Semtner Jr., A. J. (1976), A model for the thermodynamic growth of sea ice in numerical investigations of climate, *J. Phys. Ocean.*, *6*(3), 379–389.

Seroussi, H., M. Morlighem, E. Rignot, J. Mouginot, E. Larour, M. Schodlok, and A. Khazendar (2014), Sensitivity of the dynamics of Pine Island Glacier, West Antarctica, to climate forcing for the next 50 years, *The Cryosphere Discussions*, *8*(2), 1873–1894.

Sültenfuß, J., W. Roether, and M. Rhein (2009), The Bremen mass spectrometric facility for the measurement of helium isotopes, neon, and tritium in water, *Isotopes in Environmental and Health Studies*, *45*(2), 83–95.

Timmermann, R., and H. H. Hellmer (2013), Southern Ocean warming and increased ice shelf basal melting in the twenty-first and twenty-second centuries based on coupled ice-ocean finite-element modelling, *Ocean Dynamics*, *63*(9-10), 1011–1026.

Timmermann, R., S. Danilov, J. Schröter, C. Böning, D. Sidorenko, and K. Rollenhagen (2009), Ocean circulation and sea ice distribution in a finite element global sea ice–ocean model, *Ocean Model.*, *27*(3), 114–129.

Timmermann, R., Q. Wang, and H. Hellmer (2012), Ice-shelf basal melting in a global finite-element sea-ice/ice-shelf/ocean model, *Ann. Glaciol.*, *53*(60), 303–314.

Wang, Q., S. Danilov, D. Sidorenko, R. Timmermann, C. Wekerle, X. Wang, T. Jung, and J. Schröter (2014), The finite element sea ice-ocean model (fesom) v. 1.4: formulation of an ocean general circulation model, *Geosci. Model Dev*, *7*, 663–693.

Wunsch, C. (1978), The North Atlantic general circulation west of 50° W determined by inverse methods, *Reviews of Geophysics*, *16*(4), 583–620.

Zillman, J. W. (1972), A study of some aspects of the radiation and heat budgets of the southern hemisphere oceans, in *Meteorological study*, vol. 26, Bureau of Meteorology, Dept. of the Interior, Canberra, Australia, 526 pages.